Protein Crystal Presentation for Synchrotron Diffraction: Acoustic Techniques

Christian George Burton

Doctor of Philosophy

Aston University

September 2018

Aston University

Thesis Summary

Protein Crystal Presentation for Synchrotron Methods: Acoustic Techniques

Christian George Burton

Doctor of Philosophy

2018

This thesis describes the design, development and testing of novel acoustic mounting methods for the diffraction of protein crystals for structural biology.

Sample environment and presentation is a challenging field set within the larger subject of protein crystallography. The needs of researchers to achieve the highest resolution data collection from difficult to fabricate samples, sits alongside the need for complex experimental conditions, where temperature, hydration and chemistry must be altered and controlled. A movement within the structural biology field away from obtaining structures at cryogenic temperatures, towards high resolution structures at room temperature, where proteins may still function, has been the driver to search for novel solutions.

To approach this 'solution space' the following work draws on acoustic manipulation techniques, looking for self-assembly and non-contact manipulation. Thus for the first time acoustic standing wave crystal trapping and also acoustically induced rotation have been shown in situ to be viable for use with protein crystallography, a fundamental proof paving the way for new time resolved and high throughput methods. The methods investigated

included both surface acoustic and bulk acoustic waves, looking at self-assembly and flow induced rotation. Each demonstration addresses a fundamental need within the automation of room temperature crystallography, demonstrating both the technique and quantifying the diffraction resolution for the first time.

Through the completion of these novel experiments acoustic sample presentation has been proven viable. The demonstrated method does not require crystals be removed from crystallisation fluid before mounting (using the acoustic trapping method), thus enabling the application of secondary fluids and paving the way for a fully continuous and microfluidic technology. Moreover acoustic goniometry lends itself to the automated mounting and collection of small batch crystal data by removing the need for delicate spine mounting. Both methods constitute a significant extension in the ability of researchers to utilise non-contact methods to control and interact with their proteins and crystals at room temperature.

Keywords: Diffraction, Acoustics, Self-Assembly, Macromolecular Crystallography

Dedicated to Hanna and my family

Acknowledgements

The learning and research that took place during the writing of this thesis was only possible with the help and patient support of family, alongside scores of good friends and colleagues. It is fair to say that there are too many people to thank, people who at one time or another have provided support, insight and generous amounts of their time.

I would firstly like to thank my academic supervisors, Paul Topham and Mark Prince. Mark's passion for engineering is only out-weighed by his problem solving capability and perseverance during late night X-ray sessions. Paul's ability to develop leading research has been an inspiration, acting as the first port of call for many of the challenges we faced and always made time to meet in spite of a busy schedule.

It would be remiss not to highlight the exceptional and staunch support and opportunities that were Pete Docker's contribution as my Diamond Light Source supervisor, the original architect for the project. Aside from securing funding and experimental access, he ensured I had familiarity with state of the art facilities and techniques around the world, made a great travel companion and friend.

In addition to my principle supervisors, the support and enthusiasm generously offered by Danny Axford before, during and after beam times will stand as an example for the remainder of my career.

Thank you to Aston University and Diamond Light Source ltd for funding and supporting the research that forms this thesis.

Thanks to Mike Newton for his introduction to the world of acoustics and transducer design, to Rob Morris for the coaching on signals analysis and SAW fabrication, and Andy Edwards

for the long days in the photolithography lab. The generous welcome I received to their institution was deeply kind.

Thanks to Allen Orville and Pierre Aller for including me in XFEL 2017, it was a privilege to be involved in such an early stage of the facility, and along with our conversations throughout our project have helped to transform my understanding of structural biology.

Thank you to Kate Sugden who has quietly mentored my engineering training since the first days of my undergraduate degree at Aston. A special thank you to James Duggins who has provided constant support guidance and generous amounts of his time without which much of the work described would not have been possible. Thanks also to Reece Lillie, Mike Rowley, Graham Varley, Lillie Melody, Prashant Hirani, Dave Palmer and Stuart Hallard who have all helped turn ideas and concepts into real experiments.

Thank you to my fellow doctoral students of room 111, past and present, who have helped make the journey the pleasure it was. Thank you to my friend Matt Allen who has been a constant source of encouragement, patience, and adventure, often in equal measure. Thanks to David Hardy for helping me get to grips with molecular biology, David Eckold for his engineering insight, Anna Isakova and Georgie Parkes for instruction in polymer chemistry, and Bernie Lawless for discussions on experimental methods.

Finally thank you to my beautiful wife, parents, in-laws and extended family, who it is fair to say, put up with a lot.

Conference and journal items created as part of this project

M. Prince, P. Docker, C. Burton, R. Hussain, J. Kay, and G. Silgardi, "*The application of 3D printing to study microfluidic architecture for 'on-chip' mixing systems for SRCD and UV spectroscopy*" in Biotech, biomaterials and biomedical, 2015, pp. 198–201.

C. Burton, P. Docker, M. Prince, D. Axford, A. Orville, and P. Topham, "*Contact angle and active drop transport for time resolved Macromolecular and serial femto-second crystallography*" in Informatics, Electronics and Microsystems - TechConnect Briefs *2017*, 2017, vol. 4, pp. 116–119.

C. G. Burton, D. Axford, A. M. J. Edwards, R. J. Gildea, R. H. Morris, M. I. Newton, A. M. Orville, M. Prince, P. D. Topham, and P. T. Docker, "*An acoustic on-chip goniometer for room temperature macromolecular crystallography*," Lab Chip, vol. 17, no. 24, pp. 4225–4230, 2017.

A. Isakova, C. Burton, D. J. Nowakowski, and P. D. Topham, "*Diels-Alder cycloaddition and RAFT chain end functionality: An elegant route to fullerene end-capped polymers with control over molecular mass and architecture*" Polym. Chem., 2017.

Table of Contents

List of Abbreviations

BAW	Bulk Acoustic Wave
DLS	Diamond Light Source
FWHM	Full Width Half Maximum
HF	High Frequency
Hz	Hertz, cycles per second
IDT	Inter-Digitated Electrodes
LCP	Lipidic Cubic Phase
PEVCD	Plasma Enhanced Vapour Deposition
PDB	Protein Data Bank
PZT	Lead Zirconate Titanate
RF	Radio Frequency
SAW	Surface Acoustic Wave
SLA	Stereo Lithography
SSAW	Standing Surface Acoustic Wave
TEM	Transmission Electron Microscopy

List of Figures

Glossary

Acoustic	Physics concerned with the propagation of mechanical of waves.
Anti – Node	The point of maximum amplitude change in a wave.
Macromolecule	*IUPAC definition: 'A molecule of high relative molecular mass, the structure of which essentially comprises the multiple repetition of units derived, actually or conceptually from molecules of low relative molecular mass.'*[1]
Mesophase	A state of matter in between liquid and solid
Node	The point of minimum amplitude change in a wave.
Radiation Damage	The degeneration of a molecule and/or crystal during diffraction, typically presenting as an exponential decay in the number of diffraction spots visible in stills.

Spine	A small needle-like rod used in the mounting of protein crystals.
Self-assembly	A system in which elements have an affinity for a particular arrangement.
Transducer	The devices used to convert electrical signal energy into mechanical strain energy.
Ultrasonic	Sound frequencies beyond the audible range of human hearing (typically above 20 000 Hz).

1. Introduction

The work in this thesis investigates two acoustic manipulation methods for presenting protein crystals for X-ray diffraction, and structure determination. Structural biology is tasked with describing the molecular structure and function of macromolecules, structures which are responsible for the wide diversity of life, from viruses to flora and fauna. Recent advances have shown that structures are physically different dependent on the temperature at which they are imaged, and since structures determine affinity for molecules and availability of binding sites work in the field has moved to image significantly more crystals at room temperature. A challenge that arises from this move is an increase in radiation damage, effectively shortening the lifespan of crystals in beam due to the absence of protective cryogenic effects. A natural direction is an increase in the number of crystals imaged, typically using smaller and harder to handle crystals, a move which increases demand at state of the art microfocus beamlines. The following work investigates two methodologies which circumvent current mounting practices, instead using acoustic fields within the crystallisation fluid itself to mount samples, demonstrating the potential for lab on a chip techniques to create a paradigm shift in the handling of protein crystals.

The aims of the work were to specify design and test acoustic mounting methods, the specific aims were to:

- Describe the protein crystal handling environment.
- Specify the operating needs for acoustic manipulation.
- To demonstrate the acoustic effects within crystallisation fluid and protein crystals.
- To demonstrate diffraction whilst acoustic power is applied to the sample.
- To assess the suitability of crystal motion for protein crystal diffraction, considering the quantity of data achievable.

- Design, manufacture and test an acoustic protein-crystal mounting device.
- Design, manufacture and test an acoustic alternative for goniometry.

Of the current frontiers in science, perhaps the most interesting and possibly most important are found within biology. Biological building blocks, such as amino acids and proteins make up complex life, are key to aging, disease and even our ability to think. Proteins exist and function at a length scale we have yet to master despite our technological progress. Recent work has highlighted the need to expand our understanding beyond snapshots of proteins at extremely low temperatures to include images of them in multiple states and in multiple conditions. Thanks to advances in technology that include advances in X-ray detectors and diffraction techniques, data processing (both calculation power and the algorithms) the way has been paved for significantly higher throughput systems. Within this work self-organising techniques were investigated, testing their suitability for automating presentation of protein crystals in for X-ray diffraction for the first time.

1.1 Proteins and macromolecular crystallography

1.1.1 What is a protein

Introducing proteins as topic it is useful to look at the smaller sub-units make up a protein and then some of the functions that proteins perform. Proteins are polymers made up from molecular building blocks called amino acids.[2]

There are 20 types of common amino acids found in humans (selenocysteine being relatively rare [3]). Amino acids are made up of 6 elements, C, O, N, H, S, Se. The amino acids are formed of a standard group which when linked into a protein (a linear polymer, or a chain) form 'the

protein backbone'. Attached to the standard group is a further functional group that gives the amino acid its properties and in all but one case, chirality. [2], [4], [5]

It is apparent that the complexity seen in the living world requires more than a linear polymer chain. The chain naturally collapses or folds into a shorter three-dimensional arrangement called a secondary structure, self-organising to form *so-called* 'secondary' shapes such as an 'α-helix' (where the protein backbones form a spiral) or a 'β-sheet' (where the linked amino acids form a more planar ribbon-like molecule).[2]

Once the basic units have been assembled, further complexity exists as tertiary and quaternary structures. The tertiary structure being a grouping of the α-helices and β-sheet (more exotic structures have been omitted for brevity). Finally, the quaternary being a cooperative group of tertiary structures.[6]

To summarise and simplify the above: the folding of the amino acid chain gives a protein its complex structure. The three-dimensional structure prevents or encourages molecular interactions, often called the 'Lock and Key' model where the protein is a lock and the additional molecule is the key illustrated in Figure 1.1.

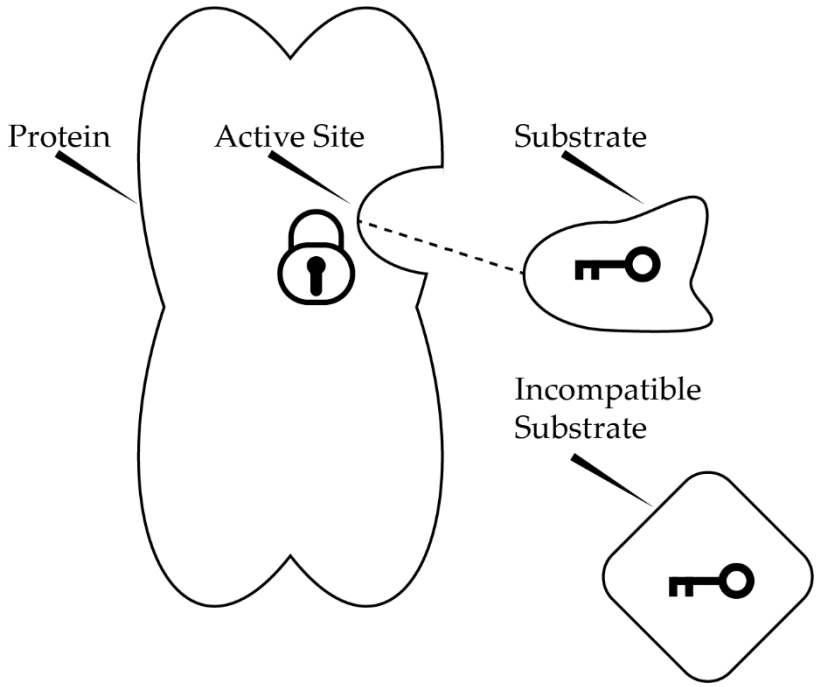

Figure 1.1 Lock and key model of protein substrate interaction.

Proteins are a three dimensional assembly of groups of atoms, so when another molecule or substrate 'bumps' into a protein it would do so at a length scale where the atomic configuration is relevant. The atomic length scale can be described as the angstrom (Å = 10^{-10} m), maps of proteins are also made at the angstrom scale. Since proteins are three dimensional, and interact with a high number of degrees of freedom (parts of the protein may translate or rotate), analytical techniques must be able to resolve the position of constituent atoms in space at the highest resolution possible to determine the action and affinity of the protein.

1.1.2 Protein Crystals

To diffract X-rays successfully, the molecule must be stacked in an ordered and periodic structure much like pool balls are arranged at the start of a game. This is the crystalline form of the protein, and the packing pattern the protein takes on is referred to as the unit cell. A significant amount of effort is required to encourage and optimise the protein crystallisation process, and often it is an even greater the challenge to create enough protein to form a crystal

in the first place.[7]–[9] Protein crystals are typically < 200 μm and may be < 1 μm.[10] Figure 1.2 shows two examples of proteins found in humans, with the unit cell representing the crystallised state.

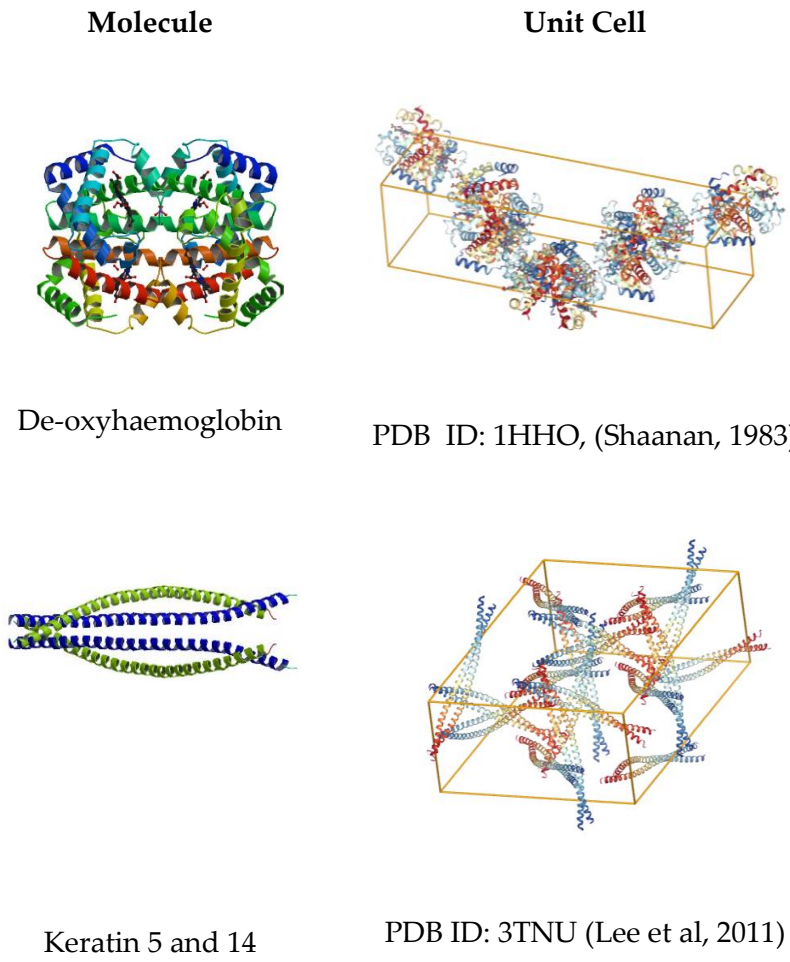

Figure 1.2 De-oxyhaemoglobin molecule structure and unit cell (top, and keratin complex and unit cell, (bottom)

1.1.3 Why use X-rays

Atoms and molecules are significantly smaller than the wavelength of visible light, if human vision is assumed to only be able to see light above 380 nm (4.2 Å) for scale, the visible (violet) light would fit one thousand glycine-amino acids into a single wavelength, with glycine being

0.42 nm in length.[11] A single protein molecule may be made up of 10 or more amino acids, and the position of each atom and group is important to the folding it undertakes, as such a light source that produces a wavelength much shorter than visible light is needed.[5] Light with a short enough wavelength to examine proteins with sufficient resolution occurs in the X-ray spectrum and is produced at specialist facilities called synchrotrons. Synchrotrons typically outperform lab based X-ray experiments through higher photon flux, better monochromation, all at shorter wavelengths (Figure 1.3 illustrates monochromation and brilliance). Photon wavelengths correspond with their energy by the relationship in equation (1.1).

$$E = \frac{hc}{\lambda} \tag{1.1}$$

Where E is energy in joules per photon, h is Planck's constant, c is the speed of light and λ is the wavelength. Comparing the energy in a photon at the centre of the visible light spectrum (500 nm wavelength), and a photon arriving at a beamline (1 Å wavelength), the beamline photon has around 5000 times more energy in every photon.

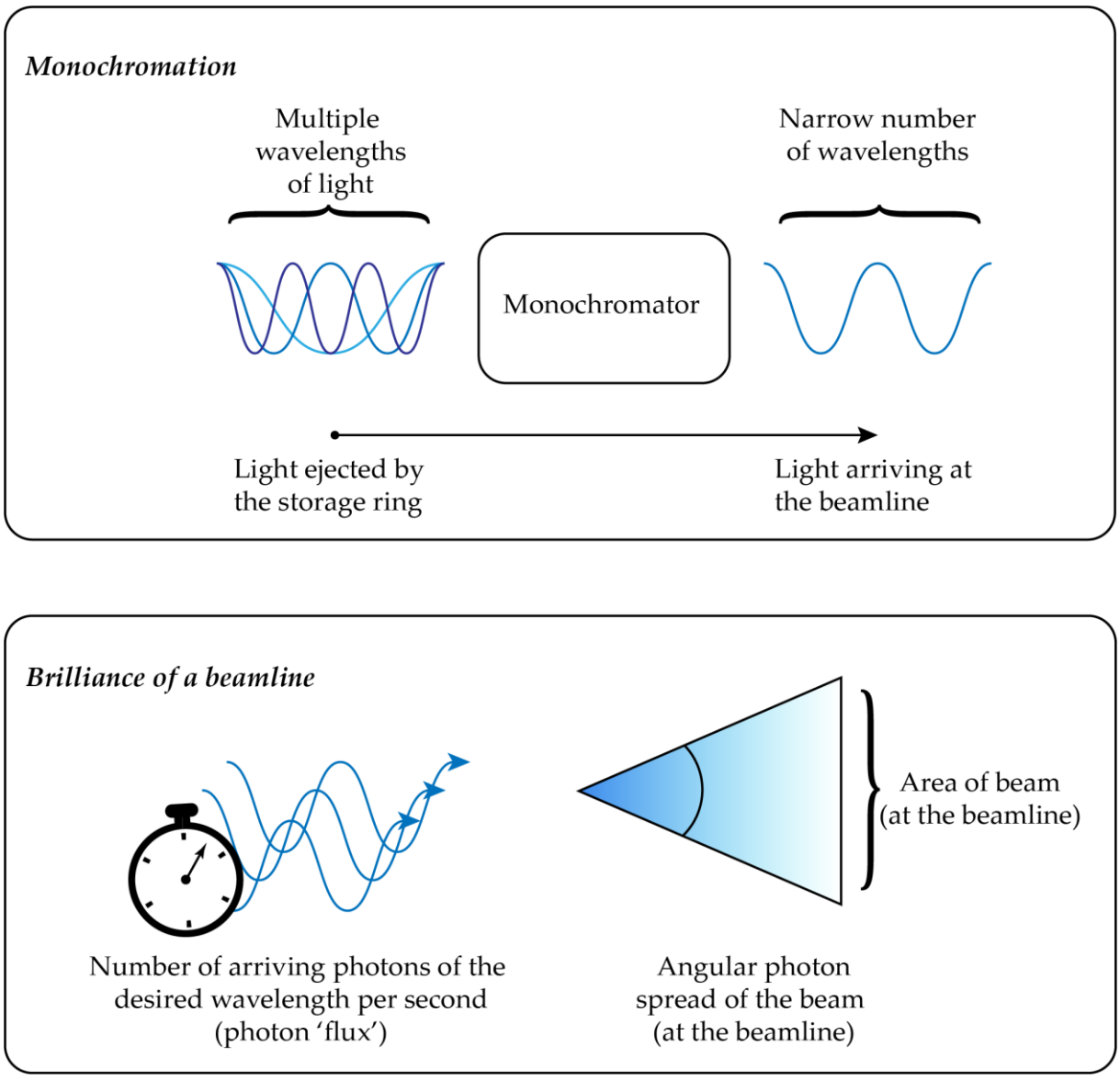

Figure 1.3 Schematic describing monochromation (top), and beamline-brilliance (bottom).

1.1.4 About Diamond

Diamond Light Source is a third generation synchrotron, operating with a storage ring energy of 3 GeV, pictured in Figure 1.4. The work contained within this thesis made use of beamline i24, which is a world leading micro-focus beamline dedicated to the study of structural biology. It is able to supply over a trillion photons per second focused into a 5 μm diameter beam when run at full intensity. This gives the beamline the title of 'high brilliance', which

coupled with state of the art Pilatus 3 X-ray photon detectors provides a leading experimental environment. Of current experiments undertaken at Diamond, approximately 50% are dedicated to life-science as can be seen from the breakdown of beamlines in Figure 1.5. [12]

Removed due to copyright restrictions

Figure 1.4 The Diamond Light Source Campus (© Diamond Light Source Ltd [13]*, 2018)*

Removed due to copyright restrictions

Figure 1.5 The Diamond Light Source Beamlines (© Diamond Light Source Ltd [14]*)*

1.1.5 Creation of a useable X-ray beam

The production of high frequency, high brightness, collimated X-ray light requires significant infrastructure:

"Synchrotron radiation occurs when a charge moving at relativistic speeds follows a curved trajectory"[15]

The creation of a consistent 'light-source' for science-users currently requires a particle accelerator, to raise the speed of electron bunches to a significant fraction of the speed of light. This phenomena can be seen in nature, in the *bremsstrahlung* (radiative braking of charged particles) around black holes and other astronomical bodies. [16] X-ray radiation is achieved by constructing a polygon more than a hundred metres in diameter, 24 sided in the case of DLS. The corners of the polygon have high strength magnets positioned at the corners, creating the radiative emittance on every circuit. The generation of a usable X-ray beam can be broken down into the following steps (Figure 1.6 is included for clarity):[17]

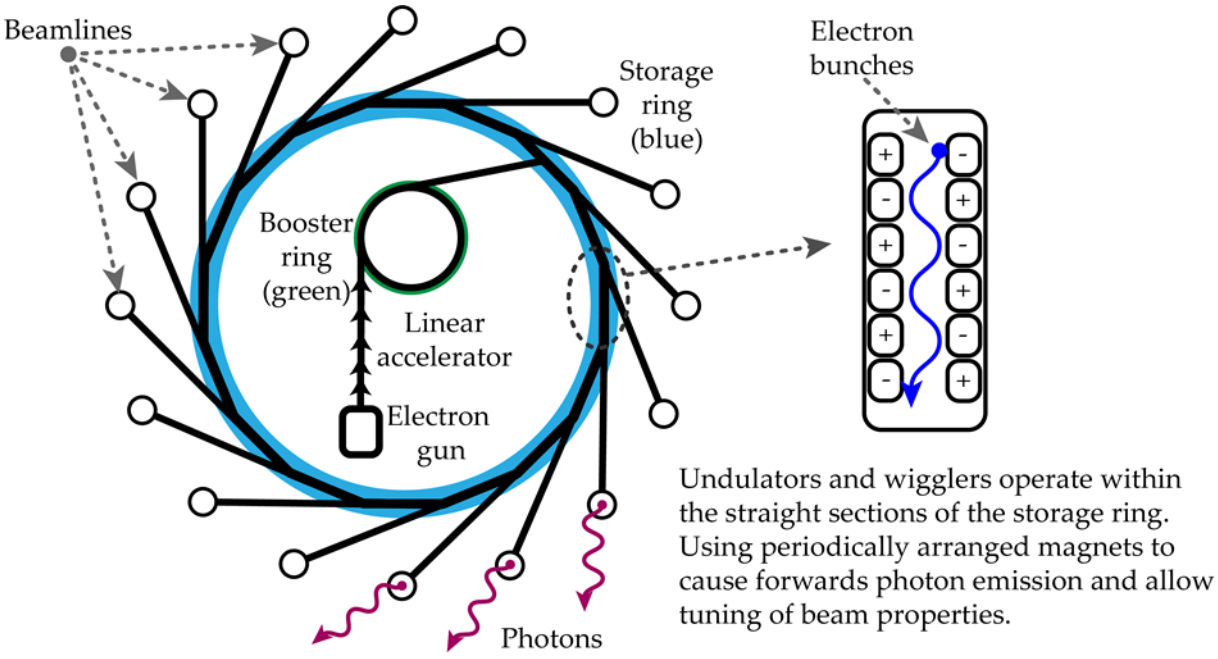

Figure 1.6 Schematic structure of a synchrotron.

- An electron gun produces small bunches of electrons which are passed into a linear accelerator.
- Electron bunches are passed from a 'linac' (linear accelerator) into a booster synchrotron, a smaller version of the final storage ring.
- In the booster ring, electrons are accelerated up from 0.1 GeV to match the energy of the storage ring (3 GeV at the time of writing).
- Once in the storage ring the electrons are maintained at a constant energy level, and as such a constant speed.
- As an electron bunch approaches a vertex of the polygon (typically having enough sides to approximate to a circle), a bending magnet redirects the electron bunch onto the next side of the polygon. It is at this point that radiative braking occurs, causing X-ray emission in the direction of original travel (i.e. at a tangent to the ring).
- In modern synchrotrons radiation output is enhanced through the use of undulators and wigglers, a linear and periodic arrangement of magnets that sits within each straight section. When this light is used, it leaves the straight section continuing in a straight line.
- The resulting light is then mono-chromated, filtered, and focused to achieve a usable beam.

Note, further power and beam features can be added through the use of undulators and wigglers, however are omitted for brevity, however both components serve to increase the radiation output of the synchrotron.

The relationship between the energy of the accelerated electron bunches, the radius of the turn the electrons take and the emitted power is shown in Equation (1.2) - (1.3).

$$\Delta E = P\frac{2\pi R}{v} \approx \frac{e^2\gamma^4}{3\varepsilon_0 R} \tag{1.2}$$

$$\gamma = \frac{1}{\sqrt{1-\frac{v^2}{c^2}}} = \frac{E}{m_0 c^2} \tag{1.3}$$

Where ΔE is the change in stored energy at the turn, P is the power of the storage ring (kW), v is the relative speed of the electron bunch, e is the charge of the electron bunch, γ is the relativistic constant, ε_0 is the magnetic permeability of a vacuum, m_0 is the resting mass of the electron bunch and R is the radius of the turn the electron bunches pass through.

It is possible to see that the power is proportional to the square of the stored energy (e) (equivalent to ring current). The radius of the turn provides a linear change to the intensity of the emitted light. The stored energy in the ring, 3 GeV for example, is shown to have affect the final radiative output at the fourth power, making it the dominant factor in a synchrotrons output.

1.1.6 X-ray diffraction

X-ray diffraction is the elastic scattering of light demonstrated by Laue in 1912. Laue formulated equations which describe the conditions required for diffraction to occur, defining a geometry often termed 'Laue cones' as set out in equations (1.4)-(1.6).[18]

$$a\cos(\mu_a) + a\cos(v_a) = n_1\lambda \tag{1.4}$$

$$b\cos(\mu_b) + b\cos(v_b) = n_2\lambda \tag{1.5}$$

$$c\cos(\mu_c) + c\cos(v_c) = n_3\lambda \tag{1.6}$$

Where a, b and c are spacings along the A, B and C unit cell vectors respectively, μ is the angle of incidence, v is the angle of in plane scattering, and n λ is the integer path difference.

The Laue conditions are important to this work as they underpin the need for goniometry, stating that the constructive interference occurs when the lattice periodicity when considered from the incident and scattered angle is equal to a multiple of the lights wavelength. By rotating a crystal lattice, different lattice elements are translated into positions which are n λ apart, and so the projected pattern is altered.

Ewald further described diffraction using the surface of a sphere to show that reciprocal lattice points which intersected a sphere of radius $1/\lambda$ caused constructive interference to occur and Bragg spots would be visible, as shown in Figure 1.7.[19] For a reciprocal lattice point to lie on the surface of the sphere, such as k' in Figure 1.7 it must satisfy the Laue equations, and so the Ewald sphere forms a geometric solution to Laue's equations. The position of the reciprocal lattice point follows Bragg's law, where: G has the length 1/d (d is the original lattice spacing); k is the incident beam and k' is the scattered beam; the Ewald sphere is shown as a circular dotted line and points satisfying the Ewald sphere (making them visible in a diffraction pattern) are shown in blue. Once the lattice is rotated new reflections constructively interfere and would be recorded on a second diffraction pattern.

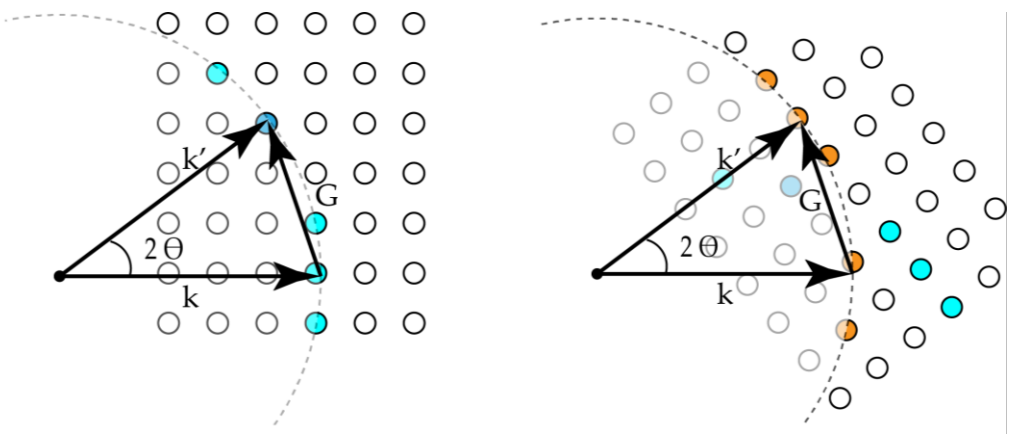

Figure 1.7 A schematic diagram of the Ewald sphere.

When considering an automated goniometer, experimental strategies attempt to ensure sufficient multi-axial rotation in order that a complete to record a complete set of reflections by sweeping the crystal lattice through the sphere. The elastic reflection of X-ray waves by atoms sums both constructively and destructively (via super position) to project a spot pattern. In single crystal diffraction, with an ideal crystal, there is a single pattern of spots presented for each rotational orientation of the crystal being struck by X-rays. [20]

If the crystal is ground up into many smaller crystals then all of these rotations are seen simultaneously (as the crystals, on average no longer possess orientation), and the diffraction appears as rings on the detector. For some proteins it is not possible to form a crystal, where it is possible, reconstruction of the protein from its crystal reflections allow for extremely high resolution models of the structures to be produced.[6] Both amorphous and crystalline diffraction are seen in protein crystallography, due to the presence of water and / or cryo-protectants, in and around most protein crystals.

The angle of reflection is determined by the inter-planar distance of a crystal, as described by Bragg's law, which is discussed in Section 2.3.

1.2 Current crystallography and synchrotron sample handling

With synchrotron time in high demand for structural biology and drug discovery the throughput of handling techniques becomes a limiting factor. The need for high throughput methods is driving research in macromolecular sample environments. The field is developing

at a rapid pace, with recent techniques already forming a part of standard beamline offerings on an international scale.

1.2.1 The Stanford Auto Mounting system

The Stanford Auto Mounting System (SAM), depicted in Figure 1.8, is a robotic-arm based beam-side sample retrieval method and the methodology is the workhorse of modern crystallography. The SAM system consists of: a beam-side dewer to hold pucks; pucks in turn hold assembled samples (which are composed of bases, spines, cryogenic loops shown in Figure 1.9); a handling robot; and a goniometer on which retrieved samples are mounted.[21] The system developed an international consensus on the size and shape of components reducing the complexity for researchers dispatching samples to synchrotrons. The variations on the standard are in use globally: MARVIN at DESY – P13; RoboDiff at ESRF – MASSIF-1; BART at Diamond. [22]–[25] The design philosophy behind the system is the reverse engineering of the human process for the hand mounting of crystals. The approach was developed by Stanford as the name suggests and has been in place for 13 years at the time of writing, the first paper published on the early development and prototyping of the system in 2002 [24].

The process begins with the screening of crystals, identifying those that are viable for diffraction characterisation. This involves inspection by eye, with birefringent imaging or Second Harmonic Generation microscopy and two-photon-UV-fluorescence (in SHG the light frequency is doubled in chiral regions, providing high contrast) to look for salt crystal, or to gain some sense of the protein content of the crystal.[26]–[28] This step is very much based on experience and 'know-how' despite technologies available to assist with this selection, typically due to cost or availability.[6], [29] A 'bad' crystal may still appear glassy and have

clearly defined edges, however the internal ordering may produce poor diffraction results. [30]

Once the crystals have been selected they are packaged and sent to the synchrotron for beam-side mounting, or they are mounted locally. An illustration of the SAM methodology pipeline is included in Figure 1.8.

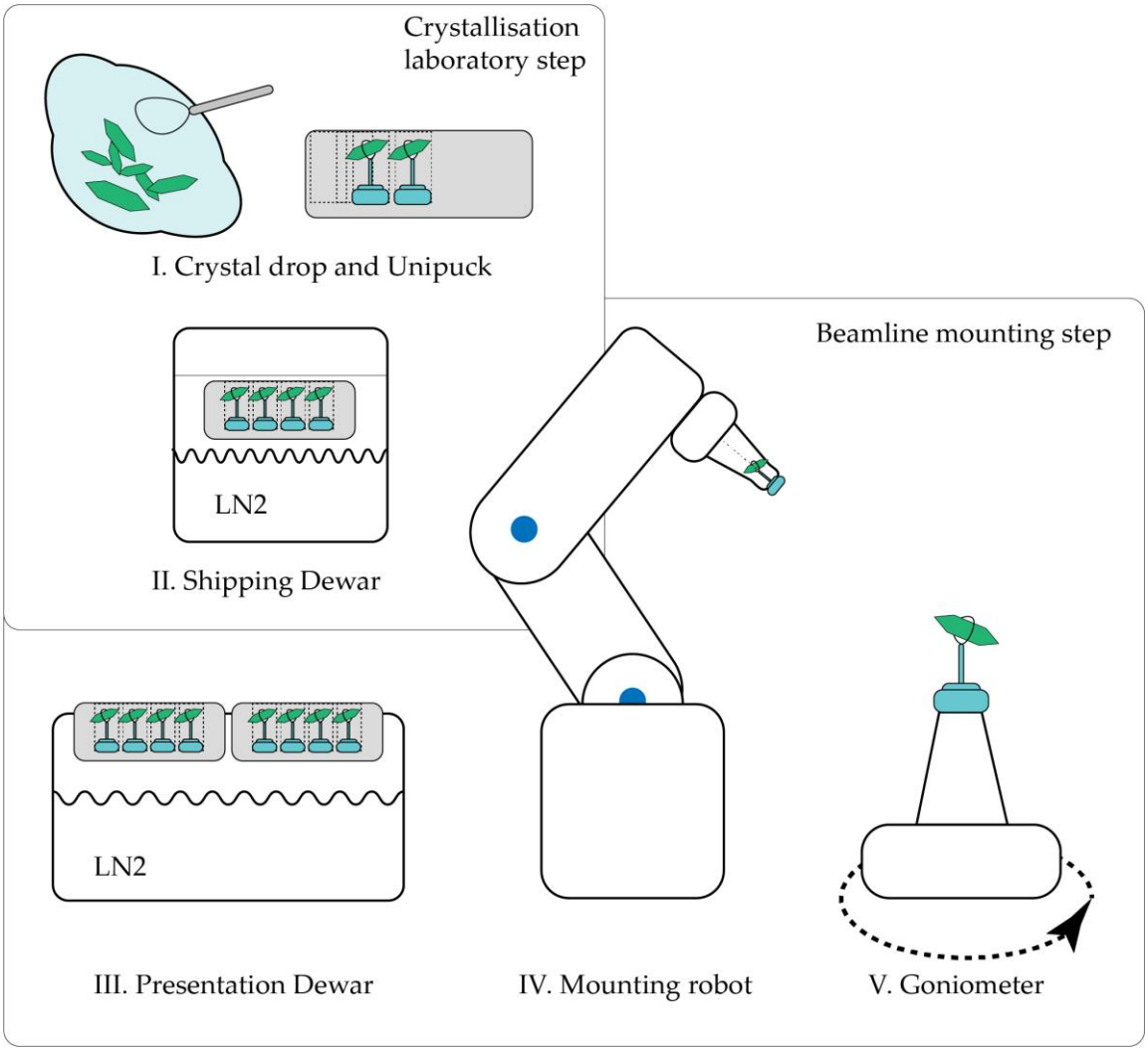

Figure 1.8 Schematic describing the SAMS methodology.

I. A selected crystal is hand mounted into a cryo-loop sized for the crystal to be examined (Figure 1.9 shows the loops which form the spine tips and is used to 'fish' for crystals).

II. The loop is mounted in to a spine (Also shown in the left of Figure 1.9), this is a standardised loading unit that is typically magnetic and can have a QR code on the underside for automated sample recognition.

III. The crystal mounted in to the spine is now loaded in to a puck, the pucks serve two purposes. The first is to safely hold the samples, the second is to provide a known position for the handling robot to retrieve the pucks from in the next step. The puck, when each of its bays have been filled, is placed in to a liquid nitrogen dewar adjacent to the beamline and in reach of the handling robot (Figure 1.10 shows pucks loaded into the presentation dewar at positions 36 ad 37). [31]

IV. In the next stage the beamline robot places a spine selected from a cryogenically-cooled puck onto the magnetic base on the goniometer.

At this point the mounting process has finished and the researcher takes back control from the machine and defines a 'collection strategy'; selecting a target site on the crystal for the beam to scan, the centre of rotation for the crystal and which angles the goniometer will pass through during scanning.

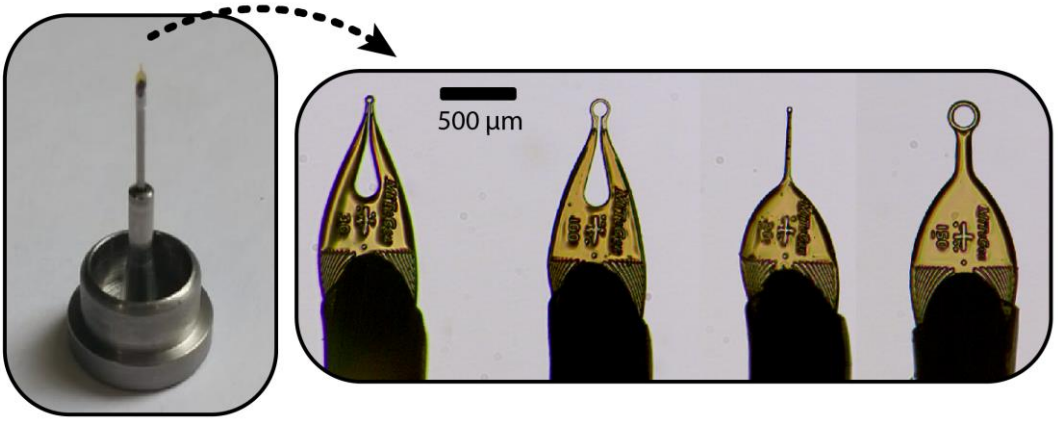

Figure 1.9 Mitegen, various crystal cryogenic-mounting loops.

Figure 1.10 Operational beam-side LN2 cryogenic-dewar containing Uni-puck spine holders in positions 36 and 37.

1.2.2 Establishing the opportunity for new sample mounting methods

There are a number of available sample mounting robots, used to provide a measure of automation typically for cryo-experiments. Commonly found systems include the Irelec CATS system, the Rigaku ACTOR and the Diamond Light Source developed BART system.

Figure 1.11 An example robotic systems available to researchers at DLS.

Simplifying the auto-mounting system routine to the robotic motion steps:

I. Retrieve a single sample from a puck held in the dewar.

II. Position the sample on a goniometer for inspection

III. Retrieve the sample and place it back in the dewar.

The BART system, operates on a similar cycle to each of the alternative robotic systems, however employs a cover over the dewar, along with an alignment calibration detail on the surface of the cover to reduce the complexity of the handling task for the robot.[32]

In one particular experiment, approximately 50 samples were scanned in 8 hour periods can be seen from the progress of the using the ACTOR (I02) and CATS (I04) system, and the data are shown in Figure 1.12. [33]

Figure 1.12 Data gathered by the BART project at Diamond (© Diamond Light Source Ltd [Ibid])

The BART system designers quote two achieved timescales for switch over, with 20.3 s during their first run, and 18.3 s during their current research run. This translates to an increase in the number of scans as is indicated by Figure 1.12.

The systems are sophisticated, composed of many parts, the significant dissimilarity between robot sample handling and fluid transport limits discussion to the total number of samples screened and the achieved change over times.

Table 1.1 Quoted change over times for operational robotic systems.

System	Location	Quoted Change Over Time
IRELEC CATS [33]	Diamond Light Source Ltd I04	Circa 90 seconds
Rigaku ACTOR [34]	Diamond Light Source Ltd I02	Circa 90 seconds
SPACE [35], [36]	Spring-8	40 Seconds
BART [Ibid]	Diamond Light Source Ltd I03	18-20 seconds
BESSY[37]	EBML BW7B	>60 seconds
TOMCAT [38]	Swiss Light Source	Not noted, however total data collection time > 5 mins suggesting circa 60 seconds

Spring-8 high throughput protein crystallography SPACE (SPring-8 Precise Automatic Cryo-sample Exchanger), demonstrates a significant gap between the found first and second place systems, when ranked by changeover speed.

To conclude a discussion of robotic methods it is important to highlight how well the systems currently serve the needs of the community, enabling 'mail-in' services and automated data

collection. Since the crystals are neatly mounted they are also able to act the end point of a robust mechanical linkage, and achieve a small sphere of confusion (the radius of a spherical volume through which the beam is swept). For smaller crystals that are more prone to radiation damage however there is a shorter collection time and so more crystals are required. If those numbers began to approach 1000 crystals, then the idle time caused by machine motion (taking 18 s as the nominal change over time) would be approximately 18 000 s or 5 hours. If the time it takes a researcher to mount a crystal on a spine is also taken in to account (assuming a crystal is mounted every 30 s, which is likely significantly faster than practical) then the researcher must continuously mount crystals for over 8 hours. As detector speeds increase and smaller protein crystals with shorter lifetimes are imaged, the interactions with each individual crystal will become a bottleneck at both in the lab and at beam-side.

1.2.3 Cryogenic and dehydrated sample handling

A current debate within the field of crystallography centres on whether or not to hold sample crystals at cryogenic temperatures or in dehydrated states during imaging. The debate is important as shows the need for multiple approaches to sample handling alongside unique benefits of lab-on-chip systems for macromolecular crystallography.

If a protein is thought of a bundle of hydrophilic and hydrophobic amino acids it follows that the molecule would be subject to differing forces and interactions (allostery) based on the presence of absence of water.[39], [40] Authors report that the presence and absence of water is sufficient to affect shape changes in molecules. [41] Given that protein molecules often remain in fluid throughout their working span it also follows that by holding protein in media or solution similar to the working conditions it would experience would produce the shape and structure it occupies 'normally'. [42]

A trade off occurs however, since dehydration improves crystal packing (mosaicity), which in turn improves diffraction.[43], [44] Improving mosaicity reduces the smear of Bragg spots, effectively sharpening the diffraction image.

An argument similar to that of dehydration exists for cryo-cooling crystals. Again the mosaicity is reduced, and a significant benefit arises in terms of radiation damage. In addition to the improved mosaicity, the crystal also experiences a longer lifespan in beam. Cryogenically cooled crystals experience radiation damage proportionally to the dose exposure. Whereas a room temperature crystal additionally experiences damage based on the length of time between the first and last dose.[41], [45] A crystal may have it's life extended by up to one hundred times the room temperature lifespan in a cryogenic state, at the cost of a change to the natural conformation. The reduction comes as a result of reduced mobility for radicals formed during irradiation as a result of Compton scattering.[46] Challenges arise in the hand-mounting techniques of cryo-cooled crystals as damage to crystals can occur and mosaicity can increase. [47]

1.3 Synchrotron sample environment research

A short review into current crystal mounting research is included here to give context to the variety of approaches that exists. An important result is a general lack of 'active' methods, as most rely on a secondary mechanism to bring crystals to an interaction region.

A range of materials have been investigated, typically focusing either on an extremely low thickness or a low X-ray attenuation coefficient, one particular study made use of cyclic olefin copolymer layers to create a micro diffusion experiment, an in a fashion similar to currently marketed crystallisation trays, enabled structure determination through in situ diffraction. Other studies also work with a similar concept, demonstrating the potential for a system that

integrates the crystallisation steps. [48]–[50] Graphene has been demonstrated as an excellent candidate for low background scatter screening, however supply of suitable material is limited at the time of writing. [51] In another work, authors grew crystals on vertically oriented slides, in 8 × 4 exposed droplets which were mounted inside the currently used puck and base arrangement. The droplets were held in position by hydrophobic coatings and oil (named the XCHIP). [52] This largely removed any housing material, however gave a longer path length through the drop than is otherwise achievable.

Axford and Aller *et al* specifically looked at the achievable background scatter within from current materials, helping to provide a standard for researchers to assess designs.[53] The work forms part of a body of work looking at thin film crystallisation, an attempt to move away from traditional crystallisation platforms towards single use, and X-ray compatible laminates.[54], [55]

Micro-electromechanical systems (MEMS) have been trialled for mounting crystals in an effort to automate the human aspect of the procedure, making use of computer vision and diffraction compatible 'micro-shovels' which were later mounted using the goniometer method.[56] A different approach trialled to increase the overall parallelisation was the inkjet deposition of hydrogels onto the protein crystal after mounting. The aim of the work was to bind the crystals in a chemical environment that reduced chemical stress which is a central concern as chemical and thermal stress can increase mosaicity and lead to the destruction of crystals.[57]

Lipidic cubic phase (LCP) is a technique that has moved from being a novel technique to a staple offering for hard to crystallise or synthesize proteins, requiring lower volumes of protein ($< 10\ \mu g\ ml^{-1}$) as the lipidic-meso-phase provides an ordering structure for the proteins. The resulting gel contains microcrystals that are suitable for serial crystallography due to the

short lifespan of small (< 5 μm) crystals under diffraction. [58], [59] Mounting takes place using 'toothpaste' type extruders and adapted spine mounts.[60]

Fixed targeting as a technique for MX, but in particular for serial crystallography is rapidly approaching maturity, and gaining use for routine use at XFEL facilities. For this technique, many crystals are mounted by depositing a drop of slurry onto an etched silicon chip. Excess fluid is wicked away and a backing is applied to prevent dehydration and to shorten path lengths.[61]–[63] A key advantage of this method is the small volume of crystals required when compared to liquid injection methods that are the norm at XFELs. A variant on fixed targeting is the hydrodynamic trap, where crystals are pulled into known locations by fluid forces. [64]

In situ crystallisation trays allow sitting drop vapour diffusion and have been shown to function in microgravity. [65] Trays are made of a low X-ray attenuating material and replace the 96 well plates crystallographers may have otherwise used. [66] A direct challenge to the use of diffraction compatible trays is the trade made between ruggedness of the tray and the amount of material X-rays must pass through. [53]

1.4 Acoustic manipulation methods

Acoustic manipulation forms the core work within this thesis, it is the direct or indirect application of force through an oscillating pressure field. In the case of this work the field is initially generated from a standing wave in both cases and two separate effects are leveraged to produce direct acoustic trapping and acoustic fluid coupling to produce rotational motion.

Acoustic manipulation is an active research area that is across many fields. A key question is: what is the effect of the acoustic field on the sample being processed? Within this work and also within the life sciences as a whole, the question of damage gains extra importance as often samples are fragile, small and are being evaluated on the nanometre or in the case of proteins Angstrom, length scale.

Reported methods for acoustic manipulation include acoustic beaming, ejection, a trapped array of particles in a horizontal tube (namely a Kundst tube), one, two and three dimensional standing wave fields, two and three-dimensional phased arrays which have variously been achieved with surface and bulk wave excitation.[67]–[69] Three-dimensional fields are challenging for X-ray crystallography because of phenomena including sphere of confusion, and the attenuation and background scattering caused by the crystallisation fluid. Acoustic beaming, one and two-dimensional fields however offer significant promise for rapid sample mounting. One and two dimensional fields may be switched on and off within a fraction of a second, and since they exist within a narrow volume, they may be constructed without creating a large volume for an X-ray to travel through, thus enabling high quality data capture.

Within the field of cell separation and analysis, trapping has been achieved directly and through the use of microspheres with higher acoustic contrast and an affinity for the cells. Cells were shown to be viable afterwards through culture and biomarkers, demonstrating that the technique may interact with soft matter at an appropriate length scale. [70]–[72] Selectivity based on the acoustic contrast (discussed in Section 2.6), and the use of fluorescence labelling has been shown to give greater specificity in final sorted populations, which may be leveraged in a pure salt crystal would likely have a different acoustic contrast to a protein crystal, as salts are likely to have a density approximately double that of protein.[73], [74] More complex

organisms (C-elgans) have been demonstrated as viable after exposure to manipulation in acoustic fields for periods exceeding one minute, providing further biological evidence of minimal or absent damage.[75], [76] When considering current techniques with respect to throughput, authors report half wavelength, single wavelength and multi-wavelength trapping, generating sorting based throughputs in the low KHz range (two to three orders of magnitude faster than required by current generation X-ray detectors).[77]–[80]

Narrowing the acoustic manipulation to work in which protein crystals are manipulated finds significantly fewer works actively manipulating crystals during diffraction, demonstrating an opportunity for further innovation. In the excellent work by Huang *et al* protein crystal were manipulated in a fashion similar to that of the Kundst tube, the work further extended its scope to demonstrate crystals responded to a two-dimensional field. All work was conducted horizontally and in direct contact with a SAW transducer which poses a challenge for X-ray diffraction due to shadowing, and attenuation. [81] However the work did demonstrate that there was no appreciable effect to the structure of actuated crystals, by removing them from the system and diffracting them using traditional goniometry.

Oberti et al also made use of acoustics to pattern of protein crystals, arraying them into a line, and passing them under an extraction hole, where the crystals were once again taken for mounting in loops and diffracted using the goniometer method.[82]

Driven by the dual needs of free electron laser facilities, and rapid fluid handling, work is ongoing, incorporating the ability for acoustic waves to eject small volumes of liquid droplets from larger drops into current methods (acoustic droplet ejection, ADE). Excellent benefits are available through acoustic ejection, the ability to deposit drops around three orders of magnitude smaller than for pipette methods; the ability to pattern crystals onto a substrate;

the ability to deposit chemicals into an existing drop quickly and with low fluid volume. The technology is used both on and off beam, within the XCHEM project using the commercially developed ECHO system, and an acoustically mounted tape drive working both with the Polypico system and in-house developments.[83]–[86] Authors also used ADE to mount samples onto micro-meshes for routine fixed target methods, providing convincing evidence that an acoustic goniometer may be integrated into a larger process for throughput..[87], [88]

In summary, current methods have mainly focused on cells, with few works considering the automation of protein crystal handling. Demonstrated methods appear to be sufficiently gentle to avoid crystal structure damage, and this has also been shown in an offline experiment. Further, the technology to allow simplified loading of crystal slurry drops into an on-chip goniometer or into an acoustic trap are obtainable commercially and would readily form part of a crystal presentation pipeline. The work contains within this thesis moves to depart from literature and to add to the current state-of-the-art methods by: trapping an array of crystals in a vertically oriented acoustic field; diffracting a crystal within an acoustic field; demonstrating effective X-ray-compatible acoustic-enclosures; using an acoustically vortexed fluid to rotate a crystal and generate a sufficiently complete dataset to process into a structure. Each technique adding to literature by demonstrating novel methods which may be readily purposed for high throughput methodologies.

1.5 Design inputs and the case for acoustic self-assembly

Summarising the challenges arising from current methods into design inputs gives the following:

- Synchrotron time is limited and in demand (time pressure).
- Methods are required for handling protein crystals in crystallisation fluids.
- Methods are required for handling protein crystals at room temperature.
- Protein crystal mounting is a time consuming step throughout the research pipeline.
- Any technique must be capable of producing high resolution data.
- Protein crystals under consideration will typically be under 200 μm.

Acoustic ordering and microfluidics match these requirements excellently. Acoustic fields are capable of influencing crystals without direct contact, removing the need for mounting. Standing wave acoustic fields have also been demonstrated to facilitate trapping and actuation.

This thesis describes the prototyping and performance of two acoustic techniques for the collection of protein crystal diffraction datasets. The first technique demonstrate trapping of small protein crystals within a vertically oriented standing wave field allowing them to be targeted for diffraction. The second technique makes use of acoustic wave interaction with fluid to cause a vortex in a droplet, which was used to capture a rotational-diffraction-dataset. Both techniques are presented for the first time.

1.6 Thesis Outline – Chapter by chapter

The thesis is comprised of six chapters:

Chapter One, the reader is introduced to the interdisciplinary topics of protein crystal diffraction, sample presentation and acoustic methods. Current challenges are outlined and the need for lab-on-a-chip techniques is described.

Chapter Three, describes the parameters and operating environment for protein crystal manipulation in fluid. Also included are engineering considerations which were the incorporated into the works of Chapter Four, Five and Six.

Chapter Four, details the specification, design, fabrication and testing of an acoustic standing wave mounting system for protein crystals. The system is evaluated on beam, and a measurements of diffraction compatibility and crystal motion are discussed.

Chapter Five, covers the specification, design, fabrication and testing of an on-chip acoustic goniometer. The system is evaluated on beam, crystal motion is described and a structure is successfully determined from the recorded data.

Chapter Six, discusses conclusions drawn from the work and envisioned future steps, devised from experience gained during the project.

1.7 Acoustics and acoustic methods

To develop a successful system for the presentation of protein crystals for synchrotron diffraction, context is important. The following chapter sets out to describe the key acoustic and fluidic theory, reviewing it with respect to current practices in X-ray crystallography. The following section goes on to introduce the methods and theory for effective acoustic trapping of protein crystals.

1.7.1 Acoustics

Acoustics is the branch of physics that describes the propagation of mechanical waves through solids, liquids, gases and plasma. The term ultrasonic is used to refer to those mechanical waves which exist outside the range of human hearing, and all frequencies used as part of this work can be considered ultrasonic. The first part of this chapter is formed of an overview of the acoustics and piezo electrics that were relied upon in experiment. The second half of the chapter is composed of physical concepts and material properties that describe the requirements for the standing wave trap.

1.7.1.1 Acoustic wave types

Two distinct types of waves were used to manipulate protein crystals within this work: Bulk waves, and surface waves. Each of the two wave types were used based on the need to create specific phenomena in fluid. Bulk waves are familiar within everyday experience in the form of speech and sound from speakers. Surface waves can come in the form of ripples on a pond or waves on the ocean, and exist at the boundaries between acoustic regions (e.g. liquid and gas, or solid and vacuum). Bulk waves radiate from an ideal point source in all directions, as

permitted by boundaries as shown in Figure 1.13. The key difference being that the bulk wave is spherical, pro and surface waves are relatively confined to a surface (elastic-half-space).

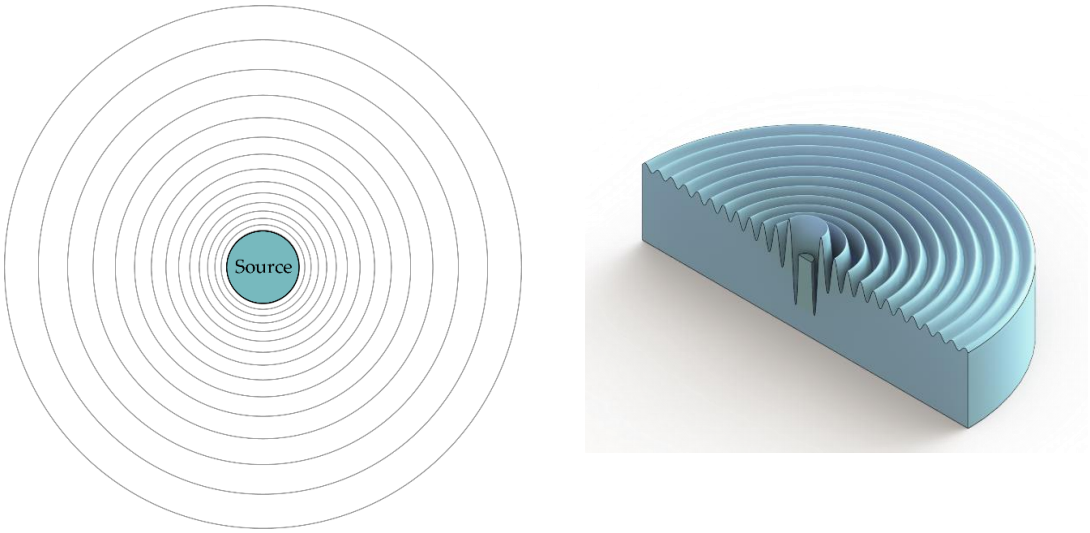

Figure 1.13 Graphical representation of an ideal acoustic-point-source (left), and a surface wave point source (right).

The propagation of waves through a continuous medium follows the general equation (1.7), where ∇^2 is the three-dimensional Laplacian, p is pressure, c is the thermodynamic speed of sound and t is time.[89]

$$\nabla^2 p = \frac{1}{c^2}\frac{\partial^2 p}{\partial t^2} \tag{1.7}$$

Surface waves as the name suggests are confined to the boundary between regions. When viewed from the normal to the surface they radiate in a similar way to a cross section of the ideal bulk wave, however for lithium niobate, an anisotropic material typically used for surface acoustic wave sensing and manipulation the penetration of the wave into the solid is minimal.[90] In lithium niobate (YZ, 128°), and indeed other materials the attenuation of a true surface wave requires only a few wavelengths in the through thickness direction. In contrast

along the direction of propagation losses are around 0.01 dB μs^{-1}.[91] Surface waves however have a relatively small amplitude with the height of a surface wave is typically of the order of 10 Å. [92]

Huygens-Fresnel principle states that for a propagating wave front, each point along the wave front should be considered the source of circular or spherical wavelets. [93] It is therefore possible to excite a plane wave (equivalent to a wave some distance from a point source as in Figure 1.13, by using a linear conductive strip, as found in the design of an interdigitated transducer. The Huygens-Fresnel principle is represented in Figure 1.14 (left), with an equivalent surface wave also shown (right).

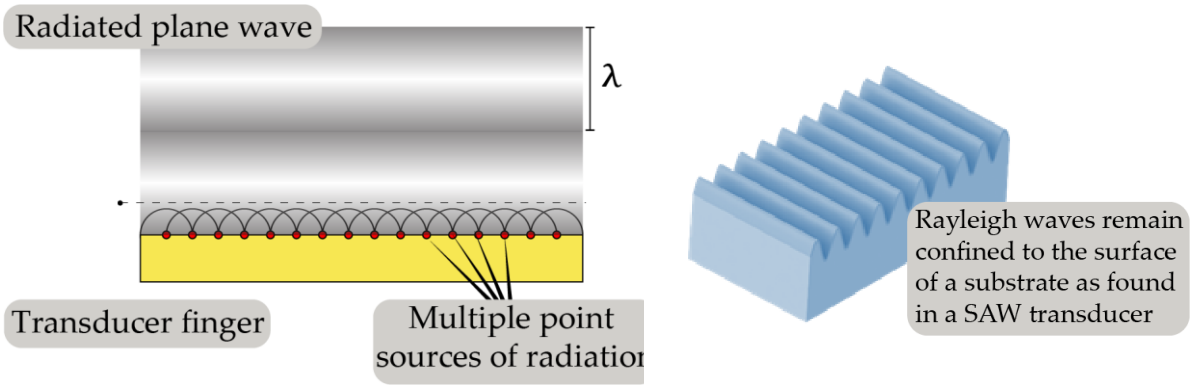

Figure 1.14 Graphical representation of Huygens principle (left) and the resulting surface-plane-wave (right)

1.7.1.2 Bulk wave transducers for acoustic ordering

To generate bulk wave excitation, as used to excite the standing wave phenomena in Section 3, a commercial through-thickness piezoelectric transducer was selected. Bulk wave transducers, typically used to generate bulk motion are ceramics, commonly made of lead zirconate titanate (PZT) or barium titanate. [94], [95] Once the ceramic is formed, a disordered

piezo electric effect exists, an electric field of the order of kV mm^{-1} is applied to create a device with a strong directional piezoelectric effect. [91] A typical acoustic coupling factor (the conversion from electric energy to mechanical strain) for commercially available piezo elements is > 0.4.[96]

One of the earliest demonstrations of wave and solid microparticle interaction was achieved by August Kundt in 1866, where a standing wave in air was excited within a tube and was used to order particles, Figure 1.15 shows the experimental setup in schematic form.[97]

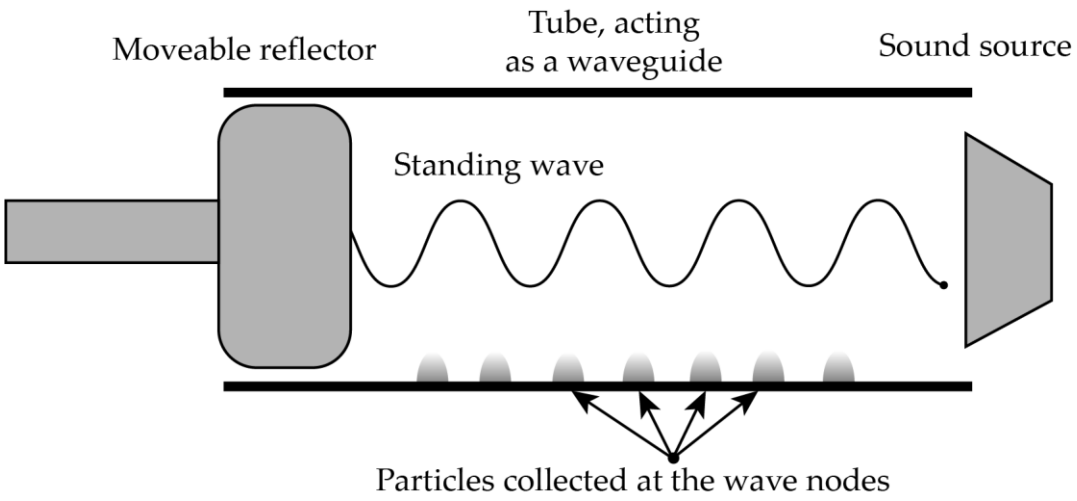

Figure 1.15 Kundt's tube schematic.

Work by Huang *et al* developed the concept for use with protein crystals, applying the technique to create one-dimensional crystal arrays in capillary tubes.[81] Since capillary tubes are currently manufactured in a way that is suitable for diffraction experimentation, the idea of creating a particle ordering effect inside the tube, lends itself to microfluidic integration. [20] The work did not extend to diffraction of crystals whilst undergoing acoustic ordering, but did succeed in showing crystals successfully survived the process.

The benefits of bulk acoustic regimes, include low cost of manufacture and the potential for higher power output than with surface waves. Sensibly, the central requirement should be the

sound reflectivity between the acoustic chamber and the medium. To achieve this, the speed of sound should be as different as can be realistically achieved between the medium and the chamber. This optimises the acoustic reflection inside the resonance chamber, allowing the excitation to create the streaming effect with minimum input power. BAW fields create an ordering force of around 10 nN [20]. Given the fragile and temperature sensitive nature of protein crystals, the need for, and benefit of, the larger distance separation distance achievable through bulk waves was apparent. The separation distance would provide opportunity for cooling remove bulk components from the region of interest.

At the time of writing, no papers were found that measured the effect of radio frequency (RF) vibration on the measurement of the crystal lattice structure of protein crystals undergoing X-ray diffraction. This is a challenging but rich topic for investigation, the challenge primarily stemming from the significant difference present in each of the crystals morphology and crystallinity, and an inability to repeatedly scan a sample twice. This is due to the severity of the X-ray light that the crystal is exposed to.

While the absence of this data raises questions, a paper was produced by Ding et al [21], that discussed the trapping of a live organism, namely Caenorhabditis elgans (also referred to as C elgans). In the paper the authors describe, not only being able to confine a living C elgans but being able to stretch it using their focused acoustic beam micro trapping technique. The ability of a living organism was capable of withstanding the forces involved in acoustic trapping, suggests protein crystals are likely to survive at a macro level.

1.7.1.3 Surface waves

Within the category of devices that deal with surface waves, there exist subdivisions based on the type of surface-wave. Acoustic plate mode, Lamb wave, Love wave, Rayleigh wave,

leaky SAW wave, Pseudo SAW (PSAW), High velocity pseudo SAW (HVPSAW). [98]–[100] Within this work the Rayleigh or SAW waves were used, which are a true surface wave, made possible by the orientation of the crystal substrate.[91] Surface waves are confined to the boundary between acoustic regions and lose little energy to bulk excitation.

1.7.1.4 Surface acoustic wave transducers

Surface acoustic wave transducers differ in construction to bulk type piezo elements, where the positive and negative electrodes are on opposing faces, ignoring the wrap-around-electrode which is purely for connection convenience. For a surface wave transducer the electrodes are adjacent and on the same surface as shown in Figure 1.16. This arises because, for a surface wave the high and low amplitude points on the wave must both be excited on the same surface and do not travel through the elastic half space. To achieve the excitation a set of interlocking electrodes that occupy the standing wave antinode positions are patterned onto the desired substrate.

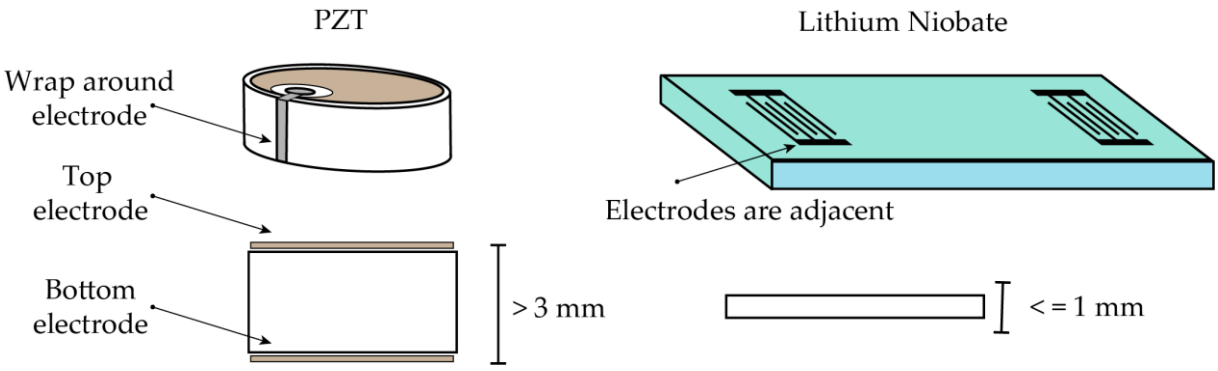

Figure 1.16 Electrode position schematic for PZT and Lithium niobate

Complex patterns have been investigated by authors of work considering SAW transducers for signal, sensing and particle manipulation applications, including single sided electrodes, apodised, tapered, split and orthogonal transducers as shown in Figure 1.17, with further variations typically used for generating complex waveforms which fall outside the scope of

this discussion. [76], [101]–[103] Split, apodised and single sided electrode configurations find use used within the field of signals and sensing, with designs affecting changes to the resonance peak and amplitude envelope.[91] Orthogonal transducers have been used by authors to excite a two-dimensional field and create grid type arrays of particles. [104] Single-Single electrodes (type A) were used throughout this work, since the wider electrodes gave greater manufacturing tolerances thanks to electrode thickness and the spacing between them. The need for X-ray compatibility prevented the use of designs that would require the lithium niobate to be present in the beam path (as it would fully attenuate the beam). Of the remaining designs, tapered electrodes (Figure 1.17 - F) would have allowed a wide range of input frequencies, and (Figure 1.17 – C) would have allowed the application of orthogonal waves, perhaps offering control over rotation.

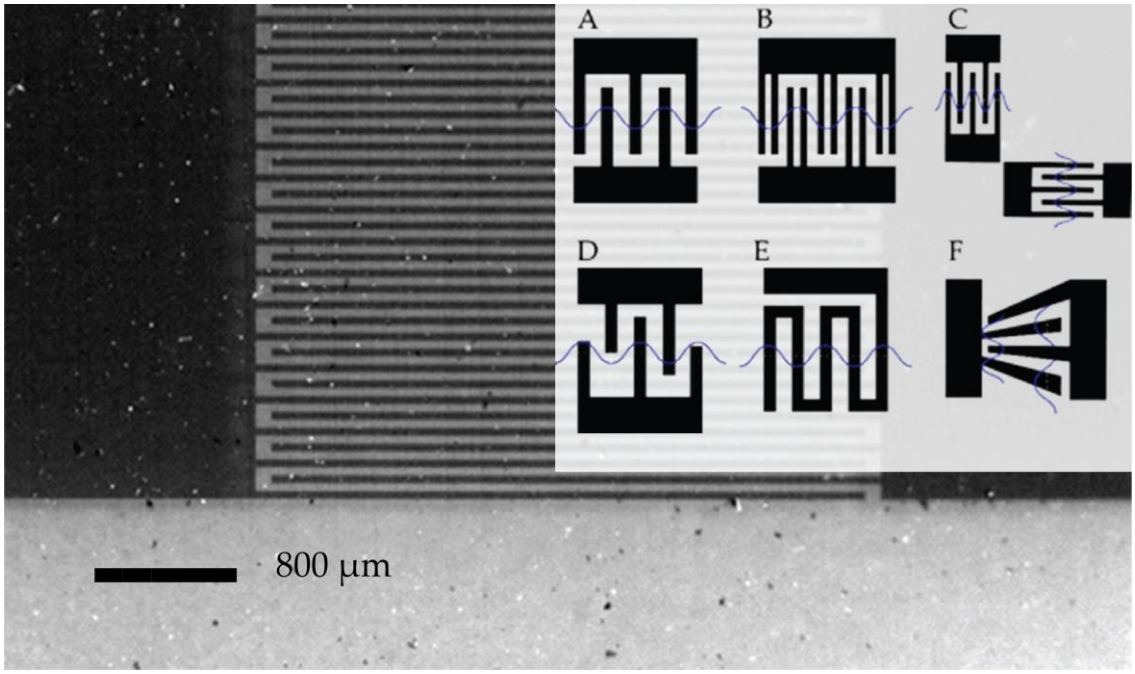

Figure 1.17 Image of a single-single transducer (Left) and Schematic of types of interdigitated transducers (Overlay): A) Single-Single B) Split electrode C) Orthogonal pairing D) Apodised electrodes E) Single Sided F) Tapered/chirp electrode.

Surface acoustic wave transducers make use of crystalline materials rather than the baked ceramics used within bulk-transducers. The crystalline form of a material is selected and a particular plane is selected from the crystal as sound propagation in crystalline materials is orthotropic. [105] Materials typically used for surface acoustic wave manipulation are laid out in Table 1.2. [106], [107] For the purpose of this work, the strength of acoustic coupling and the surface wave velocity were the key parameters.

Surface wave velocity is the speed of wave (sometimes referred to as phase) propagation across the surface. The cut refers to the angle a crystal is cut at relative to the unit cell and is typically quoted by manufacturers. Finally the coupling constant is the ratio at which electrical energy is converted into mechanical energy.

For the work described in Section 5 lithium niobate 128 ° YX was selected, as the higher coupling constant allows a reduced power input and therefore also reduction in heat generated.

Table 1.2 Material properties for candidate surface wave substrates

Material	Cut	Surface wave Velocity	Coupling Constant
Quartz	YX	3159	-
	ST	3158	0.045
Lithium Tantalate	YZ	3230	0.05
	112 YX	3288	0.0075
Lithium Niobate	YZ	3488	0.045
	128 YX	3992	0.053
Langasite		2600	-

1.7.1.5 Acoustic reflection and transmission

When acoustic waves meet boundaries, particularly in the case of enclosed fluid volumes as in Section 3A bulk-acoustic standing wave protein crystal mount, a portion of the wave is reflected, and a portion is transmitted into the second medium as shown in Figure 1.18.

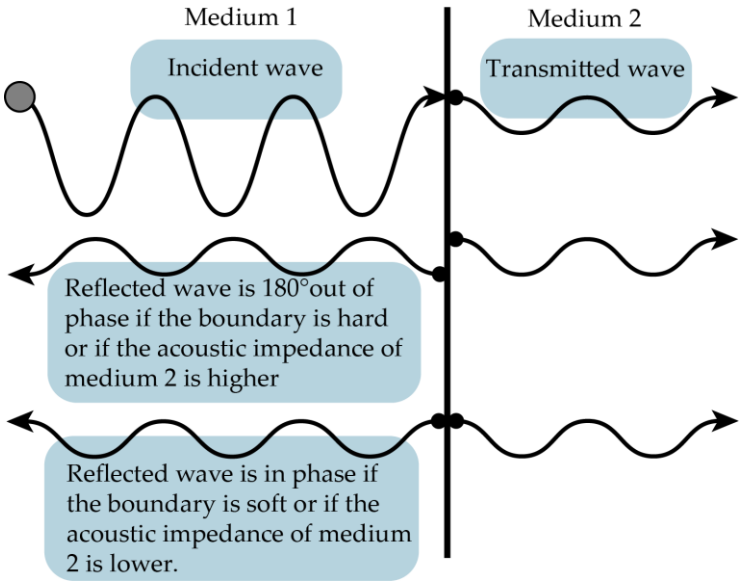

Figure 1.18 Transmission and reflection of a sound wave at a surface.

Typically the greater the mismatch between acoustic impedances the greater the reflection. A notable exception however is the half wave phenomenon. Using the Fresnel equations for the reflection of a non-polarised wave as shown in Equations (1.8) – (1.11), it is possible to calculate the ratio of reflection to transmission: [108]

$$V = \frac{\sqrt{\rho_1 E_1} - \sqrt{\rho_2 E_2}}{\sqrt{\rho_1 E_1} + \sqrt{\rho_2 E_2}} = \frac{n - m}{n + m} \tag{1.8}$$

$$n = \frac{c_1}{c_2} \tag{1.9}$$

$$m = \frac{\rho_1}{\rho_2} \tag{1.10}$$

$$c = \frac{E}{\rho} \tag{1.11}$$

Where V is the reflectance, ρ is density of medium 1 and 2 respectively, E is Young's modulus, n is the index of refraction and m is the density ratio.

The equations are also frequently rearranged in terms of admittances of the media as reproduced in Equations (1.12) - (1.14): [109]

$$Y_1 = A_1(\rho_1 c_1)^{-1} \tag{1.12}$$

$$Y_2 = A_2(\rho_2 c_2)^{-1} \tag{1.13}$$

The reflected wave g whose solution is:

$$\frac{g(t)}{f(t)} = \frac{Y_1 - Y_2}{Y_1 + Y_2} \tag{1.14}$$

Where Y is the admittance, A is the area, is the density, c is the speed of sound, g is the reflected wave and f is the incident wave.

Equations (1.8) and (1.14) are used for estimating one-dimensional interactions between material regimes. The topic of reflection and power transmission is developed further in Section 2.6.2.

1.7.2 Piezo Materials

Two piezo electric materials were used during the project. Bulk transducers often called 'soft' or 'baked' ceramics are formed from a compacted powder which is later baked and subjected to a high strength magnetic field to align the poles of the unit cells. Crystalline piezo electric materials including quartz, lithium niobate, lithium tantalate, are grown in large boules, typically based around a seed crystal of a known orientation, later to be diced and polished into useable wafers. To give the reader context for the following chapters some information and comparison is offered for the materials used. Given that piezo materials often find use at the forefront of precision movement and sensing applications, there is unsurprisingly a significant amount of theory to describe behaviours and phenomena, relevant theory is also presented.

1.7.2.1 Piezoelectricity

Piezein is the Greek word for to press, coined by Hankel in 1881 the term piezoelectric describes materials where strain within the material induces a charge, also the reverse is true and a

charge may induce a strain.[110] Piezo materials were used as part of this project to excite the acoustic waves used to actuate and trap crystals.

1.7.2.2 Complex impedance in piezo elements

Reactance arises from opposition to oscillation in a circuit and is present in both electronic and mechanical components. Reactance is described in terms of complex impedance (ς) obeying Equations (1.15) - (1.17).[111]

$$X_c = \frac{1}{2\pi f c} \tag{1.15}$$

$$X_l = 2\pi f l \tag{1.16}$$

$$Z_s = \sqrt{R^2 + (X_l - X_c)^2} \tag{1.17}$$

Where X_c is the capacitive reactance, X_l is the inductive reactance, f is the frequency, c is the capacitance, l is the inductance, R is the resistance, and Z_s is the complex impedance in a series circuit. As Z_s approaches the purely resistive value, the circuit is said to be in resonance. Figure 1.19 shows and equivalent circuit for a transducer, for the purpose of clarity the mechanical components of resonance have been separated from the electrical. The equivalent circuit describes the frequency that optimal transfer takes place. If a load is purely resistive then power transfer (at a given frequency) is resonant, or optimal. If a load shows capacitance or inductance some measure of power factor correction is required and a matching circuit should be constructed to reduce amplifier load and prevent amplifier damage through voltage-standing-wave-ratio (VSWR). VSWR is the amount of power which remains in physical connection between the amplifier and the piezo electric. For the work described in Section 3 and 5 matching circuits were not required as impedance matching (power factor correction)

had been conducted by the manufacturer in Section 3, and in Section 5 the power being applied low and the resonance quality was sufficiently high to avoid the additional complexity.

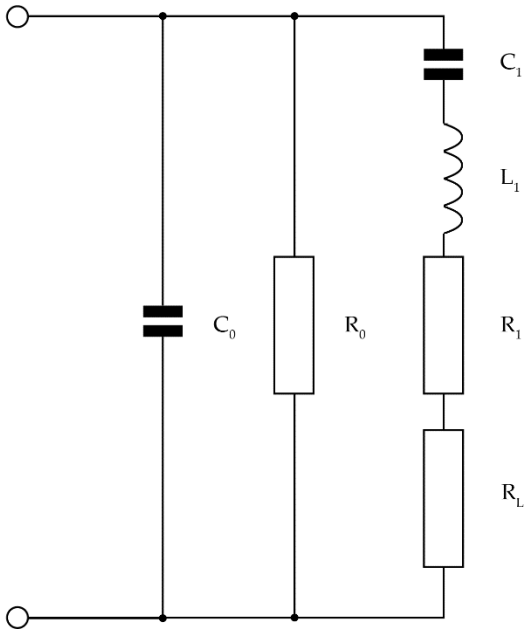

Figure 1.19 An equivalent circuit for a Transducer showing R1 which is the mechanical impedance, which acts as an offset resistance. C_1 is the capacitance of the mechanical circuit, C_0 is the capacitance of the transducer below resonant frequency less the capacitance C_1, L_1 is the inductance of the mechanical circuit, Adapted from [112]

1.7.2.3 Electro-mechanical coupling factor

The electro-mechanical coupling factor is the conversion between applied electrical power and the resulting mechanical power (transduction). It is relevant to acoustic work as it defines the input power to a system and that typically affects both form factor of a system and the heat created during operation. Heat which may be problematic if located adjacent to a sample such as in the case of a SAW device. An applied stress creates a charge within a piezo-electric material, and an applied electric field creates a stress and therefor strain. All three parameters

are linked and have properties which vary based on the orientation of the piezo electric unit cell to the applied stress or strain and it's Young's modulus (E). Considering the simple case of a disc transducer, not dissimilar to the device used in Section 3, equations (1.18) - (1.19) describe the relationship between stress and strain. The subscripts denote the axis of stress application and the axis of field measurement as shown in Figure 1.20:[113]

$$k_{33} = \frac{d_{33}}{\sqrt{\varepsilon_{33}^{T} S_{33}^{E}}} \tag{1.18}$$

$$k_t = h_{33}\sqrt{\frac{\varepsilon_{33}^{S}}{c_{33}^{D}}} \tag{1.19}$$

Where k_{33} is the coupling coefficient for an axial-planar stress along the 33 (z) axis, d_{33} is the piezo electric strain constant in m V^{-1}, ε_{33}^{T} is the permittivity at constant stress in F m^{-1}, and S_{33}^{E} is the elastic compliance under a constant electric field m^2 N^{-1}. k_t is the thickness mode where all strain is normal to the top and bottom surface of a disk. h_{33} is the piezo electric stiffness constant in V m^{-1}, ε_{33}^{S} is the permittivity at constant strain in F m^{-1}, c_{33}^{D} is the elastic stiffness under constant electric displacement in C m^{-2}.

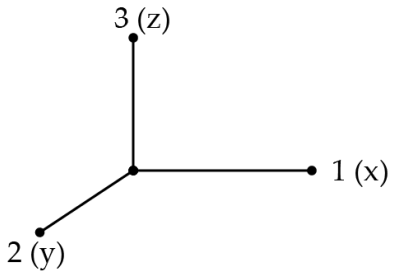

Figure 1.20 Polarisation axis

The coupling equations however begin to differ significantly as more complex modes are considered. However for practical applications the coupling constants are well established and provided by manufacturers so they may be found in reference tables. [114]

1.7.3 SAW uses and fabrication

Surface acoustic wave technology uses the Rayleigh surface wave, exciting it on a substrate capable of sustaining a true surface wave. Typically true surface waves attenuate the subsurface component of the wave within a few wavelengths (within the high frequency region), but will propagate a surface wave two or more orders of magnitude further. In the case of the piezo-ceramic crystals used within this work (lithium niobate 128 ° Y rotated, X propagating) the material is also orthotropic within the elastic-half space surface; this means that waves travel much like a light ray, with minimal spread. The dominant use for the technology include: telecoms as a delay line, chemical sensing as a mass sensor and gas sensor and also as a signal filters. The ability to create narrow resonance bands and strongly coupled fluid interactions has led to their use for particle manipulation covered in section 1.4).

2 Development of a standing wave protein-crystal mount

2.1 Chapter Summary

To develop a standing wave protein crystal mounting method, key specifications, parameters and constants were required. This chapter details the parameters as they were taken from literature, developed using analytic equations or approximated from calculated values. Where appropriate explanations have been included to assist the non-specialist in following the requirements which are drawn from acoustics, sedimentation mechanics, x-ray physics, and structural biology. The chapter concludes with a developed specification enabling the success of the device to be described.

2.2 Introduction

The first stage of a design process is to establish the requirements for the finished system. The following chapter sets out to identify and bring to the attention of the reader, properties and parameters that a successful standing wave based protein crystal X-ray presentation system will be subject to. By the nature of the work subjects from several fields are touched upon, including:

- Settling
- Crystallisation
- Acoustics
- X-ray Diffraction

For clarity, some of the background information on these subjects has been omitted and the reader is directed elsewhere for further discussion.

2.3 Geometric Constraints – The diffraction cone

Of the design inputs that need to be considered in the successful design of a protein crystal handling system, the angle at which diffracted light will leave the protein crystal is one of the most important. As the crystal is a 3D object, the light leaves the crystal at a solid angle, which is an angle that has been rotated around a central axis to form a cone as shown in Figure 2.1.

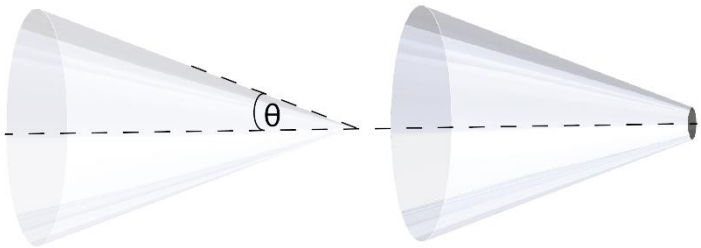

Figure 2.1 Conic and conic frustrum shown, rotated out of plane for clarity

It is important to understand and incorporate this angle as if the resulting cone intersects, some solid part of the device geometry, data will not arrive at the detector, an occurrence referred to as 'shading'. To establish the exit angle for the diffraction cone, the Bragg diffraction, Equation (2.1) to can be solved. [93]

$$n\,\lambda = 2\,d\,sin\,\theta \tag{2.1}$$

Where n is the order of diffraction, typically a value of one is used here due to the significant reduction in the power of higher order reflections for complex molecules; d is the inter-planar distance of the crystal; λ is the wavelength of light; θ is the diffraction angle. Taking the first order reflection (n = 1) one obtains a simplified version of Equation (2.1) for the inter-planar distance (resolution) in Equation (2.2):

$$d = \frac{\lambda}{2\ sin\,\theta} \tag{2.2}$$

Using Equation (2.2) it is possible to determine the conical region of 3D space that X-ray light travels through between the crystal and the detector. Entering the wavelength of light generated at I24 (λ), and the target resolution of 1 Å (d):

$$d = 0.1\ nm$$

$$\lambda = 0.07\ nm$$

$$\theta = 20.5\ ^\circ\ or\ 41\ ^\circ\ solid\ angle$$

The Bragg diffraction angle results gives and exit cone of 41 degrees, from this result any device must have an unobstructed exit cone to obtain data with resolution up to 0.1 nm. During the design phase, the exit cone should be considered for any position where a crystal

may reside; for a perpendicular flat channel, a conical-frustrum serves as a simple design guide provided all locations where a crystal may sit reside on the top plane.

2.3.1 Geometric Constraints – The beamline apparatus

The second set of geometric design constraints are the physical dimensions, interfaces and requirements of the beamline being used for studies and prototypes, pictured in Figure 2.2.

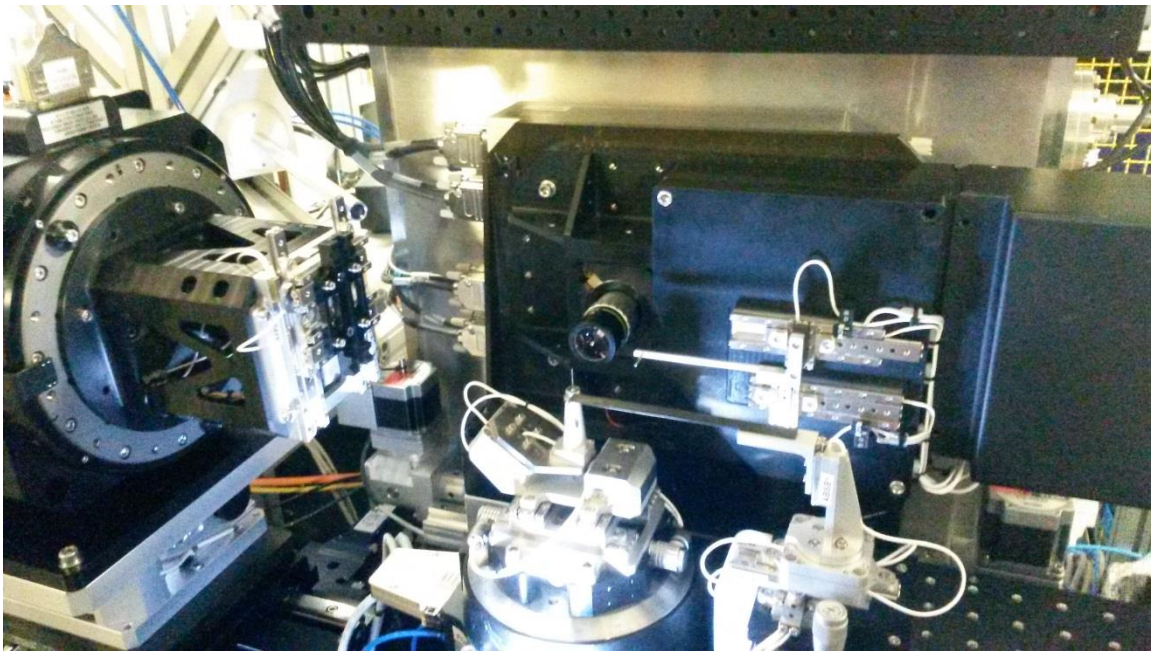

Figure 2.2 I24 beamline end-station apparatus

Figure 2.3 shows a three-dimensional CAD model of the I24 end-station. The model has been false coloured to identify specific systems: Pink shows the beam entrance point, with hole in the centre of the online beam optics; Orange shows the scatter guard, a tube positioned between the sample and beam optics designed to attenuate any diffraction (termed air scatter) that occurs before the beam hits the sample and useful data is generated, ultimately reducing background noise at the detector; Green shows the beam stop, as the name implies it is important to prevent the full intensity of the beam striking the detector as such an overload would cause damage to the pixels; Blue denotes the current sample holder arrangement, a

turret which forms a mount for a spine and pin as discussed in section 1.2; Teal describes the translation stages, incorporating x and y translation, Q rotation (the in-situ goniometer not shown) and vertical z axis (not shown) Finally yellow highlights a simple model of the HC1 humidity controller used in Chapter ◎ to prevent dehydration of small liquid drops, or more typically crystals.

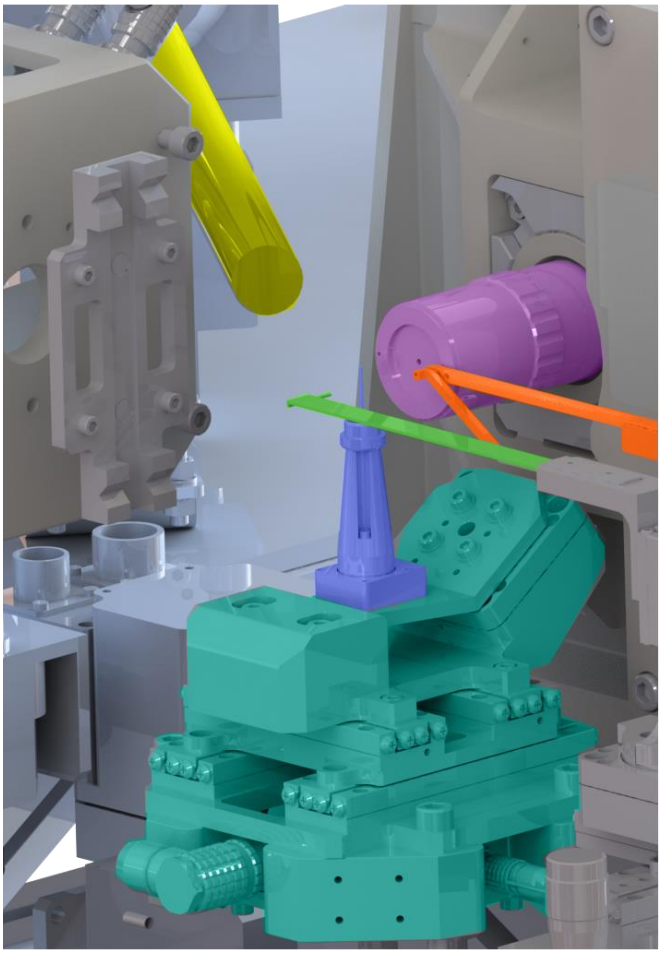

Figure 2.3 False coloured CAD model of I24 end-station – Models provided by Diamond Light Source

- Design inputs coming from existing physical apparatus are geometric and optical.
- Firstly a need for any device to fit around the beam stop and scatter guard
- A need to interface with the upper translation stage (teal)
- To allow any device to be moved into the on axis microscope's focal plane (pink)

- To be sufficiently transparent to allow sample observations to be taken by the on axis microscope (pink). Particularly important as due to the presence of ionising radiation, no-one may be in the room during operation.
- X, Y, Q and Z (vertical) translations comprising 20 mm, 20 mm 180 ° and 200 mm respectively.

2.4 Settling

2.4.1 Buoyancy of crystals

Settling and buoyancy are naturally linked, with the relationship being the prime factor in a system that has no flow. The buoyancy of crystals, size of the crystal and the properties of the working fluid determine the speed of settling and so the rate at which any imaging system is able to monitor them, and the force which must be overcome by the acoustic system.

Buoyancy is defined as:

$$F_{buoyancy} = \frac{\pi D^3}{6}\left(\rho_p - \rho_f\right) g \qquad (2.3)$$

Where D is the diameter of a sphere equivalent to the particle, g is gravity, ρ is the density of the particle (p) and fluid (f) respectively.

Several assumptions help to calculate buoyancy forces and settling: (i) the crystal will always be heavier than the surrounding fluid. (ii) the density of proteins is an active topic within the field of protein crystallography, with an approximately inversely proportional relationship between density, the unit cell structure, and molecular weight, however for the purpose of developing a general set of criteria an upper and lower figure of 1.32 – 1.45 g / cm^{-3} has been

used. [11], [115] (iii) density and viscosity of the working fluid is set by typical crystallography formulations, given the delicate nature of protein crystallisation substitutions are not possible.

Investigating the possible working fluids further, they are formed of water based solutions used as 'mother liquor' (precipitation fluid) in hanging and sitting drop experiments. While the fluids are water based they are altered to include salts, polymers, 'crystal glue' and cryo-protectants, all of which alter the density and viscosity.

Crystallographers develop and tune the crystallisation parameters for proteins of interest use a screening panel of common conditions. During the course of this project, a 96 well index produced by Hampton Research was selected as a test case for characterising devices, the screen contains a wide array of parameters. Without direct measurement of the solutions precise viscosity values were not available, however density figures could be readily obtained for the Hampton Research "Index Screen" [116].

Analysing the variability across solutions shows a density range for the 96 conditions of 0.236 g cm^{-3}, with an average, maximum and minimum of 1.072, 1.231, 0.995 g cm^{-3} respectively. Figure 2.4 is a histogram plotting the densities of all 96 solutions in the Hampton Research index screen.

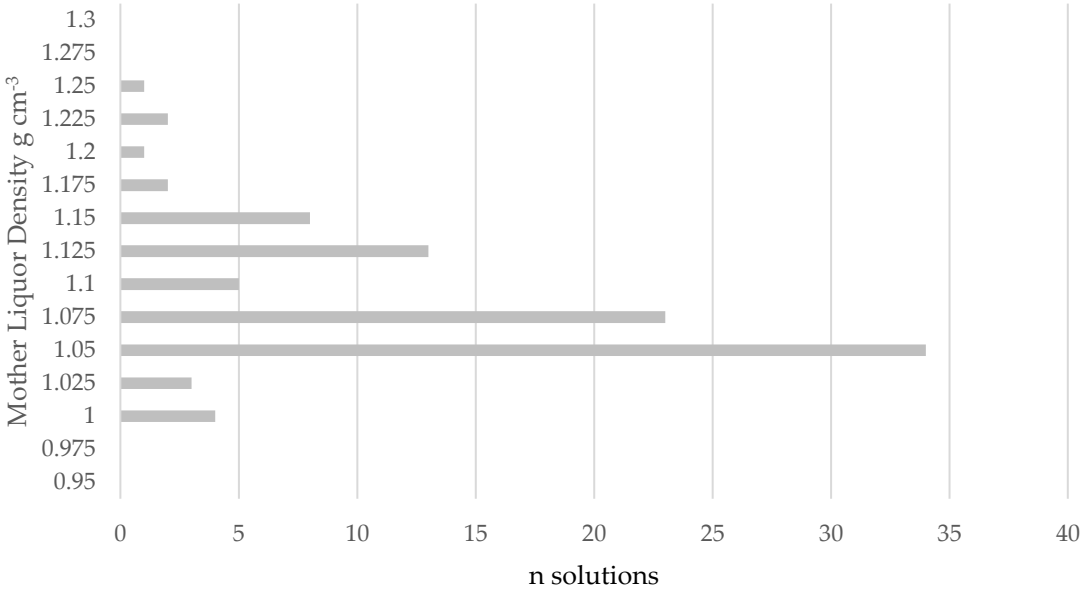

Figure 2.4 Density histogram of trial crystallisation conditions

The density data provides three important results, the density of the settling medium is higher than water, with the maximum being 127% of the minimum. Secondly, the assumption of crystals always being heavier than solution appears correct, with a difference spanning 0.089 to 0.455 g cm^{-3} depending on the value used for protein and solution respectively. From these figures an approximate range for buoyancy force can be calculated as shown in Figure 2.5.

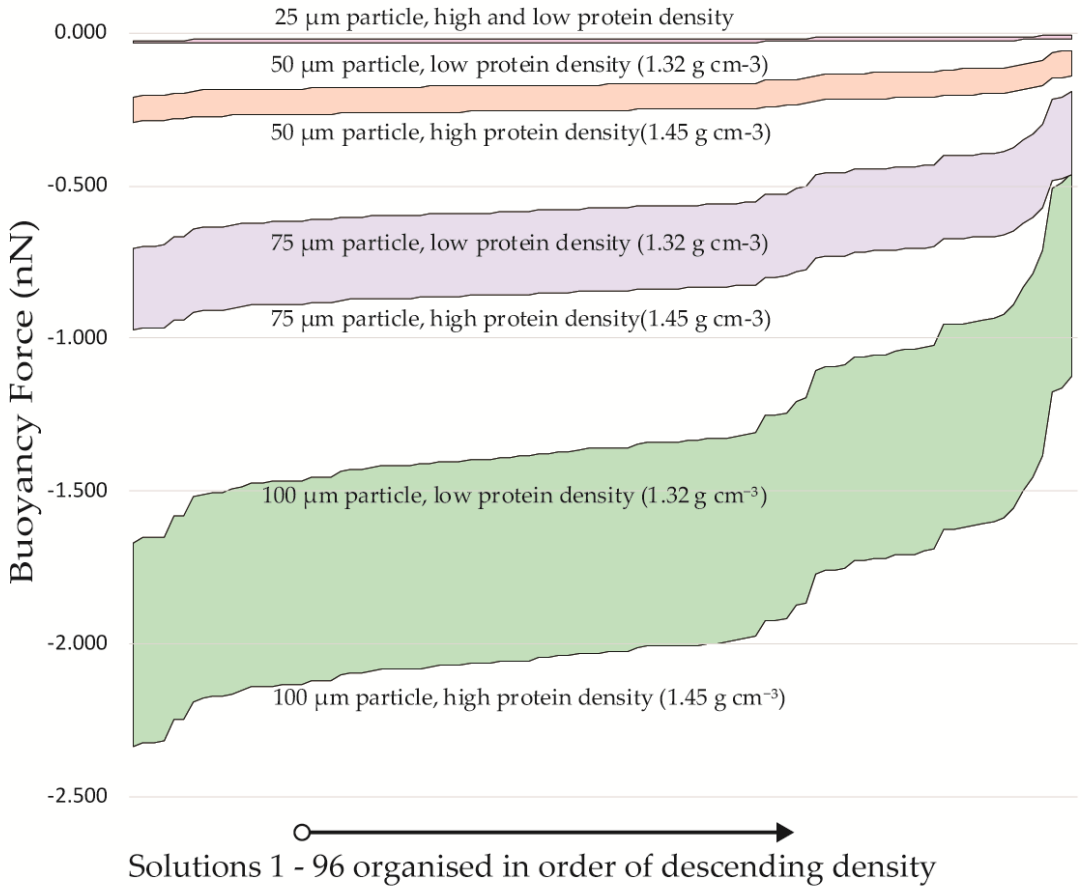

Figure 2.5 Buoyancy force of particle sizes 25 – 100 µm calculated using current approximations for protein density and crystallisation-condition-solution density, the 96 crystallisation conditions are arranged by decreasing density from left to right

After calculating the buoyancy force as plotted Figure 2.5, Table 2.62.1 and Table Figure 2.72.2 provide descriptive statistics on the buoyancy force as plotted in Figure 2.5. The source of the greatest difference, the particle size, is readily apparent causing a change that spans 4 orders of magnitude. Particle and the solution density combined effects typically lying within a single order of magnitude.

Table 2.62.1 Buoyancy force for particles 25-200 µm at the higher estimate for protein density

Particle Size (µm)	25	50	75	100	125	150	200

Protein Density ($g\ cm^{-3}$)	1.45	1.45	1.45	1.45	1.45	1.45	1.45
Min	-0.018	-0.141	-0.475	-1.125	-2.197	-3.797	-8.999
Max	-0.037	-0.292	-0.986	-2.337	-4.565	-7.888	-18.697
Range	0.019	0.152	0.511	1.212	2.368	4.091	9.698
Average	-0.030	-0.243	-0.819	-1.942	-3.792	-6.553	-15.534

Table Figure 2.72.2 Buoyancy force for particles 25-200 μm at the lower estimate for protein density

Particle Size (μm)	25	50	75	100	125	150	200
Protein Density ($g\ cm^{-3}$)	1.32	1.32	1.32	1.32	1.32	1.32	1.32
Min	-0.007	-0.057	-0.193	-0.457	-0.893	-1.543	-3.657
Max	-0.026	-0.209	-0.704	-1.669	-3.260	-5.634	-13.355
Range	0.019	0.152	0.511	1.212	2.368	4.091	9.698
Average	-0.020	-0.159	-0.537	-1.274	-2.488	-4.300	-10.192

As the working fluid and diversity of crystal sizes found in crystallography can be expected to affect a change spanning orders of magnitude, it is apparent that any crystal handling system oriented either vertically or horizontally, will experience multiple settling velocities, and would be at risk of settling induced blockage. This result is key to understanding the likely performance of a microfluidic system for protein crystals, and requirements for a complete system to include either automatic or manual sample selection by size prior to acoustic manipulation if consistent response is sought.

2.4.2 Settling – velocity

The need to consider settling velocity is one of the more unique elements of acoustofluidics for crystallography. Typically a microfluidic device is a 2.5D device, i.e. the device geometry

is formed of one or more flat layers. An advantage of flat construction is that gravity can be considered a constant in all X and Y coordinates (in plane), and so can be ignored, simplifying operation. Conversely, devices that take advantage of the ability of different size particles to settle at different rates, typically keep a constant flow rate, using fluid velocity to prevent settling in undesired regions of the device. In this project there is a need for almost stationary crystals, due to detector limitations and data requirements. Since a device must be oriented vertically (to avoid blocking) with a horizontal X-ray beam, a challenging design constraint arises as crystal velocity becomes a variable that is not governed by channel position (as would be typical in analytic and sorting devices).

An assumption and limitation of this work is that the particles are all spherical. This assumption is a known limitation, however given the diversity present within crystal precipitation fluids, and also the interesting and varied shapes that crystal may take on it was falls beyond the scope of this work. To add further context, crystal settling has a practical and appreciable effect in modern crystal handling often requiring innovation to ameliorate (For more detail on this see 'crystal shakers' at use for XFEL [86]).

Within the trapping portion of this work, extremely low Reynolds numbers occur, as such Stokes law may be applied, and the terminal velocity of the particles calculated using Equation (2.4). [117]

$$V_t = \frac{g\, d^2(\rho_p - \rho_m)}{18\ \mu} \qquad (2.4)$$

Where V_t is the terminal velocity, g is gravity, d is the particle diameter, ρ_p and ρ_m are the density of the particle and medium respectively, and μ is the dynamic viscosity.

Equation (2.4) may also be easily re-arranged to estimate the dynamic viscosity of the working fluid as shown in Equation (2.5).

$$\mu = \frac{g\, d^2\, (\rho_p - \rho_m)}{18\, V_t} \tag{2.5}$$

In expectation that crystals are likely to be large enough that they occupy a significant fraction of the channel and so reduce the overall settling rate, it is appropriate to introduce the 'Francis wall factor', a coefficient that models the decrease seen in narrow enclosures with low Reynolds numbers. The Francis coefficient was calculated using Equation (2.6) and applied using Equation *(2.6)*. Figure 2.8 shows the impact that the wall factor has dependent on particle or crystal size for the range of sizes expected.

$$f_w = 1 - \left(\frac{x}{D}\right)^{2.5} \tag{2.6}$$

$$V_{settling} = f_w \left(\frac{g d^2 (\rho_p - \rho_m)}{18\mu}\right) \tag{2.7}$$

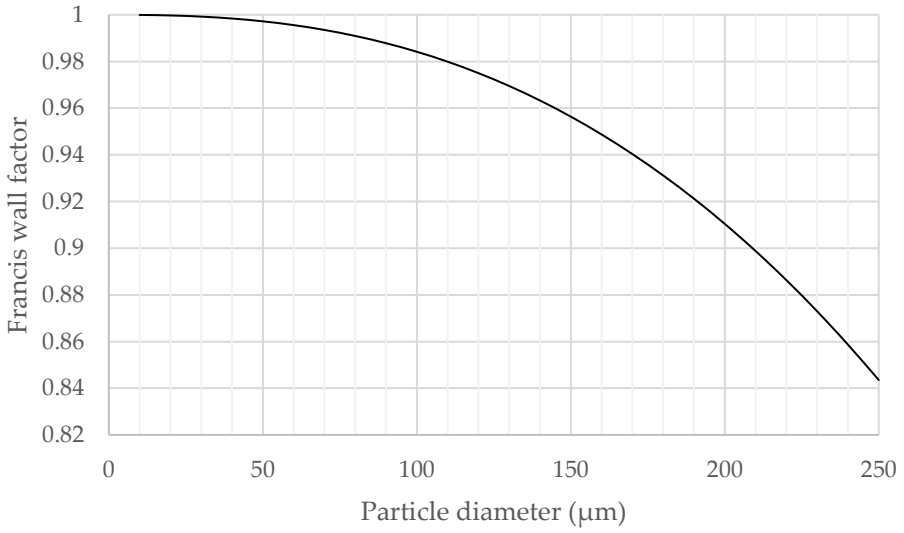

Figure 2.8 Francis wall factor settling chart for particles 0 - 250 μm in a 525 μm channel.

The viscosity of water was used to generate Figure 2.8 using the dynamic viscosity at 20 °C as an estimate for the properties of the crystallisation fluids

2.5 Speed of actuation

To provide an early estimate for the appropriate actuation speed for crystals within an active-mounting system, key parameters include: (i) frame rate of the detector; (ii) photon flux of the beam; (iii) beam cross sectional size and (iv) target number of images per crystal.

The first three parameters are to some extent selectable. The frame rate of the detector used (Pilatus 3 X 6M [118]) has a maximum full image capture rate of 100 Hz. The photon flux of the trial beamline was 3.0 x 10^{12} photons s^{-1} and the beam size was controllable between limits of 7 x 6 to 50 x 50 μm (i24 at Diamond Light Source, Didcot, Oxford - ibid). The photon flux may be reduced to achieve an acceptable power level for experiments.

Given the brightness of the beam, the photon flux does not form a limiting factor, and in-fact is capable of significantly higher brightness than protein crystals are able to sustain without significant radiation damage. Creating a simple model for the time spent in the beam path:

$$\text{Captured Frames} = \left(\frac{\text{Length of Crystal} + \text{Beam Width}}{\text{Crystal Translational Velocity}}\right) \cdot \text{Frame Rate} \qquad (2.8)$$

Using equation (2.8 and taking frame rate as 100 Hz, beam width as a fixed 6 μm and evaluating for crystal sizes 0 – 200 μm (denoted by the grey shading between maximum and minimum lines), in Figure 2.9:

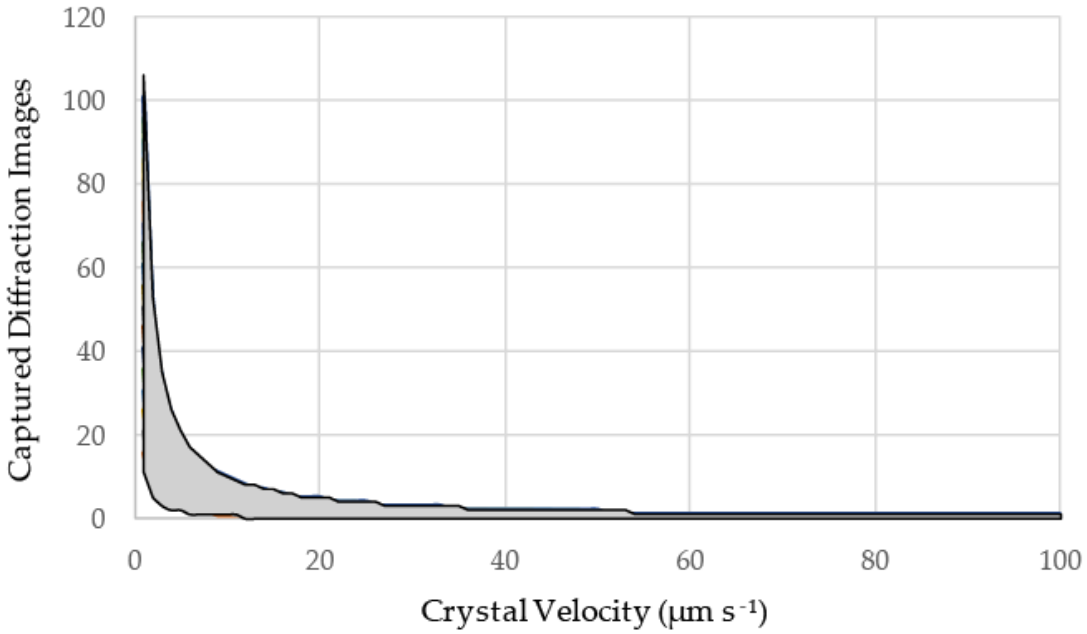

Figure 2.9 Plot showing possible data capture for crystal sizes ranging from 5 - 100 μm vs crystal velocity relative to the beam.

Figure 2.9 demonstrates that despite the desire for high throughput sample holders, there is a limiting factor in the detector sampling rate. Given a target number of images per crystal of over 1000, dependent on crystal size and radiation resistance, the desired translational velocity may be considered nil for single crystal techniques, and around 20 μm s^{-1} for serial methods.

2.5.1 Material attenuation

Of significant concern for any device is the effect that the materials and method of construction used will have on the quality of data attainable. This is exceptionally important in X-ray diffraction as beam attenuation and / scattering is often a limiting factor in the performance of a method.[53] The Beer-Lambert Equation (1.14), allows the calculation of the absorptivity of a given material, anticipating the impact that construction methods will have:

$$I = I_0 e^{-\mu\rho x} \qquad 2.9)$$

Where I is the resulting intensity, I_0 is the incident intensity, μ is the mass attenuation coefficient ρ is the material density and x is the path length through the material. For many compound materials the mass attenuation coefficient is not known, in this case a useful approximation is made by summing the atomic absorbance of the atoms present in the compound [15]:

$$\mu = \frac{N_A}{MW} = \sum_i x_i \sigma_{ai} \qquad (2.10)$$

Where N_A is Avogadro's number, x_i is the number atoms of type i in the compound, σ_a is the absorbance cross section.

Evaluating Equations (2.9) and (2.10) for common construction materials and comparing with photon energy (which is equivalent to wavelength) produces Figure 2.10. A region has been marked in grey showing values found in practice. Naturally the desire to maximise the signal

to noise ratio at the detector leads to a decrease in the path length of even the best performing material between a crystal and the detector.

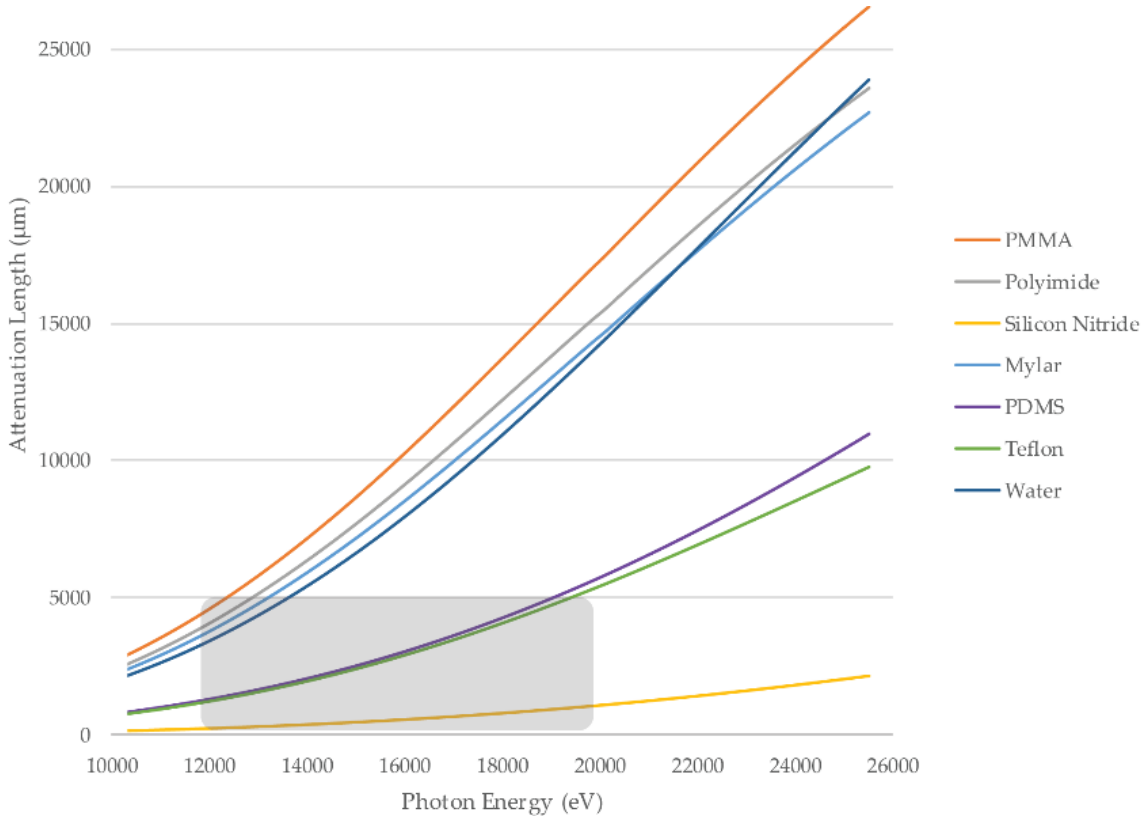

Figure 2.10 Plot showing extinction length vs photon energy, the grey region denotes typical construction.

The data in Figure 2.10 shows that three bands of materials with PMMA, polyimide (such as Kapton) and Mylar being good candidates for thick construction with the longest extinction path length of approximately 4 to 15 mm in the relevant energy range; PDMS and Teflon with excellent ease of construction and antifouling properties respectively, having an extinction path length of approximately 2 to 5 mm; Finally silicon nitride appears to significantly underperform other materials with < 2 mm extinction path for all relevant photon energies. Current MX methods frequently make use of silicon nitride however, by chemically etching a down to a ≤ 1µm thick layer of this hard and glass like material, several orders of magnitude thinner than its competitors. Windows can be purchased commercially and can be found in

transmission electron microscopy (TEM). Each of the materials included in Figure 2.10 possesses practical characteristics such as availability, ease of manufacture and anti-fouling.

2.6 Acoustics

The following sections detail estimates for the operational conditions for driving the acoustic phenomena. Ultrasound was used throughout the experimental portion of this thesis, any frequency beyond the range of human hearing is encompassed by this term. The frequencies discussed in Sections 3, 4 and 5 are described properly as 'high-frequency' category in radio terminology, being between 3 - 30 MHz.[111]

2.6.1 Change in the speed of sound in water due to temperature

Speed of sound in water at various temperatures, the speed of sound in water varies with temperature. The variation arises from a change in the viscosity of water due to temperature. The range of the speed of sound can be seen in Figure 2.11 adapted from work conducted at NIST [119]:

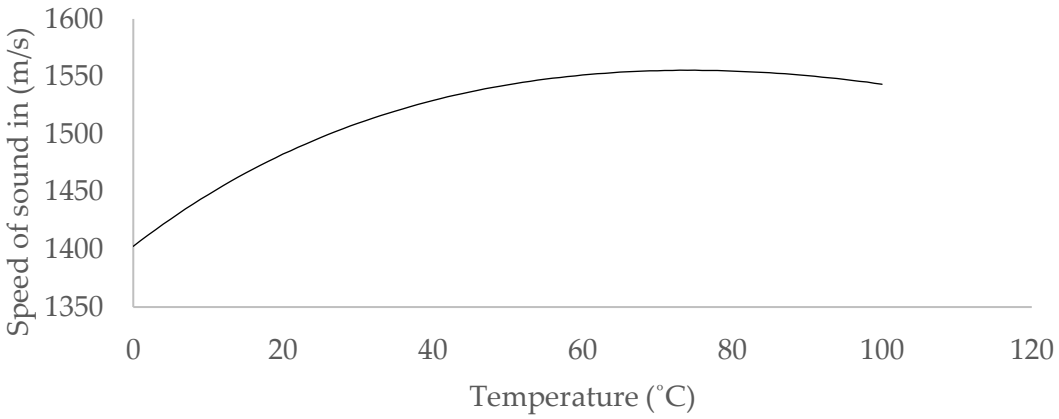

Figure 2.11 Speed of sound in water plotted against temperature.

The minimum and maximum being 1402 and 1555 m s^{-1} respectively give a percentage change > 11 %, and a range in wavelength at 25 MHz of 56 – 62 μm. this range can be narrowed in the context of macromolecular crystallography as the low and high temperature regions would create challenging conditions for crystal survival. However even for a single wavelength this suggests a movement from the optimum $n \cdot \lambda/2$ positions as discussed in section 1.7.1, for wall sections spanning distances equivalent to multiple wavelengths it risks the resonance moving to an antinode. Because of this constant change the need for a swept signal is necessary until such a time as calibrated-temperature feedback can be incorporated into the control loop.

2.6.2 Transmission and reflection of the proposed system

The transmission and reflection coefficients for the wave arriving at the silicon for the near-optimal arrangement X-ray transmission arrangement used in section 3 have excellent reflection properties due to the contrasting acoustic impedances of selected silicon and crystallisation fluids.

2.6.3 Speed of sound calculation for compressional waves in a silicon lattice.

Sound travelling through crystalline media has a wavelength which is determined by the direction of propagation, due to the anisotropic elastic constants. The constants

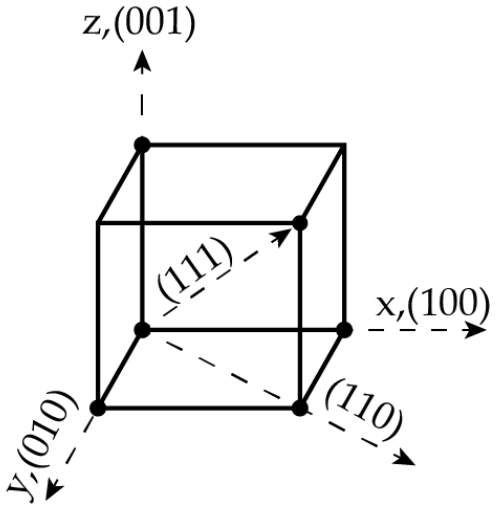

Figure 2.12 Cubic lattice notation.

The speed of sound in the 110 direction, as pictured in is calculated using Equations (2.11) to (2.13).[19] The directional stiffness constants used were $C_{11} = 1.66$, $C_{12} = 0.639$, $C_{44} = 0.796$ (all × 10^{11} N m^2), and density was taken as $\rho = 2328$ kg m^{-3}.

$$\omega^2 \rho = \frac{1}{2}(C_{11} + C_{12} + 2C_{44})K^2 \tag{2.11}$$

$$U_{110} = \frac{\omega}{K} = \sqrt{\frac{\frac{1}{2}(C_{11} + C_{12} + 2C_{44})}{\rho}} \tag{2.12}$$

$$K = \frac{2\pi}{\lambda} \tag{2.13}$$

The result gives the longitudinal wave speed in the (110) direction as significantly faster than the (100) direction at 9141 m s^{-1} and 8430 m s^{-1} respectively. [120] The calculated velocities are used in Section 2.6.4.

2.6.4 Acoustic reflection

The dominant concern for acoustic interaction with a fluid volume is the ability to have acoustic power arrive at the volume in sufficient quantity to achieve the desired 'work'. A useful tool to evaluate the likely performance of the silicon chambers are the transmission and

reflection equations. The governing equations for reflection are restated as outlined in Section 1.7.1.5 are reproduce as Equations (2.14) - (2.17) for clarity.

Amplitude (also giving the phase at the point of reflection):

$$t_s = \frac{p_t}{p_i} = \frac{2\,Z_2}{Z_1 + Z_2} = \frac{2\,\rho_2\,c_2}{\rho_1\,c_1 + \rho_2\,c_2} \tag{2.14}$$

$$r_s = \frac{p_t}{p_i} = \frac{Z_2 - Z_1}{Z_1 + Z_2} = \frac{\rho_2\,c_2 - \rho_1\,c_1}{\rho_1\,c_1 + \rho_2\,c_2} \tag{2.15}$$

Power:

$$t_p = \frac{p_t}{p_i} = \frac{4\,Z_1\,Z_2}{(Z_1 + Z_2)^2} = \frac{4\,\rho_1 c_1\;\rho_2\,c_2}{(\rho_1 c_1 + \rho_2 c_2)^2} \tag{2.16}$$

$$r_p = \frac{p_t}{p_i} = \frac{(Z_2 - Z_1)^2}{(Z_1 + Z_2)^2} = \frac{(\rho_2\,c_2 - \rho_1\,c_1)^2}{(\rho_1\,c_1 + \rho_2\,c_2)^2} \tag{2.17}$$

Where t_s and t_p are the transmission constants for amplitude and pressure respectively, r_s and r_p are the reflection constants for amplitude and pressure respectively, Z is the acoustic impedance of medium 1 or 2 as denoted by subscript, ρ is the density and c is the speed of sound for the medium also denoted by subscript. Figure 2.13 shows the power transmission and reflection for silicon (100) and (110) and water for a normally incident wave:

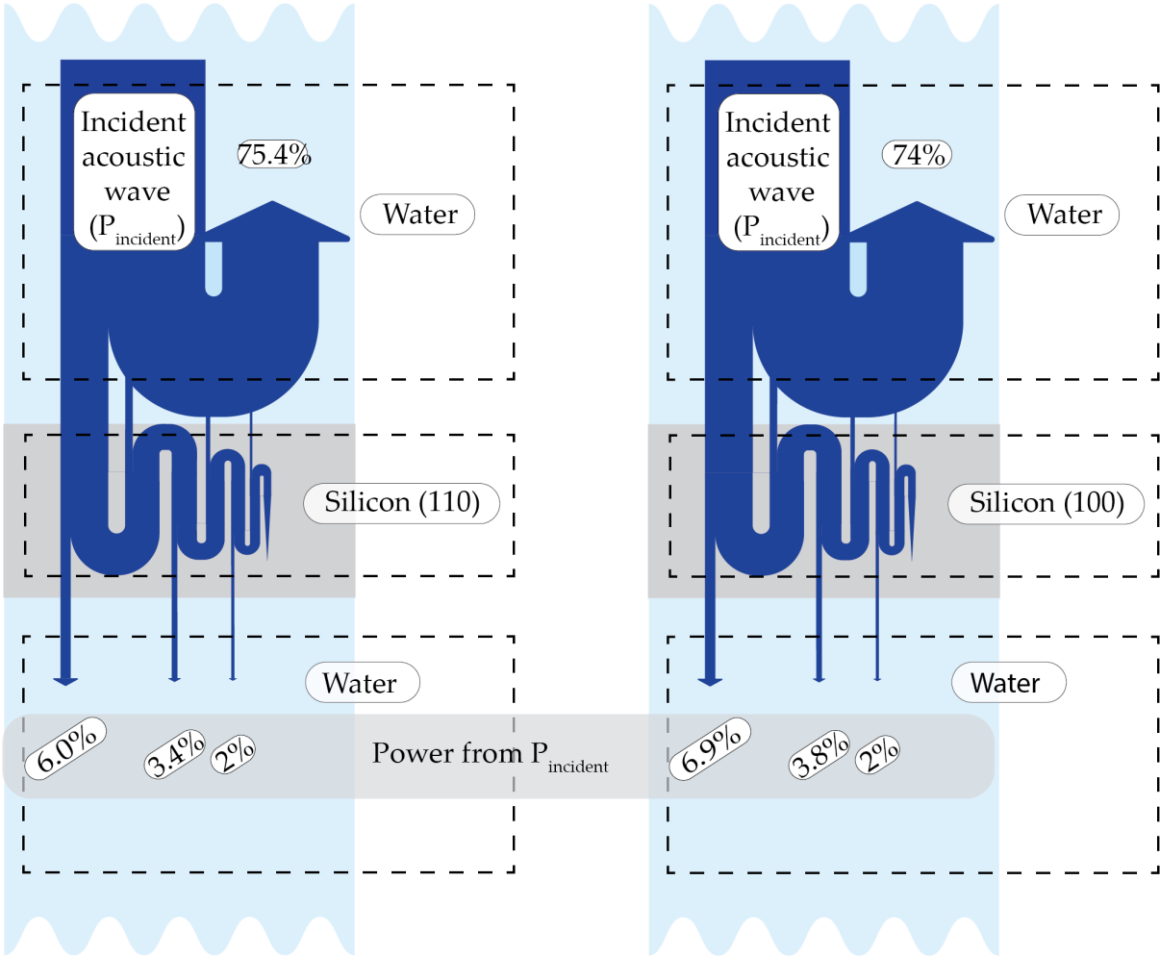

Figure 2.13 A Sankey diagram showing the first three transmissions through a water-silicon-water boundary for a normally incident wave.

While silicon nitride makes an outstanding X-ray compatible chamber, the ≈75% reflection at the boundary suggests that an impedance matching layer would be a significant improvement to the experimental arrangement, it was not possible to develop one as part of this project however.

2.6.5 Sound interaction with the silicon nitride layer

Since sound is propagating from high speed of sound region to a low speed of sound region, total internal reflection does not occur in spite of the strong aspect ratio. However to evaluate the loss to air through the silicon nitride membrane at maximum (a normally incident wave), and taking the value for the speed of sound in PEVCD silicon nitride to be 9900 m/s and a

density of 2500 Kg m^{-3} gives a reflection coefficient of >99% against the air boundary (PEVCD stands for plasma enhanced vapour chemical deposition).[121]–[123] This result is expected due to the significant differences in the relative acoustic impedances.

2.7 Operational-design inputs

Through consideration of the macromolecular crystallographic sample environment the following list of design requirements for the standing wave trap were generated:

- Sufficient acoustic pressure to enter the fluid cell to allow the excitation of a standing wave within the fluid.
- Multiple wavelengths contained within a single window, allowing for an array of crystals to be trapped.
- The presence of sufficient acoustic force to cause the trapping of protein crystals.
- The retention of crystals within a stable trapping position for a duration allowing their targeting and diffraction.
- A stable form of trapped-crystal motion allowing effective beam targeting.
- The arrangement of a fluid cell which was capable of sustaining a standing wave.
- The arrangement of a fluid cell which was sufficiently transparent to X-rays to allow scattering data to escape enabling < 2 Å data collection.
- Developed fluid cells must be inert relative to the crystallisation fluid and the crystals themselves.

3 A bulk-acoustic standing wave protein crystal mount

3.1 Chapter Summary

The following chapter details a fabricated bulk standing wave protein crystal, where work was undertaken to trap protein crystals in a vertically-orientated acoustic field, while they remain at room temperature and in crystallisation fluid (also referred to as a crystallisation condition, or mother-liquor). The chapter includes details of the specification, fabrication and testing of the device. During the work, challenges specific to the acoustic trapping were identified and discussed for the first time. Topics presented cover: Acoustic transducer performance, examining the design with respect to operation, data acquisition quality and type, wavelength, and the crystal response to the applied acoustic field. Finally, the discussion covers the integration and operation of the device on a beamline.

3.2 Introduction

Self-ordering systems offer a way to overcome many significant challenges present at the sub-micrometre length scale. Many techniques require the presence of fluid and so are a natural choice for incorporation into lab-on-chip technologies. High throughput methods require the ability to find analytes quickly, incorporation of a self-ordering system can be a step towards this. In protein crystallography, the need to expand understanding of how protein structures look and act at room temperature has placed developmental pressure on current high throughput methods, which typically rely on robotic handling of single crystals. A natural consequence of the move towards higher temperature diffraction is an increase in radiation damage that would have previously been prevented under cryogenic conditions. The increased damage implies that more crystals must be imaged and for less time to achieve a high quality structure. Macromolecular Crystallography (MX) is also concerned with the resolution of data achieved, affected by crystal quality, attenuation by any surrounding material and background scatter caused by material in and around the crystal undergoing diffraction. In recent years, significant work has been undertaken to optimise background scatter and investigate mounting methods. High frequency acoustics ($1 < \omega < 30$ MHz) have wavelengths comparable to the crystal size and have been shown to be capable of exerting sufficient force to manipulate objects within their field. Bulk acoustics developed from 'soft' piezo types offer a wider frequency response to surface-acoustic-wave transducers, and can readily be adapted and operated to produce a high power output thus making any final system more resilient.

To generate a complete set of diffraction patterns, an electron density map (and from this a molecular structure) a crystal, or multiple crystals must be oriented and rotated to capture

reflections on a two-dimensional detector. This is routinely achieved through hand mounted crystals, ancillary equipment and mechanical goniometer (conforming to the Stanford Auto Mounting System standard, SAMS or similar). [21] An alternative approach to data collection utilises serial methods where single detector snapshots of large number variously oriented crystals (1000s).[124] Higher resolution structure determination available from third generation synchrotrons and enhanced data processing, and the ability to undertake hydration studies has led to renewed interest in room-temperature structures.[125], [126] Manufacturers now produce a series of *in situ* crystallisation plates that are diffraction compatible, enabling room temperature and native environment screening.[66] these method have been extended by authors who have optimised the material construction and developed the field of fixed target data acquisition.[61], [127], [128] The following work remains within this vein but attempts to simplify components and take advantage of acoustic phenomena. The work also focuses on room temperature techniques to help to avoid artefacts or structure degradation induced by cryo-cooling. [126],[129]

The self-assembly potential of bulk-driven standing wave acoustics has been widely demonstrated, most heavily in high-throughput cell sorting applications.[71], [130]–[132] Device operation is governed by mode shape, which is the position of the high and low amplitude points of a standing wave, and may form a one, two or three-dimensional field. Common modes demonstrated include horizontal half, single and multiple wavelength one-dimensional acoustic fields, and two-dimensional multiple wavelength fields.[133]–[135] One-dimensional vertical bulk-standing-acoustic fields have also been trialled to levitate protein crystals for diffraction in air.[136] A study was conducted on the effect and practicality of acoustic manipulation of protein crystals in an offline setting, providing further evidence that acoustics are suited for rapid crystal mounting. [137]

Authors have demonstrated it is possible to offset and rotate the excitation source from the target of the standing-wave field, allowing the use of lower cost generic transducers. [138] Acoustic trapping and manipulation has been demonstrated on delicate samples including: mammalian cells, fluid droplets and living worms, with no adverse effects reported.[139]–[141]

The following work demonstrates and describes the diffraction of protein crystals which have been trapped in a two-dimensional vertically oriented acoustic field. A bulk acoustic transducer is used to initiate the self-assembly by exciting a standing wave within a fluid cell optimised for X-ray transmission, and containing protein crystals. Diffraction has been demonstrated while crystals are subject to the acoustic trap and analyse the devices performance has been assessed using both X-ray and lab-based methods.

3.3 Methodology

3.3.1 Acoustic Design

One-dimensional chamber resonance was evaluated with respect to temperature and wavelength in section 2.6, producing the characteristic wavenumbers shown in Table 3.1. Several assumptions were made within the calculation: the speed of sound was assumed to be within the range of 1466 and 1509 ms^{-1} based on the speed of sound in pure water.[119] Incident soundwave was selected as vertical as it negated the refraction caused by the silicon nitride walls. Table 3.1 then lists the maximum and minimum frequency required for a simple one-dimensional resonance. Further, the results can be used to ensure that a transducer is suited to either directly driving the required frequency or is capable of working at a higher harmonic that may excite the lower mode. Further use of Table 3.1 in defining the sweep range

is required to ensure persistence of the resonance as temperature changes and small changes to alignment alter the natural frequency. As described in section 2.6, the sweep range was set to 0.5 MHz. Equation (3.1) restates the relationship between wavenumber, chamber dimension and the speed of sound.

$$\omega_{resonance} = \frac{n \cdot U_{acoustic}}{l} \tag{3.1}$$

Where ω represents frequency, U is the acoustic velocity, n is the wavenumber, l is the characteristic length of the cavity. The resonance modes available within the selected fluid cell are approximated to Table 3.1:

Table 3.1 Table of maximum and minimum wave numbers possible between angled walls of a 4 mm silicon/silicon nitride chamber.

	T (˚C)	15	20	25	30	
	Speed of sound (m/s)	1466.25	1482.66	1497.00	1509.44	
	L water (μm)	Resonant frequency at wave number n (MHz)				Wave number (n)
Min	4000.00	24.56	24.83	25.07	25.28	67
Max	5034.31	24.47	24.74	24.98	25.19	84
Δ	1034.31	-0.09	-0.10	-0.10	-0.10	

3.3.2 Fabrication

Figure 3.1 shows the device offline without labelling or obscuring features. A schematic of the experimental arrangement is shown in Figure 3.2 with exaggerated relative size of components, separation distance between the transducer and the fluid cell, and also the thickness of the silicon nitride layer scaled for clarityFigure 3.3. The beam mount comprised of a bulk acoustic wave transducer (Videoscan, 25 MHZ, Olympus, JP) secured into a 3D-printed housing, designed to locate fluid cells directly above the transducer and in line with the focal plane of the on-axis optics. Further, the silicon nitride trap was aligned with an unobstructed path for the x-ray light. Silicon nitride membranes (Silson 525 μm 1000 nm) were paired to form a small volume capable of maintaining a fluid seal. Membranes were bonded to a mounting wand. The completed arrangement is pictured in Figure 3.3, with labels added for clarity.

Figure 3.1 Un-mounted device

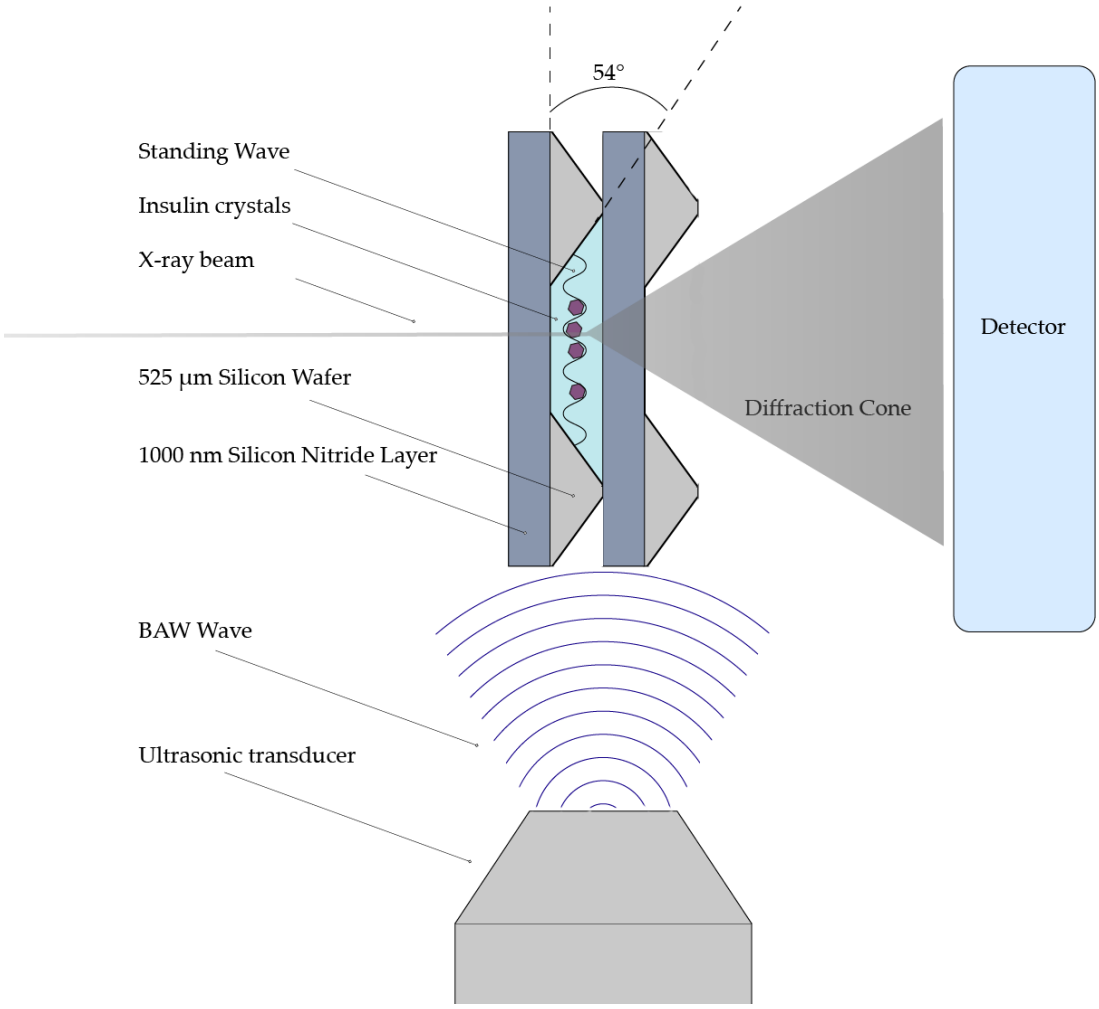

Figure 3.2 Schematic representation of bulk wave excited acoustic trapping experimental setup. Note the 1000 nm nitride layer is significantly enlarged to aid visualisation and is 1 / 500th of the thickness of the silicon layer in practice.

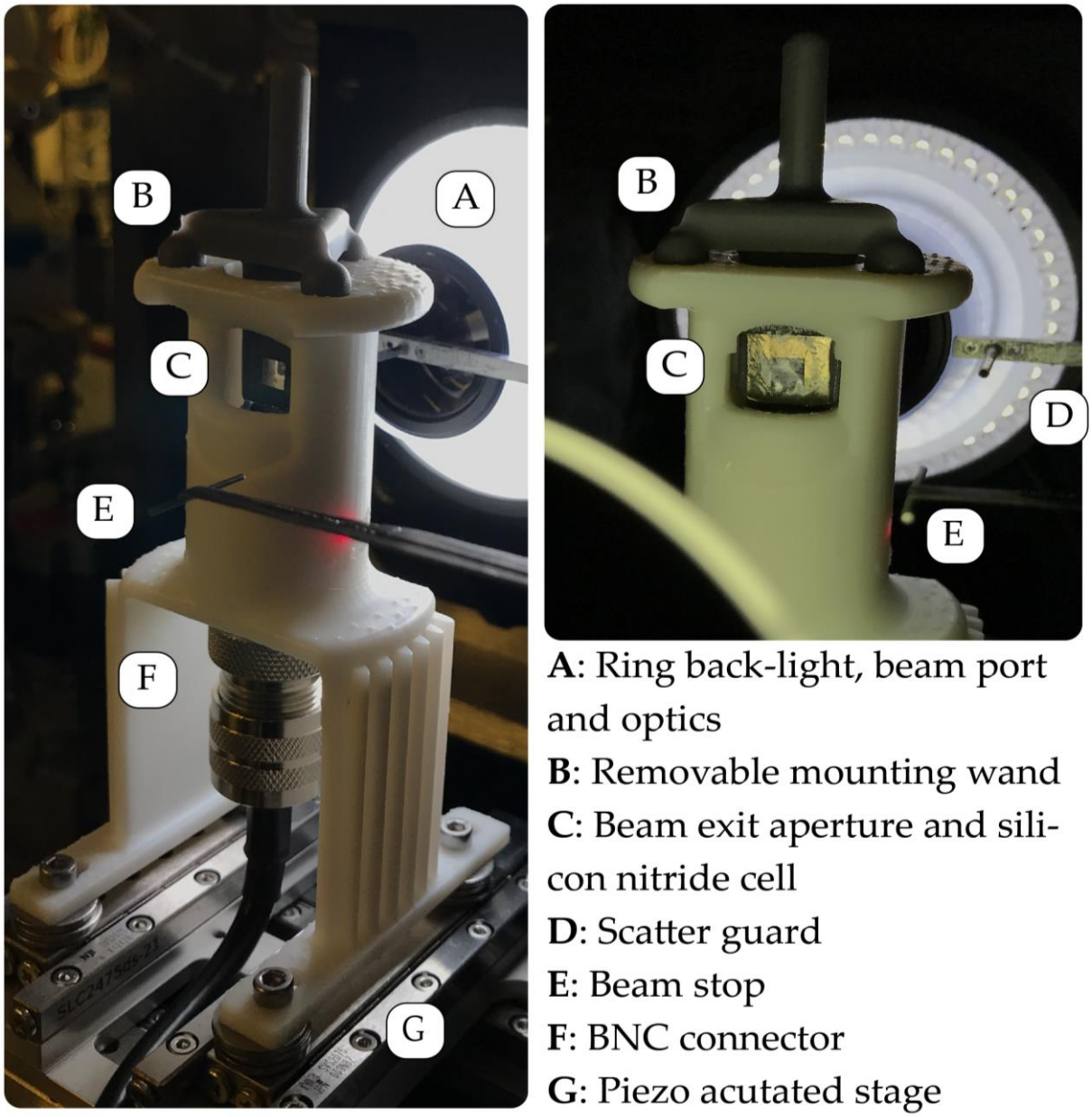

Figure 3.3 Excitation apparatus and sample mounted on a goniometer, scatter guard is in position, with the beam stop removed.

3.3.3 Determination of Background Scatter

To determine the effect of device construction on the ability to obtain data during diffraction experiments, individual diffraction frames were taken from and processed to find detector pixel background intensity levels. Data were processed using ALBULA (Version 3.3), a

proprietary software written by the detector manufacturer (Dectris, SWI). 2D scattering patterns, as shown in Figure 3.4 were processed by averaging the pixel intensity at a given radius from the recorded centre of the image. A 1D plot can then be produced from the resulting averages as shown in Figure 3.5.

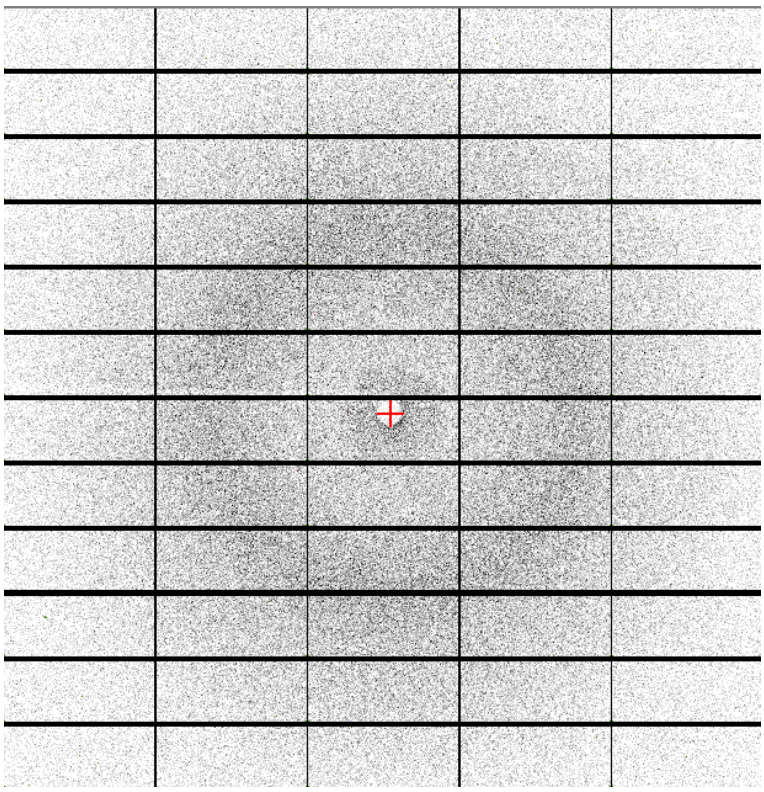

Figure 3.4 (a) Example diffraction frame (captured during study NT 14493-100) showing a typical background scatter pattern.

The X-ray must be normalised to allow comparison between data collected at different times (sometimes this can be many months apart). Further, it is useful to draw a baseline to describe the effects of any experimental construction. Given the varying methods trialled a simple air scattering background was chosen for comparisons. The air scatter demonstrates the background noise that would be seen if no sample were present in the beam path. Air scatter

is a weak effect when compared to the scattering behaviour of solids and liquids, so the relative increase of background scatter is not concerning.

All X-ray data on background scattering in this thesis have been presented as normalised plots showing background scatter against the solid angle (the angle that describes a cone starting at the sample and finishing at the detector at a given radius).

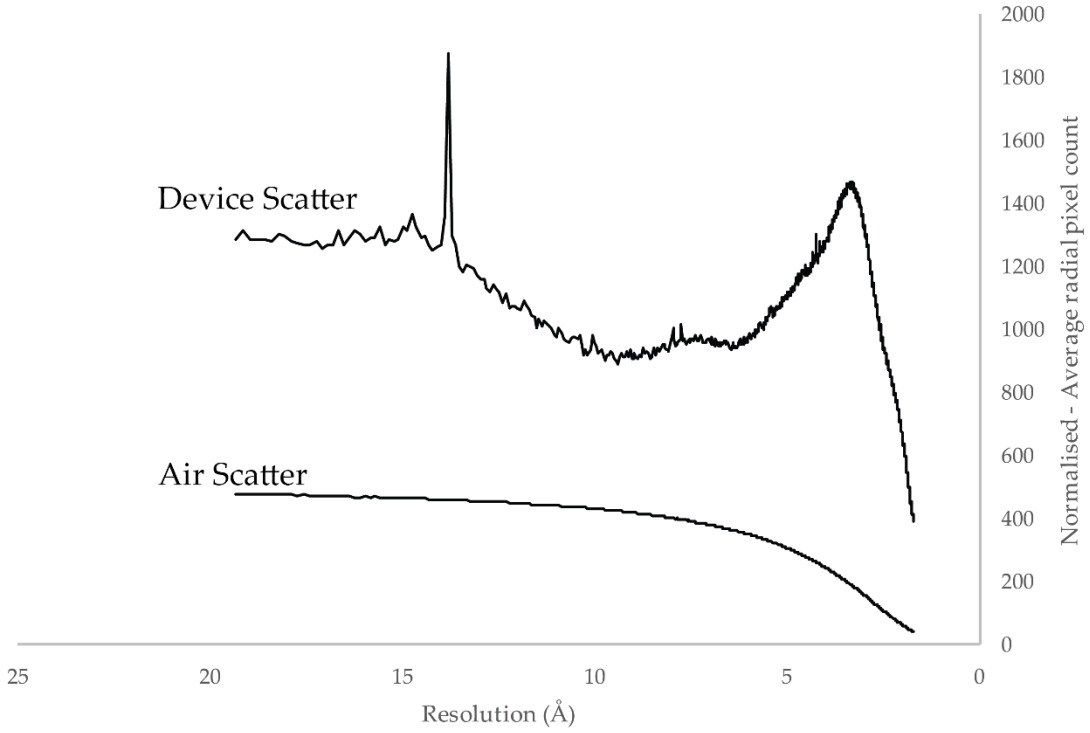

Figure 3.5 Plot showing data as pixel counts using air scatter as a baseline and the background scatter collected during the experiment as normalised to the air scatter collection conditions

It is common for key parameters to be varied during typical data collection, particularly when collection periods are separated by a period of months. These parameters include:

- Flux (the number of photons per second).

- Exposure time (length of time a pixel may receive photons e.g. for a framerate of 100 Hz, approximately 0.009 s, with a shutter time of 0.001 s).
- Filter, where the beam is directly attenuated rather than reducing power at the undulator stage.

To normalise the scattering data each of the above factors were included, essentially providing a 'normalised at sample' radially averaged pixel intensity count as shown in Equation (1.8).

$$\frac{Normalised\ intensity}{at\ detector\ (1\ Hz)} = \frac{recorded\ average\ radial\ pixel\ intensity}{(flux\ \cdot exposure\ time\ \cdot filter)} \tag{3.2}$$

The result of (3.2 gives a pixel intensity value that is very high in comparison to typical experimental conditions. A scaling factor was then added resulting in Equation (3.3 which gives the normalised observed background scatter for each detector still when full beam power is used and the detector is run at 100 Hz, this was done to make numbers more comparable with literature.

$$\frac{Frequency\ normalised\ intensity}{at\ detector\ (100\ Hz)} = \left(\frac{recorded\ average\ radial\ pixel\ intensity}{(flux\ \cdot exposure\ time\ \cdot filter)}\right) \cdot 0.01\ s \tag{3.3}$$

Finally, it should be noted that in the background scatter analysis, full range plots are shown, the region of interest is the < 5 Å region, which is shown in sections 3.6.2 and 5.5.2.

Of experimental interest is the relative inability to remove air scatter from the background noise in experiments conducted in air. It is possible to improve the signal-to-noise ratio by incorporating helium atmospheres or vacuum [142]. Practically the use of a tungsten scatter guard and beam-stop offers some reduction in air scatter. Incorporation of these components into a microfluidic device may allow for further improvement by precisely locating a tungsten

beam stop at an optimal distance from the sample exit and a pinhole scatter guard at < 50 μm from the sample.

3.3.4 Crystal-acoustic interaction

Crystals are attracted to either the standing wave node or anti-node depending on the affinity of the crystal. The affinity of the crystal for either nodes or anti-nodes (minimum and maximum pressure amplitude, respectively) depends on the density and compressibility of the crystal and medium as shown in Figure 3.6.

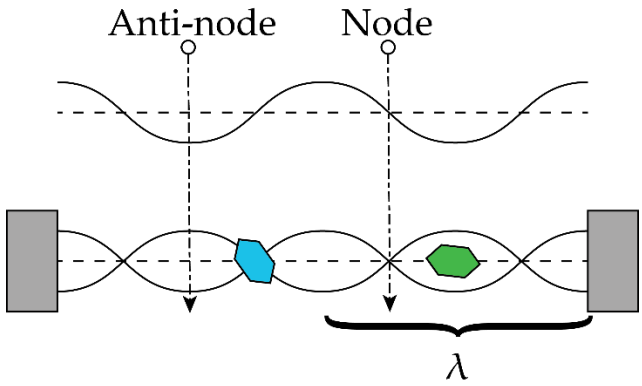

Figure 3.6 Example of node, and anti-node of a standing wave with particle preference shown below. A positive acoustic contrast factor is shown in blue with a preference for the node position, a negative acoustic contrast factor is shown in green with a preference for the anti-node.

The analytic solution to acoustic radiation force on a particle (which includes the acoustic contrast factor) produced by Yosioka and Kawasima provides an analytical model for the force experienced by a particle in an acoustic field, reproduced here in Equations (3.4 and (3.5.[143] As noted in several works, the acoustic contrast factor $[\phi(\beta,\rho)]$ is linked to the speed of sound difference between the medium and particle. [144]–[146] The sign (+/-) of Equation (3.5) gives the affinity of a particle to a node or anti-node.

$$F_r = -\left(\frac{\pi P_o^2 V_p \beta_m}{2\lambda}\right)\phi(\beta,\rho)\cdot\sin(2kx) \tag{3.4}$$

$$\phi(\beta,\rho) = \frac{5\rho_p - 2\rho_m}{2\rho_p + \rho_m} - \frac{\beta_p}{\beta_m} \tag{3.5}$$

Where F_r is the radiation force, P_o is the acoustic pressure, V_p is the volume of the particle, β_m and β_p are the compressibility of the medium and particle respectively, λ is the wavelength of the standing wave, $\phi(\beta,\rho)$ is the acoustic contrast factor and ρ_m and ρ_p are the density of the acoustic medium and particle.

Despite no values being published for the acoustic contrast factor or the compressibility of protein crystals, it is possible to interrogate Equation (3.5). Equation (3.5) may be alternatively expressed as follows in Equation (3.6): [139]

$$\Phi = \frac{\rho_p + \frac{2}{3}\left(\rho_p - \rho_0\right)}{2\,\rho_p + \rho_0} - \frac{1}{3}\frac{\rho_0 c_0^2}{\rho_p c_p^2} \tag{3.6}$$

Where Φ is the acoustic contrast factor, ρ_p and ρ_0 are the densities of the particle and the medium, and c_p and c_0 are the speed of sound in the particle and medium respectively. The advantage of such a change is the substitution of the compressibility term, whilst the speed of sound is also challenging to measure for small and variable samples, it is perhaps easier to estimate.

Trialling bulk keratin (the protein forming hair) as an indicative substitute for the unknown values (which are expected to vary according to protein and crystal type) offers useful

insights.[147] Keratin has a reported density of $\rho_{keratin} > 1300$ kg m^{-3} and $U_{acoustic} > 2800$ m s^{-1} (note the density value for keratin is comparable to the stated density for the protein in Section 2.4.1 and the speed of sound is comparable to PEEK and PMMA [148]). The resulting contrast factor in bulk water ($U_{acoustic} > 1500$ m s^{-1} and $\rho_{water} > 1000$ kg m^{3}) is $\Phi = 0.343$. A positively signed contrast suggests an affinity for nodal positions and, within the limits of the approximation, further demonstrates a value that is three times larger than the recorded acoustic contrast for successfully manipulated mammalian cells ($\Phi \leq 0.11$).[139] Extending the approximation to include the highest density crystallisation fluid described in Section 2.4.1 ($\rho_{fluid} > 1220$ kg m^{-3} and $U_{acoustic} > 1500$ m s^{-1}) yields $\Phi = 0.271$. As such, the acoustophoretic contrast factor is expected to remain positive and the affinity to be towards a position of lowest pressure amplitude.

3.3.5 Fluid cell and acoustic field interaction

Experimental verification of acoustic paths is experimentally challenging, therefore the following work makes the assumption that the acoustic path theoretically offering the most efficient power transfer would be the dominant mode of operation in practice. The verification of the acoustic path was achieved through the subsequent trapping wavelength observed within the trapped volume, recommendations for the analysis of waveforms, and for the improvement of acoustic power transfer are included in Section 6. A schematic of the experimental arrangement is shown in Figure 3.2. A swept sinusoidal excitation wave is generated using a commercially available ultrasonic transducer (25 MHz Olympus Videoscan, Olympus, JP). The wave is incident to the bottom of the paired silicon nitride cells. A portion of the wave is then reflected at the boundary, the remainder of the energy passes into the silicon wafer and goes on to meet the internal 54.2 ° boundary of the etched silicon nitride

where a further portion of the wave energy is dissipated. Once the acoustic wave has reached the inside of the fluid cell, the wave is carried by the fluid (crystallisation solution) within the cell to the far wall where once again a portion of the wave travels into the wall and a portion is reflected. The tapered walls of the cell ensure that for a range of frequencies there is a wavelength where the distance between the walls is equal to $\frac{n\lambda}{2}$. When this condition is met, a standing wave is able to develop within the cell. If the settling force of the crystal is lower than the force of the standing wave it becomes possible to trap the crystal in position enabling diffraction. Constructing the cell from etched silicon nitride membranes gave extremely flat sealing surfaces allowing effective fluid trapping and an X-ray path which is controlled, short and uniform.

3.4 Sample Preparation

Protein crystals were prepared by in-house biologist Tracey Keates at Diamond Light Source. Commercial insulin (Bos taurus) was resuspended to a concentration of 15 mg ml^{-1} in a solution of 10 mM of EDTA and 50 mM disodium hydrogen phosphate to a pH of 10.5. The reservoir solution consisted of 25% w/w ethylene glycol. Sitting drops were made by mixing 2 μl of protein solution and 2 μl of reservoir solution. Wells were filled with 300 μl of reservoir solution and equilibrated against the siting drops in sealed trays, at 20 °C. Crystals approximately 40 μm in diameter grew during the following week.

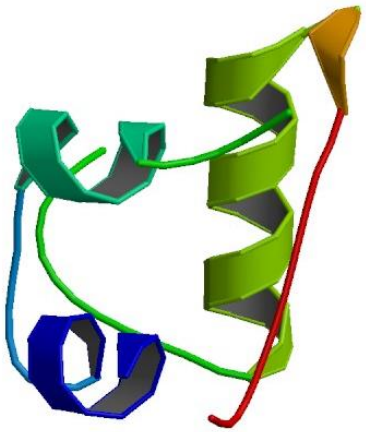

Figure 3.7 PDB ID: 4ihn, Belmonte, L., Pechkova, E., Bragazzi, N., Nicolini, C., High Resolution Insulin by Langmuir-Blodgett Modified Hanging Drop Vapour Diffusion.

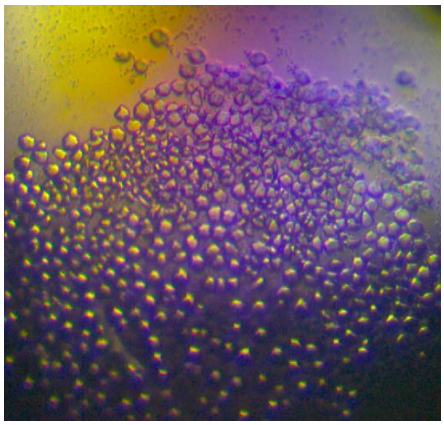

Figure 3.8 Bovine insulin crystal sample approximately 50 µm in diameter- test sample provided by Diamond Light Source

3.5 Sample Mounting

In order to present samples to the beam a novel 3D printed mounting system was developed. The design used kinematic principles to reduce the changeover time during experiments that often occurs in synchrotron-type experiments given the need for work to take place in a sealed

room and in front of a small and precisely focused X-ray beam. The sample mounting procedure is depicted in Figure 3.9, and may be summarised as follows:

i. A silicon nitride window is placed on the alignment fixture, locating pegs are used to ensure that the window is horizontal.
ii. Cyano-acrylate (Loctite 401, Farnell, UK) is sparingly applied to the mounting wand, ensuring any excess is removed.
iii. The mounting wand is located in the socket features of the window alignment tool.
iv. Gentle pressure is applied between the mounting wand and the silicon nitride window by rotating the wand in a hinge-like manner, depicted in Figure 3.9.
v. The bond is almost immediate and the wand may now have a thin layer of silicon grease applied around the edge of the window to act as a sealant.
vi. A second window is placed on the window alignment tool and approximately 5 μl of crystal laden solution is deposited into the well.
vii. As before the mounting wand is located in the window alignment tool and carefully rotated into planar contact with the second window.

It is important to note that the mounting wand is deliberately asymmetric to prevent misalignment when using it with the window alignment tool or the acoustic mount. A mounting study was conducted, and is described in Appendix 0. In summary, the study identified key parameters of angular and vertical location were repeatable. Angular repeatability for a single wand was found to have a two standard deviation (2σ) value of < 3 °, and 57 % of trialled samples achieved $2\sigma < 1.5$ °, allowing for improvements by process control. Further details and discussion are in Section 0.

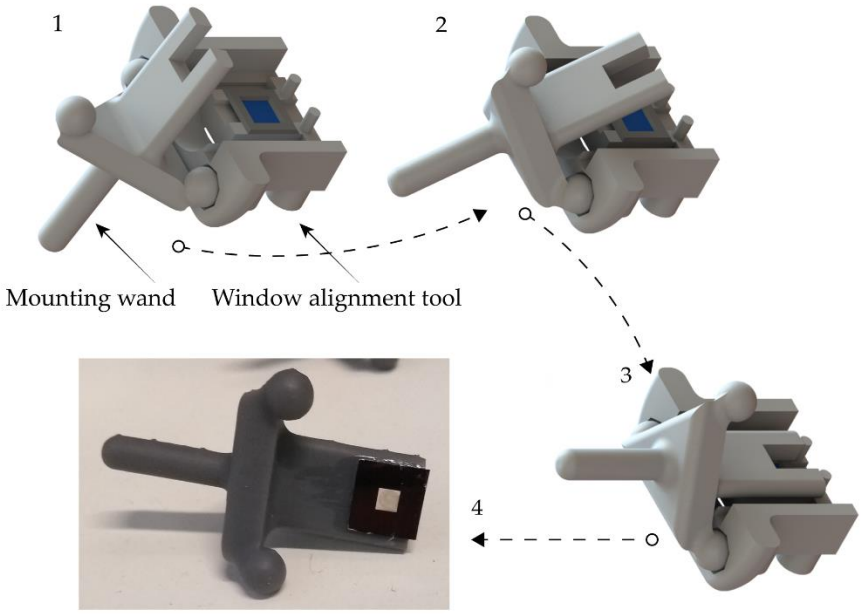

Figure 3.9 Mounting method designed to restrain and position silicon nitride on silicon frame windows.

3.6 Results and Discussion

Work was undertaken at Diamond Light Source, beamline i24, as part of Beam Access Group Session 14493-100 September 2017, the acoustic trapping was successfully trialled and diffraction and fluid cell compatibility was demonstrated.

3.6.1 Transducer operation

The transducer was driven by an RF amplifier (20B, Henry Radio, USA) with gain > x 60. The device was characterised by a Sark-115 network analyser (Seeed, CHI). Series and resistive impedance were measured, along with a voltage drop measurement taken during operation, as shown in Figure 3.10 and Figure 3.11, respectively.

In Figure 3.10, two traces are plotted, the purely resistive response of the transducer (shown in black) and the series circuit equivalent reactance (shown in blue). To recap for the non-

specialist, the reactive portion of complex impedance consumes power but does no useful work. The significant increase in the resistance in the 25 MHz region arising for the purely resistive load (black trace) is due to the mechanical losses caused by radiation from the device. The increase gives an indication of how the device performs as an excitation source at a given frequency. [112] The device can be seen to also have broad peak centring at 24.63 MHz slightly off from the zero crossing of the reactance (blue trace, 24.22 MHz).

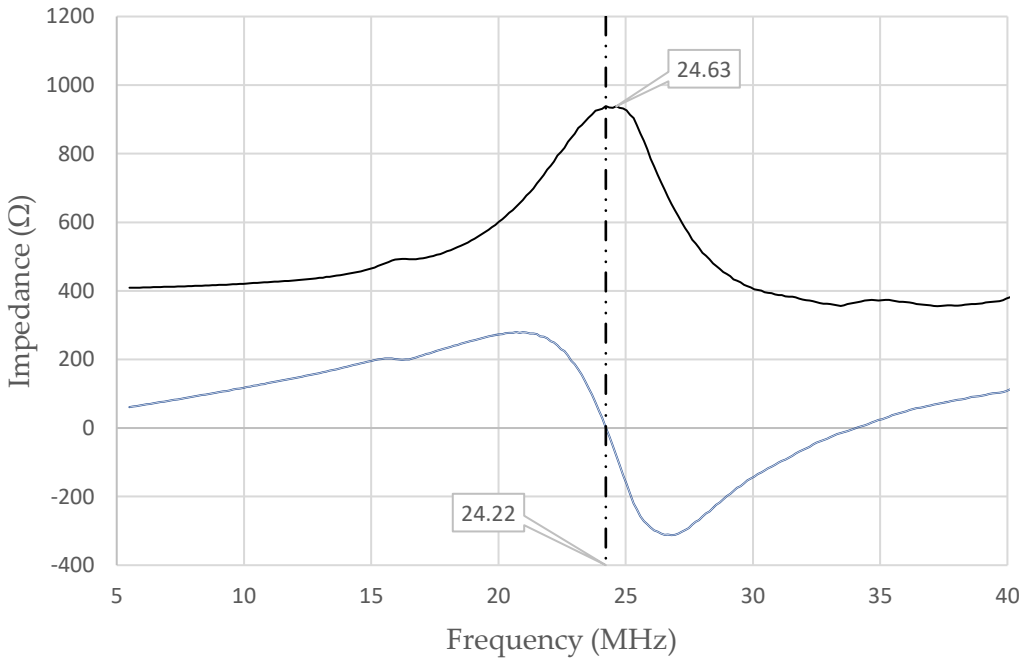

Figure 3.10 Olympus Videoscan 25 MHz transducer frequency response measured by network analysser. The complex impedance curve is shown in black, the reactance phase (serial) is shown in blue and the zero crossing is marked by a dashed line at 24.22 MHz.

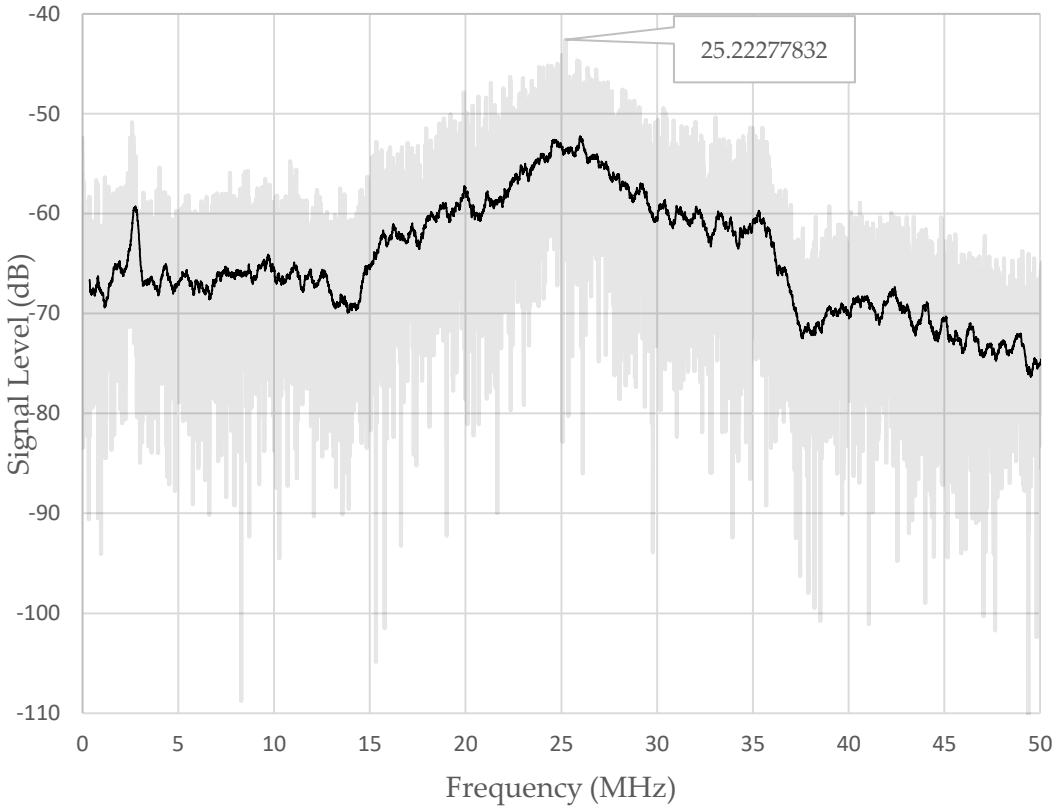

Figure 3.11 Olympus Videoscan transducer in operation. Background trace shown in grey is raw voltage drop data, the black line shows a 100 period average.

3.6.2 Background scattering performance of the standing wave trap

Within the portion of the device that contributed to scattering was formed of a silicon nitride and silicon sandwich. The beam path comprised of a 1000 nm thick silicon nitride layer chemically deposited on silicon wafer (the silicon wafer did not form part of the beam path) and the fluid volume of 6.3 µl of bovine insulin crystallisation solution having a through thickness of 525 µm. All trials were conducted using bovine insulin crystallisation solution as the acoustic medium.

Eight stills taken during the experiments were processed in accordance with Section 3.3.3, an example still is included Figure 3.12. The Pilatus 3 detectors records counts when sufficient X-ray photons reach a pixel. Each pixel performs this cycle many times a second, providing

significant information 'depth' (or, more accurately, intensity resolution). The counts are referred to as counts per second (CPS).

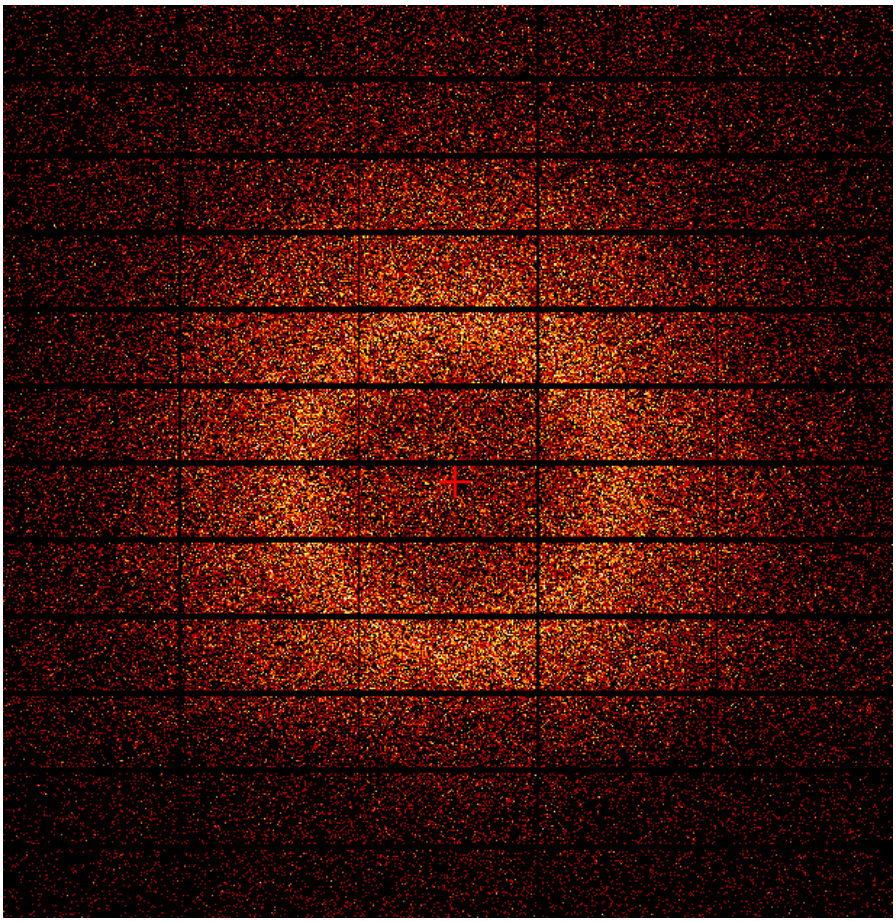

Figure 3.12 Diffraction still captured during 14493-82.

The custom-designed sample holding arrangement performed in a fashion commensurate with the state of the art. [149] Shown in Figure 3.13 (blue trace), the average background scatter across the detector was < 10 CPS. Air scattering is also plotted in Figure 3.13 for comparison (shown in black). Evaluating air scatter provides a useful benchmark as it is the minimum background scatter obtainable, without modifying the gas environment around the detector. Within the high resolution (2 Å) region fewer than 5 CPS were observed. While direct

comparison is challenging due to the availability of data, it is probable that this arrangement outperforms *in situ* crystallisation trays that are currently utilised simply through significantly reduced material in the beam pathway.

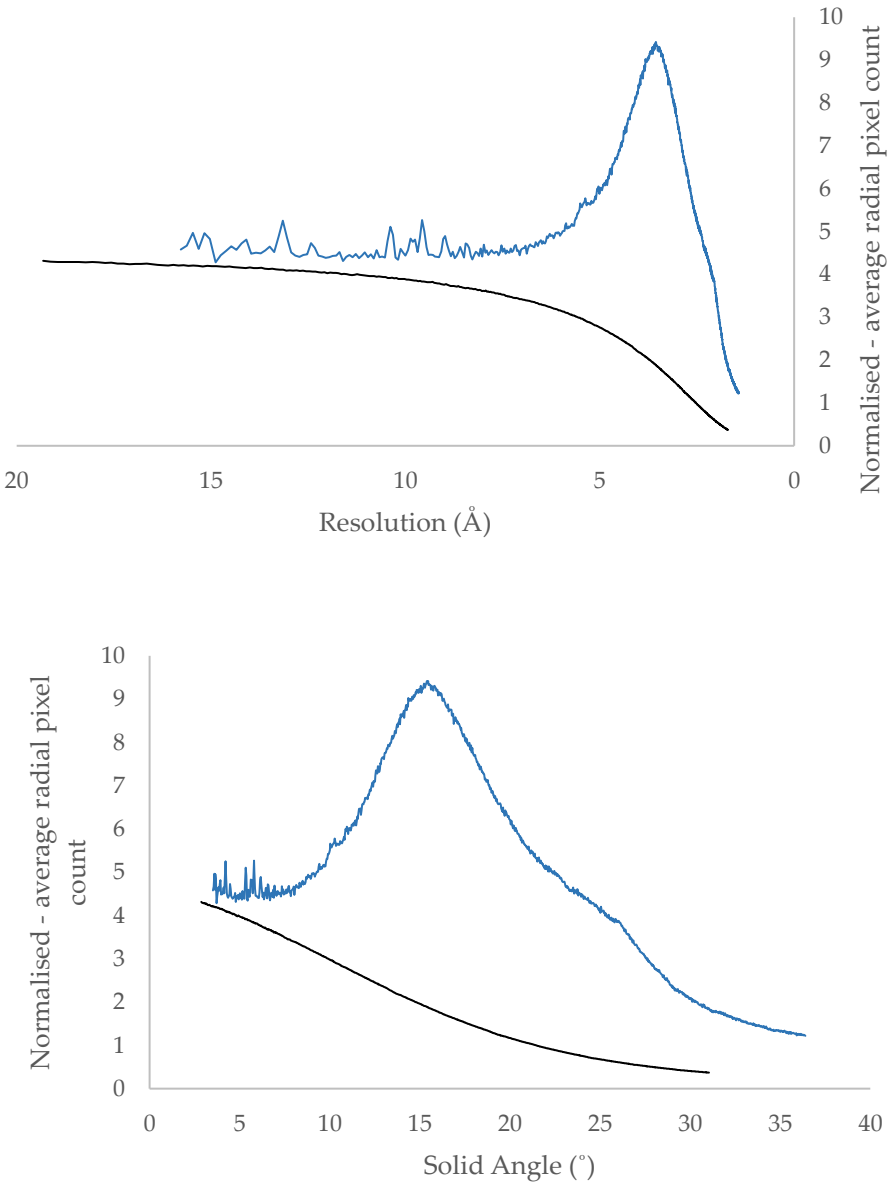

Figure 3.13 Plots showing averaged background scatter as a function of solid angle (top) and resolution (bottom), normalised background scatter (blue), and normalised air scatter (black).

It is evidently impractical, however, to construct lab-ware from 1000 nm thick silicon nitride. Two areas may be considered to improve the background scatter, the first being thinner silicon nitride, and secondly, a reduced fluid volume. It is entirely practical to reduce the membrane thickness to 500 nm. The fluid volume is more challenging, as it is only possible to buy 525, 381, 200, 100 μm thickness frames, and customisation is a lengthy procedure. A 381 μm arrangement may be plausible, however, as fluid cells reduce in volume, there is a marked increase in user difficulty, stemming from small volume fluid handling and crystal sizing prior to the experiment.

Figure 3.14 shows a section of a diffraction still taken during nt14493-82, with clear Bragg spots in evidence against a low-noise background scatter.

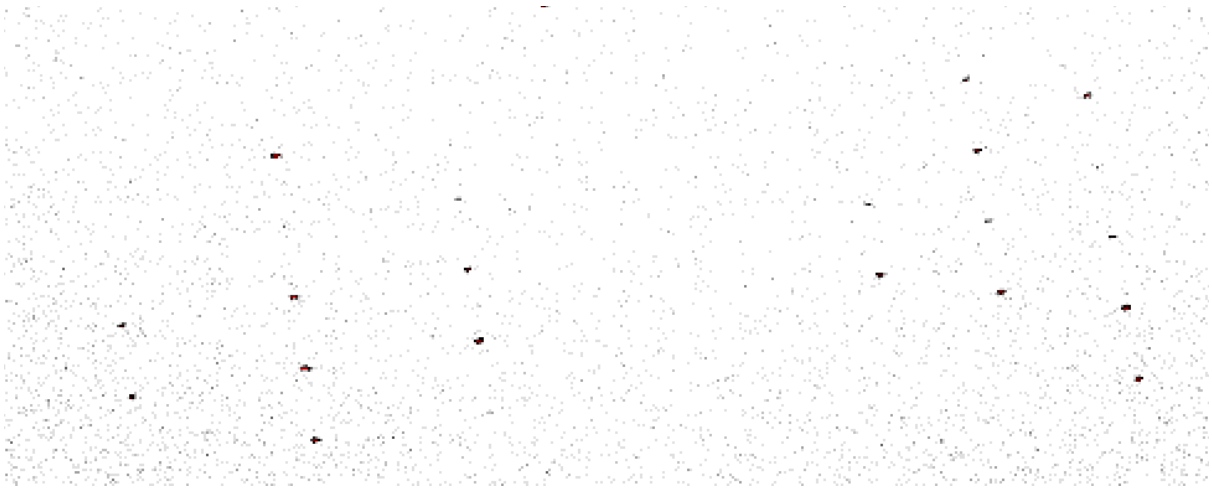

Figure 3.14 Section of a diffraction still taken during beam time nt14493-82, showing diffraction spots in comparison to background scatter.

3.7 Crystal Motion

During experiments, crystal motion was observed to be affected by the applied acoustic radiation. The diversity of crystal size, shape and starting position gave rise to several responses. Types of crystal motion observed during the experiment include:

- Switchable-slowing of crystal sedimentation,
- Crystal trapping,
- Upwards translation.

In a vertical trapping arrangement, crystal motion is dominated by gravity and sedimentation. A crystal will very quickly reach terminal velocity (taking less than 1 s) when no acoustic force is applied, a velocity which is dependent on the working fluid, and the distance from the wall of the fluid cell and other crystals as discussed in Section 1.7.1. Figure 3.15 (top) shows the trajectory of a crystal held in an acoustic field (period t: 0 – 7 s). In the later time period the trapped crystal almost immediately reaches terminal settling velocity after the transducer is switched off (period t: 8 – 11 s). A sharp response to the presence of the acoustic field can be seen, with the crystal rising to the trapped position. A rising motion demonstrates that a careful balance of forces must be preserved between a primary force (quartz wind), a secondary force (standing wave trapping), the acoustic streaming effect and the sedimentation effects caused by gravity, to achieve a steady state position.

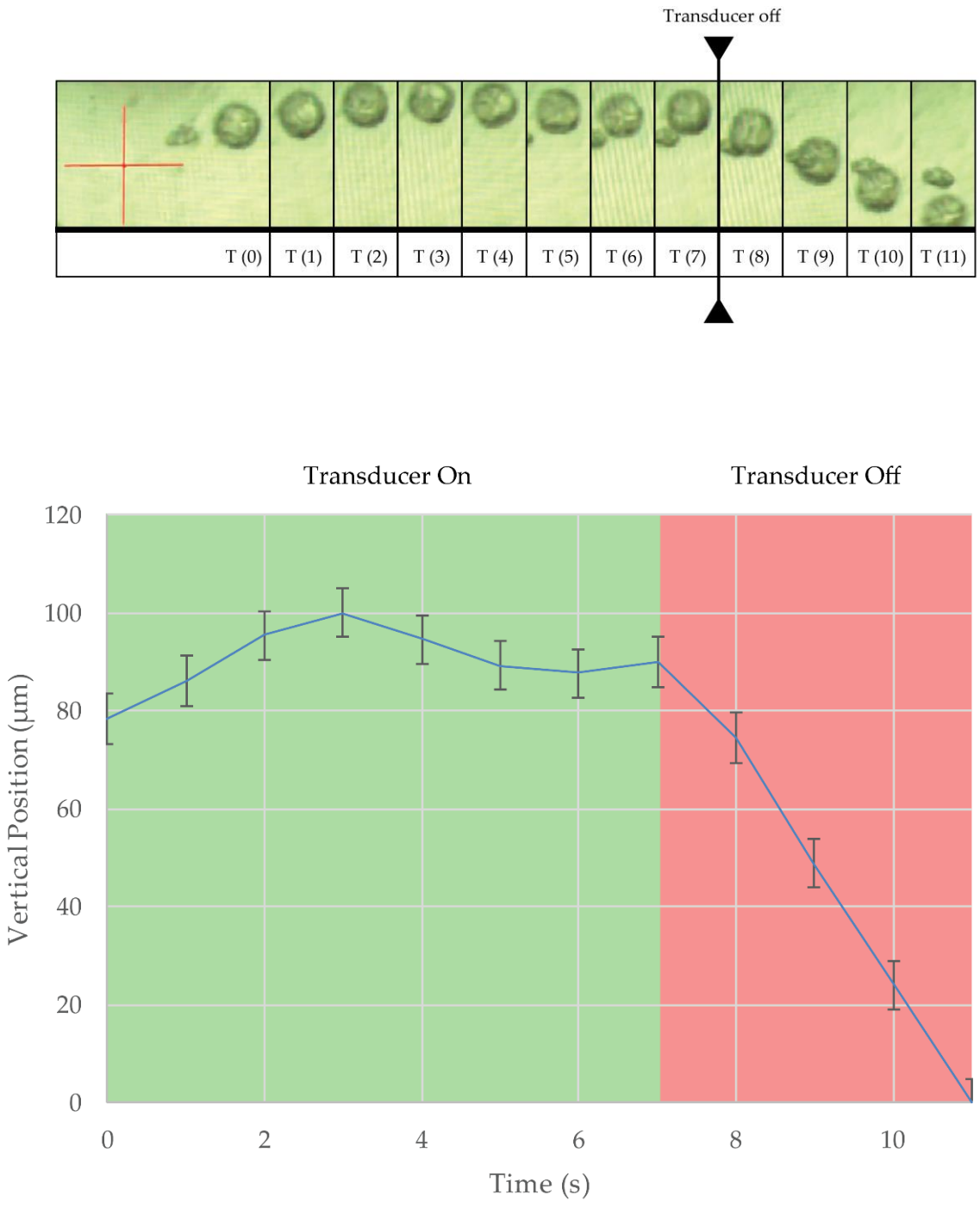

Figure 3.15 Sections from captured frames showing a trapped insulin crystal rising to stable a trapping position (top) and a line graph describing the motion (bottom).

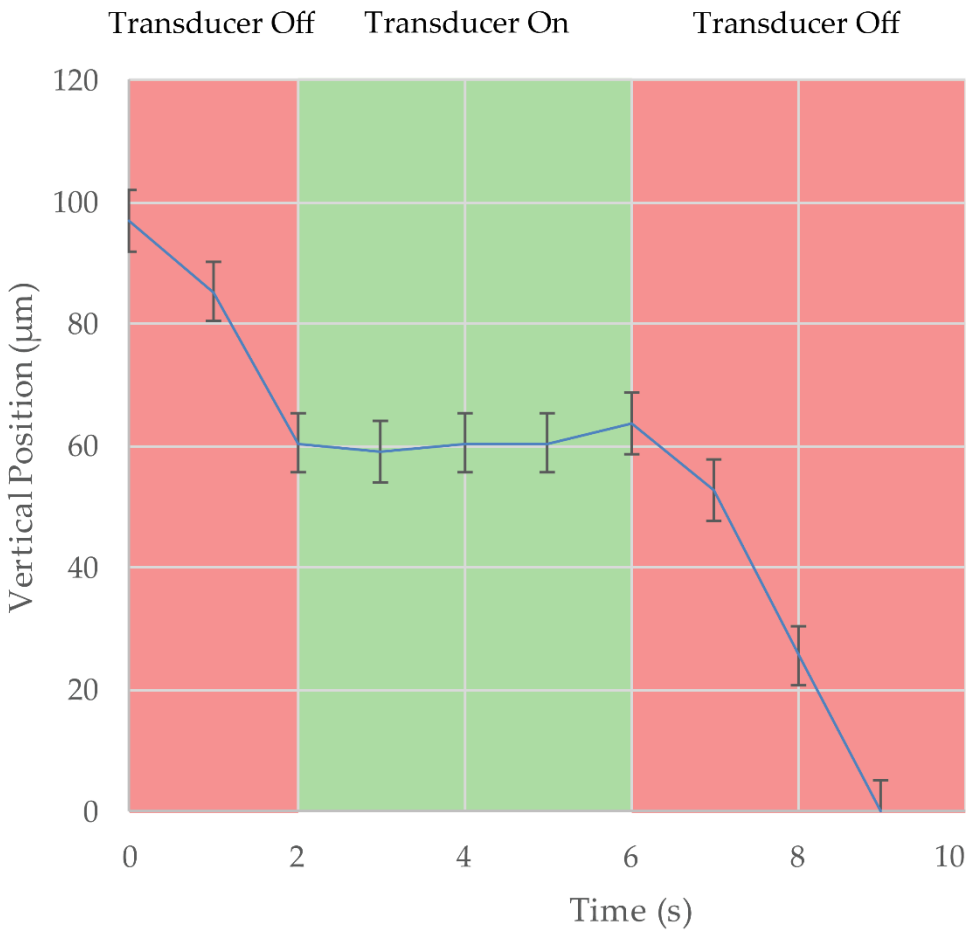

Figure 3.16 Crystal falls to a stable trapping position.

Figure 3.17 shows the course of an insulin crystal where the balance was not met. After an initial fall that was arrested by the acoustic field, the crystal accelerates upwards being trapped at two separate nodes: height 20 µm and t: 7 – 9 s; height 60 µm t: 12 – 16 s. The distance between nodes is comparable to the equivalent wavelength in pure water where $\lambda / 2 > 30$ µm. At the time of writing data was not available on the speed of sound in common crystallisation solutions, nor was the viscosity data making wavelength calculations challenging, however, assuming a standing wave at 25 MHz, the wavelength corresponds to a speed of sound of 2000 ms^{-1} which is a realistic estimate for crystallisation fluid.

A further trial with a drop containing a higher number of insulin crystals were diffracted. Shown in Figure 3.18 are approximately 18 crystals. Crystals were effectively trapped for sufficient time to allow safe exit of the experimenter from the X-ray enclosure, targeting and diffraction. A grid has been placed over the images, taken from video at 1 s intervals, and assembled to give context to the motion observed. Overall, the crystals were seen to experience minor translation while 'trapped', despite the vertical orientation. Crystal-to-crystal coupling (flocculation) did occur but did not immediately cause the pair or group to descend.

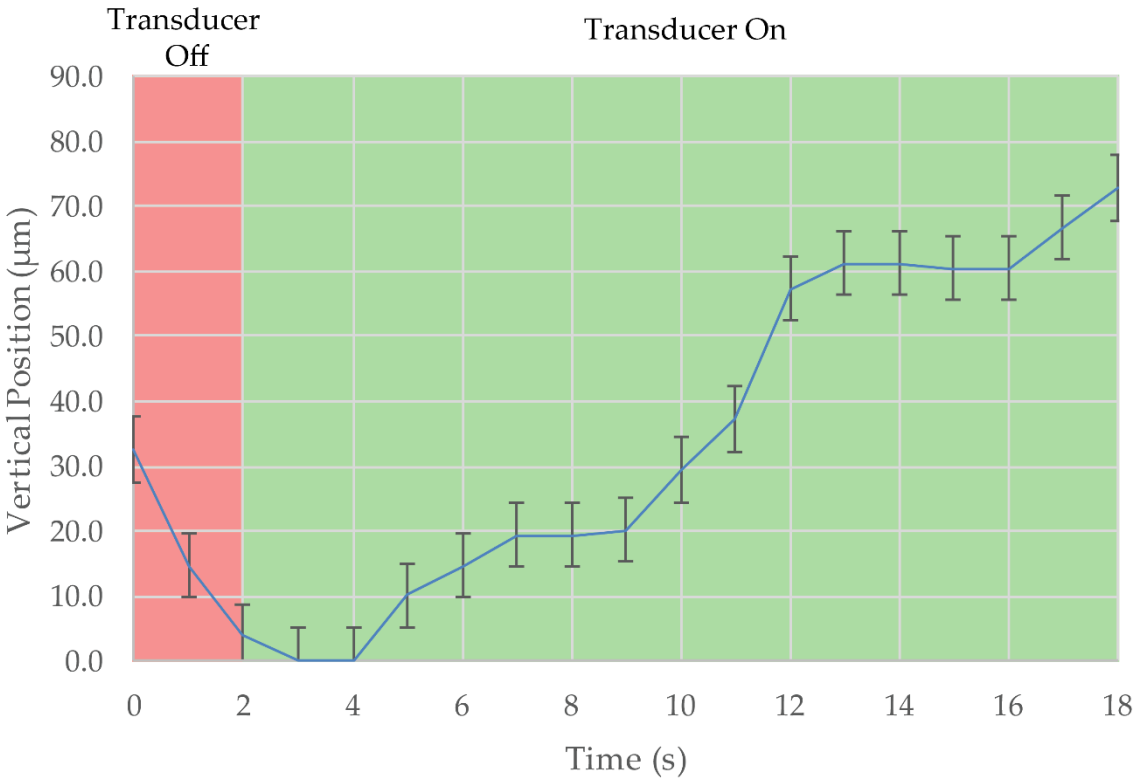

Figure 3.17 Line plot showing crystal motion when the forces did not balance, where crystal descent is arrested and the crystal proceeds upwards through two trapping nodes.

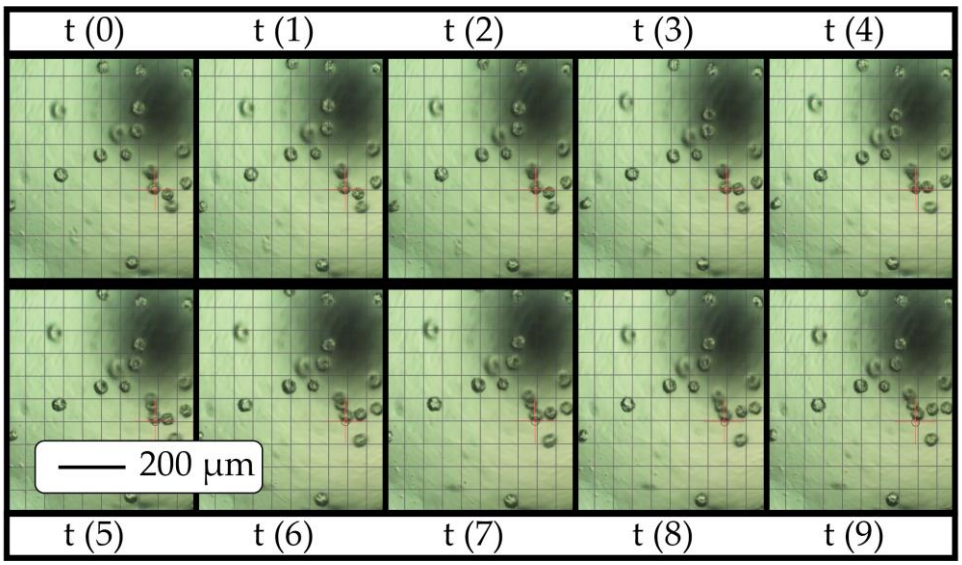

Figure 3.18 Multiple crystals held in vertical position during beam-time, with sufficient stability to enable targeting.

3.8 Hit rate

DISTL plots, produced by IsPyB (DISTL: Diffraction Image Screening Tool and Library IsPyB: Information System for Protein Crystallography Beamlines, a multi-facility experiment management tool [150], [151]), showing the diffraction data collection rate for crystals held in standing waves during experiments, are shown in Figure 3.19. Each plot represents a single experiment. During all experiments, the detector (Pilatus 3M) was run at a frame capture rate of 100 Hz, giving an experimental duration of 50 s. During the experiment, targeting of trapped crystals was achieved manually, and with delayed X-ray feedback. While manual targeting is perfectly adequate for proof-of-concept trials, automation of stage motion would be a worthwhile investigation.

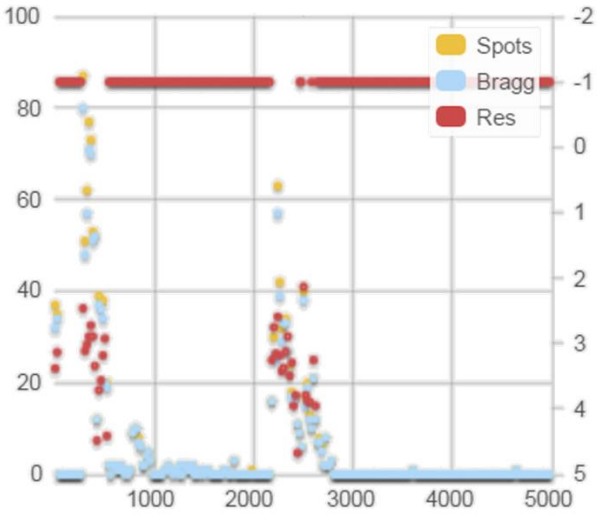

A)

Sample Ins01

Run: Data01

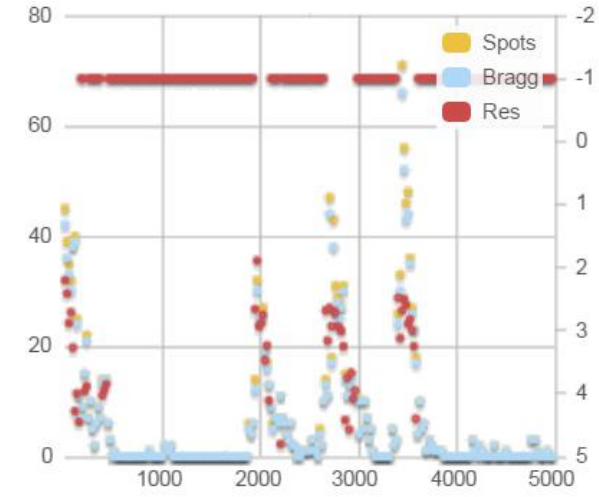

B)

Sample: Ins02

Run: Data01

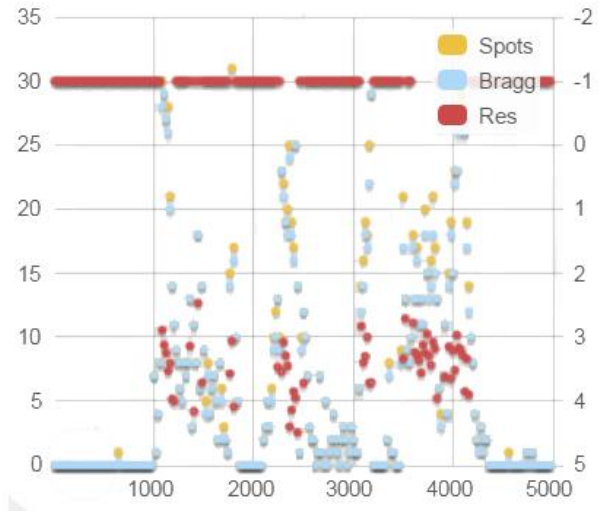

C)

Sample: Ins02

Run: Data02

Figure 3.19 Diffraction acquisition data for vertically acoustically trapped bovine-insulin crystals, DISTL plots created during two diffraction experiments, each lasting 50 s where Yellow is the spot count, blue is the Bragg candidate count and Red is the resolution of the count shown on the right hand axis (e.g. closest to zero is the

highest resolution) A) A scatter plot showing discrete hit events, B) A scatter plot showing a higher frequency of discrete hits. C) A scatter plot showing approximately continuous data capture.

In the generated DISTL plots: Left axis represents total spots with an intensity greater than the cut-off ($I(X) > \gamma_l$ {typically tested at 1.5, 2, and 2.5}, yellow), and Bragg candidate spots ($I(X) > \gamma_u$ {typically 3.8}, blue), where I(X) is calculated as shown in Equation(3.7). The right hand axis of the DISTL plot represents the resolution ring the spots were present in (red). Where the resolution count reads -1, the resolution is > 5 Å.

$$I(X) = \frac{X - m_{n\times n}}{S_{n\times n}} \tag{3.7}$$

Where $I(X)$ is the pixel signal height, X is the digitized pixel value, $m_{n\times n}$ is the average of the n sized square window around the pixel, and $S_{n\times n}$ is the standard deviation of the same window.

Unfortunately, as can be seen from the resolution typically remaining around 3 Å, crystal quality was insufficient to allow the accumulation of data. The careful material selection and assessment of the background scatter of the cell in Section 3.6.2 suggests that data were not lost due to attenuation below the background scatter level.

Positions A and B, in Figure 3.19, show regions where crystals were manually targeted, with clear targeting 'hit' events. Figure 3.19 Position C was recorded with a higher number of crystals present in the targeted region, where clustering meant individual crystal 'hits' were less distinguishable. However, it is possible for any overlapping crystal data to be deconvolved at a later stage, so multiple hits may be considered innocuous.

3.9 Conclusions and further work

The virtual trap method designed and developed in this work shows strong experimental evidence for the ability to efficiently trap and diffract protein crystals at room temperature and *in situ* without the need for involved and time consuming single crystal mounting procedures. The diffraction data acquired from the study was limited by sample quality. However, background scattering measurements indicate that high quality data acquisition is possible with the current arrangement. The level of stability shown in trapped crystals is highly applicable to the problem of crystal mounting, and observed acoustically-induced crystal rotation removes the need for goniometer collection strategies, suggesting that the technique may form a 'complete' mounting method. The translation speed (and by inspection the rotation speed) appear appropriate to the detector frame exposure time of 10 ms. Crystal 'hit' rates appeared to decline after initial targeting, therefore further study is needed to determine if this is due to crystal degeneration attributable to radiation damage, or the beam locally affecting the crystal trap (radiation damage at room temperature should be anticipated). The sealed environment succeeded in creating a long sample life, with multiple collection runs possible with a single cell, no evaporation was evident. Going forwards, incorporation into a microfluidic environment would be of significant interest, allowing the introduction of new crystals for investigation without the need for users to enter the experimental chamber. Secondly, the additional automation of targeting tasks would likely allow for a practically continuous data collection. In summary, acoustic trapping has been demonstrated *in situ* as a technique with significant potential for room temperature protein crystallography. The ease of target acquisition for

unmounted samples is a clear advance towards automating sample handling in a room-temperature, fluidic and non-contact manner, and further investigation into the mounting of irregular and non-spherical crystals is a promising next step.

4 Development of the on-chip goniometer

4.1 Chapter Summary

In this section operational parameters are developed and discussed which were used in the design of the on-chip goniometer. Amplifier linearity, droplet acoustic absorption, droplet vibrational modes and vortex modes were considered in light of input frequency and working fluids. The results suggested that the On-chip goniometer would be suited for use with the full range of crystallography fluids at the selected driving frequency.

4.2 Introduction to the on-chip goniometer concept

To reconstruct a 3D lattice via diffraction, diffraction images taken throughout rotation of the lattice is required. This is traditionally achieved through the use of planned rotation of a goniometer. The advent of serial crystallography data processing techniques which allow for diffraction patterns with unknown rotation of the crystal lattice to be reconstructed into a crystal structure gives the opportunity to test acoustic field actuation of drops on a simple surface. This may be simply described as a single drop containing a crystal or multiple crystals on a piezo electric device. The benefit arising from this is that a droplet based mounting technique would be readily automated via droplet ejection techniques. The following chapter describes the development considerations and operating goals for an on-chip goniometer, which was then realised and tested in Chapter 5.

4.3 Theoretical considerations for an on-chip goniometer

4.3.1 Crystal settling rate

As described in Section 2.4, the ability to target a crystal requires stability of position. The vertical component of which is dominated by the settling velocity for low fluid velocity. The settling rate for a given crystal is given by Stokes law, which is reproduced in equation (4.1)

$$V_t = \frac{g d^2 (\rho_{p-} \rho_m)}{18\mu} \tag{4.1}$$

Where V_t is the terminal velocity, g is gravity, d is the crystal diameter, ρ is the crystal density and the fluid density respectively and μ is the viscosity of the fluid.

Restating the previously discussed result, for crystals suspended within a fluid between 50 and 200 μm a crystal would have traversed the entire height of a proposed droplet within a

timespan consistently less than two seconds. equation (4.1) is plotted in to illustrate the ability of the device to use the horizontal surface of the transducer as a locating feature for crystal targeting.

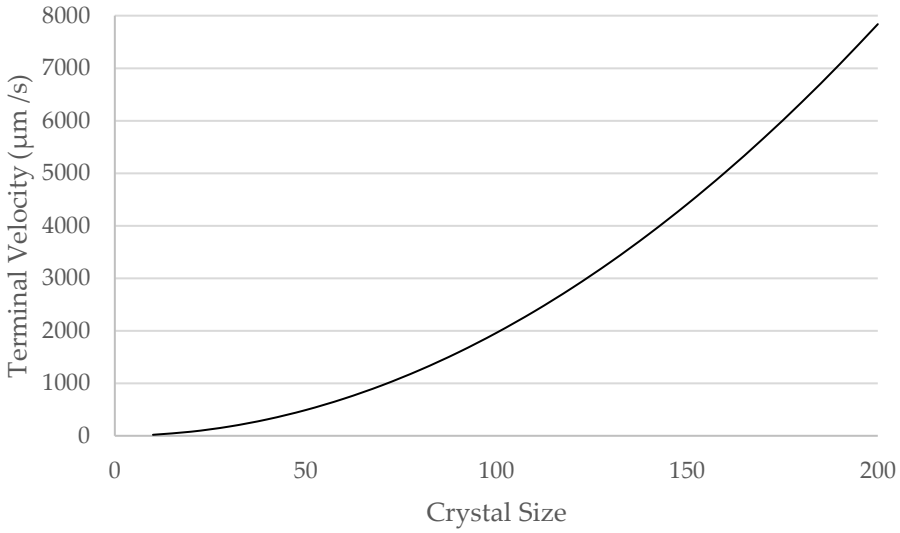

Figure 4.1 Settling velocity for a crystal

The settling velocity result is important for evaluating the translation and rotation requirements for the goniometer.

4.3.2 Speed of translation

The limiting factor for the crystal translation is the ability for the user to target the crystal with X-rays and the quality of data which will be produced. Translation of the crystal does not affect data beyond targeting as rotationally invariant translation does not alter the lattice orientation and so the pattern produced at the detector remains constant.

However, restating the previous result, for a beam of approximately 10 μm width, a detector capable of 100 Hz capture, and a crystal of 100 μm length Figure 4.2 depicts the number of images produced assuming the translation is consistent.

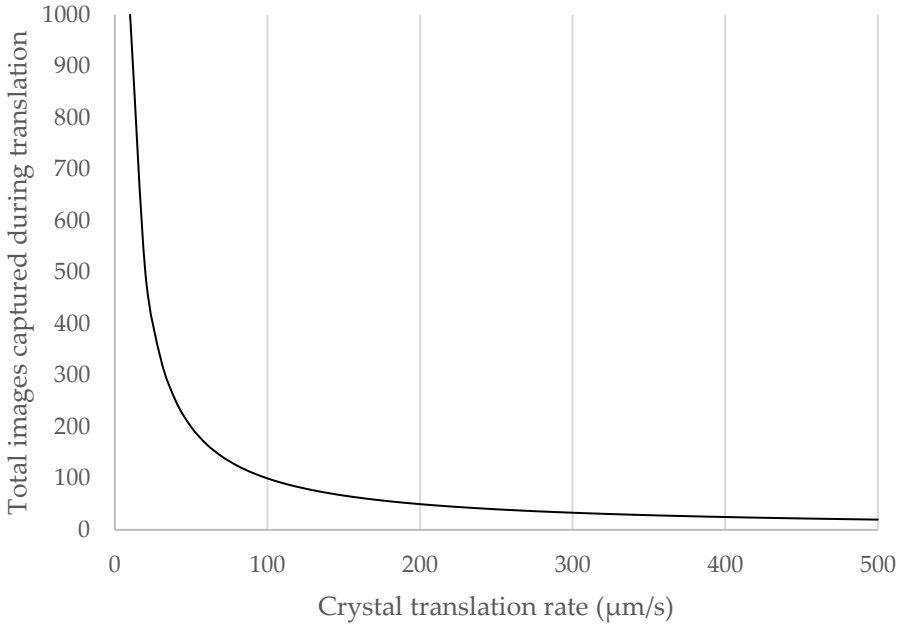

Figure 4.2 Crystal images produced during a single consistent translation.

The result, as before, shows that translation of a crystal should be largely minimised as even small crystal velocities would require that the beam be retargeted.

4.3.3 Absorption of a surface wave by a drop

Attenuation due to radiative power loss, as energy transfers from the surface wave to the fluid

Attenuation or radiative loss of a wave travelling along a surface fluid interface may be described by equations (4.4)-(4.5). The equation is formed of an exponential decay and the acoustic impedance for the fluid and the substrate. [152] Comparing water and lithium niobate evaluates to: $\approx \frac{0.09}{\lambda}$. It is apparent that as the wavelength decreases towards zero (indicating that the frequency is rising) the attenuation of the wave by the fluid occurs in a shorter distance. Given a design wavelength of 160 μm (or 160×10^{-6} m at 24 MHz) equation (4.3) evaluates to an attenuation coefficient of $\alpha_L = 568.4$. Equation (4.2) is then evaluated for a

range of wavelengths and plotted in Figure 4.3, showing that after 10 wavelengths over 50 % of the incident power is transferred to the fluid.

$$Q_x = e^{-\alpha_L x} \tag{4.2}$$

$$\alpha_L = \frac{\rho_F C_F}{\rho_R C_R \lambda_R} (m^{-1}) \tag{4.3}$$

Where Q_x is the ratio of energy lost (m^{-1}), x is the distance which a wave has travelled along the solid-fluid interface (m^{-1}), α_L is the attenuation coefficient, ρ_F is the density of the fluid, C_F is the speed of sound of the fluid, ρ_R is the density of the substrate, C_R is the speed of sound of the substrate and λ_R is the wavelength (m^{-1}).

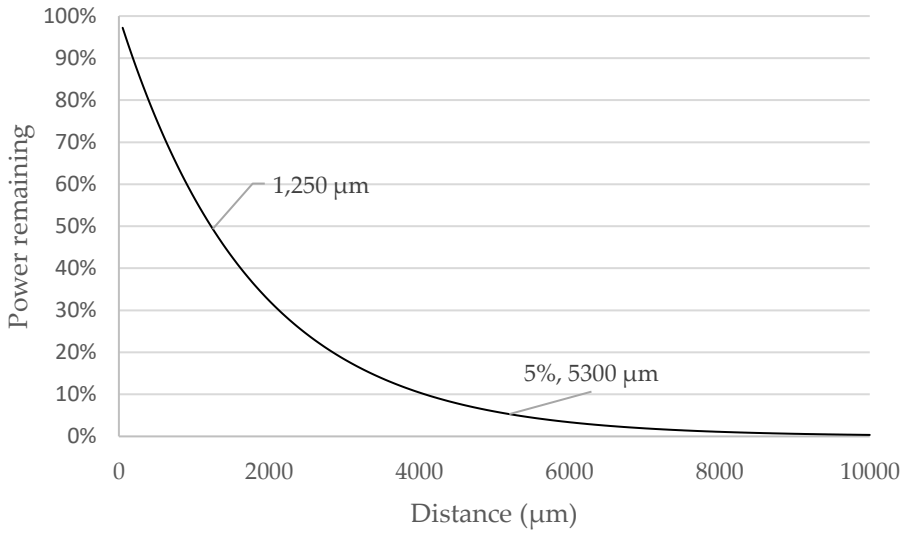

Figure 4.3 Attenuation of a 24 MHz Rayleigh wave by a surface water layer.

4.3.4 Acoustic resonance of a sessile drop

The resonance of a sessile drop was calculated to ensure that it was possible to reliably excite vortex motion within a droplet. The works of Vukasinovic et al, and separately Noblin et al

was used for calculations as shown in equation (4.4) and (4.5) and Figure 4.4 is included for clarity: [153], [154]

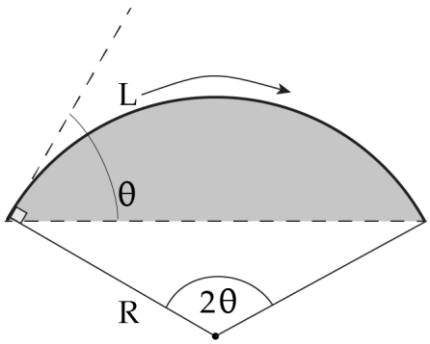

Figure 4.4 Diagram showing the relationship between contact angle and profile length (L), where R is the radius of the spherical cap, and Q is the contact angle, the droplet area is shown in grey.

$$f^2 = \frac{n^3 \pi \gamma}{4\rho L^3} \alpha^2 \tag{4.4}$$

$$\alpha = \frac{n\pi d}{L} \tag{4.5}$$

Where f is the frequency of surface oscillations, n is the wave number, ρ is the fluid density, γ is the surface tension of the liquid, and L is the length of an arc describing the drop surface.

This is an approximated method adapted from the depth of a fluid filled bath (d), as such α may be approximated by the following:

$$\alpha^2 = \tanh\left(\frac{n\pi\overline{h}}{L}\right) \tag{4.6}$$

Where $\overline{h}$ is the average height of the sessile drop.

Using Equation (4.4) the range of mode numbers (n = 0 : 5000) shown in Figure 4.5 *Plot showing the full range of resonant modes of a sessile drop up to n = 5000.* were determined for pure water (a linear fit is included to help make the roundness of the curve more obvious). A further assumption was included as the element α was approximated to 0.89 in accordance with work done by Sharp et al.[155] An interesting point of note is that although the droplets are of millimetre scale, the first resonance has an equivalent longitudinal wavelength of 0.14 m, a result that is in good agreement with literature. In Figure 4.6 the curve demonstrates the range of mode numbers with similar wavelengths (+/- 5 μm) to the selected excitation frequency (24 MHz gives $\lambda \approx 57$ μm).

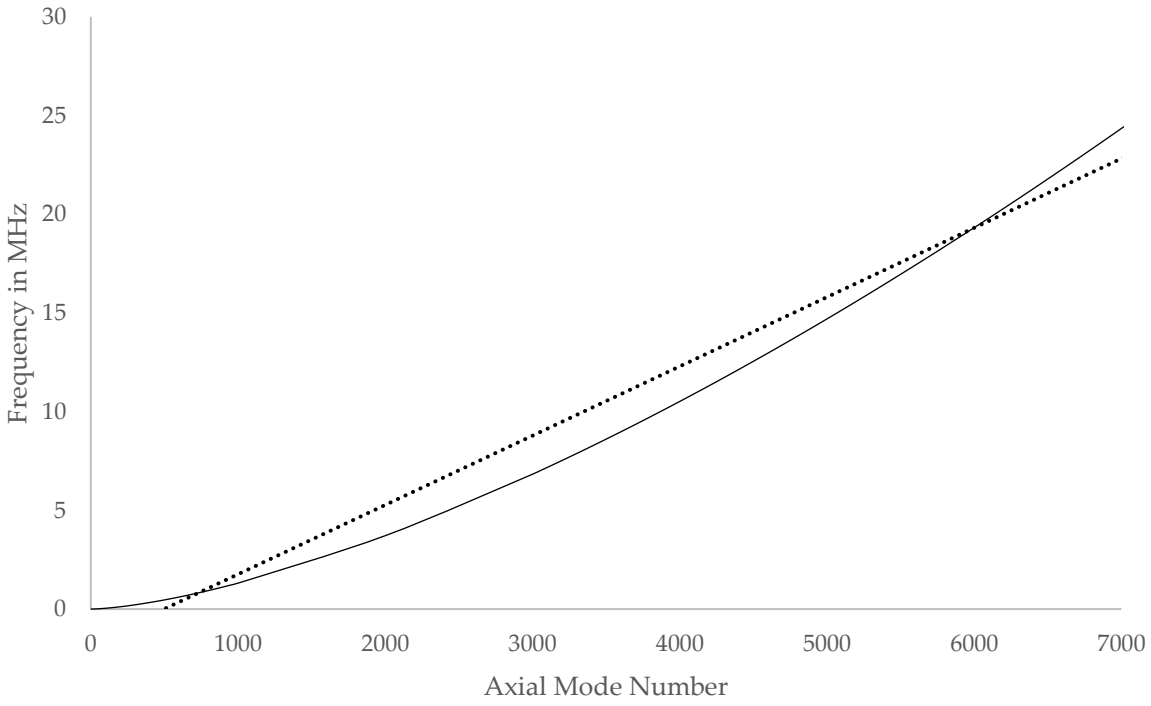

Figure 4.5 Plot showing the full range of resonant modes of a sessile drop up to n = 5000.

4.3.5 Acoustic vortex mode

Surface acoustic waves have been shown to produce distinct internal flows dependent on the size, voltage and symmetry of the sessile drop and transducer arrangement. Voltage and drop

size have been shown to affect the speed, offering a method to modulate the rate of crystal presentation which was relied upon in Section 5.[156], [157] Rotational modes occur within a sessile drop in respond to the refraction of an acoustic wave into the fluid from the underlying boundary. The type of rotation generated may be selected by positioning the drop relative to the transducer, or through the addition of a secondary transducer.[104] The resultant flow patterns are provided in Figure 4.6. The rotational (acoustic streaming) component of the flow is what recommended this technique for use as within an on-chip goniometer device, since rotation of the crystal lattice is required for a complete dataset.

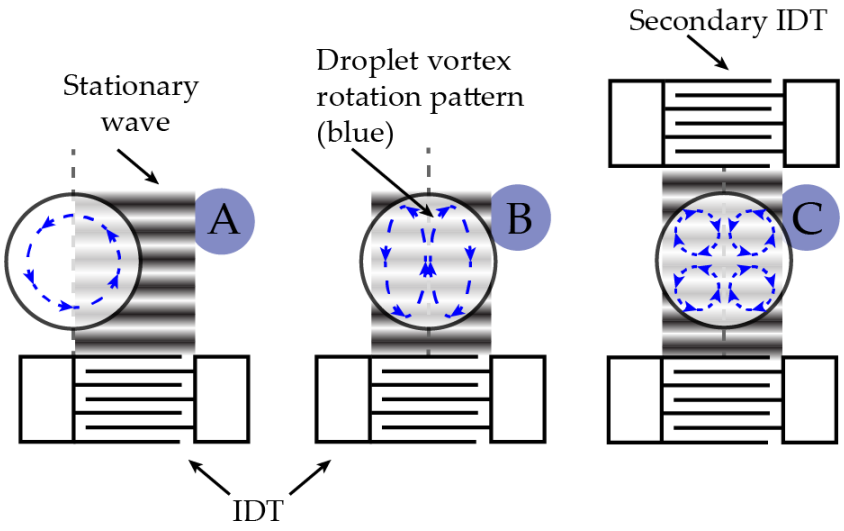

Figure 4.6 Rotational modes within a surface-wave-excited droplet.

4.3.6 Amplifier output

The amplifier 20B (Henry Radio, USA) was attached to a 60 MΩ ceramic ballast resistor load. A Rigol DG4102 (Rigol, CHI) signal generator, was used to create an electric signal composed of 25 MHz sine waves of various amplitudes. The resulting output voltage was measured

using a Picoscope 2000 oscilloscope (Picotech USA) the True RMS / DC RMS of the signal to give a post amplification voltage. The amplifier was evaluated into and beyond the range used for the operation of the surface acoustic wave device as shown in Figure 4.7.

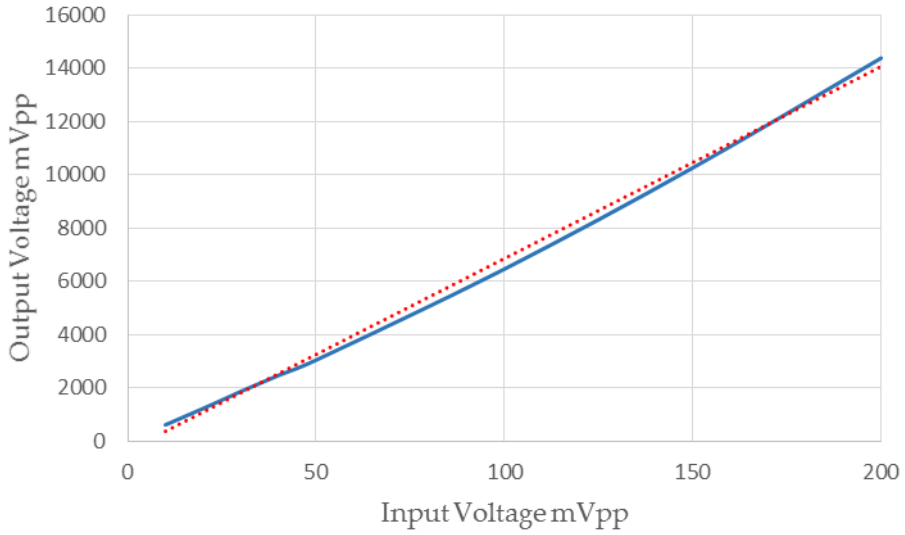

Figure 4.7 Amplifier linearity - input vs output, the red dotted line shows a linear fit of the results and the blue is the measured data.

The results of the test gave a linear gain approximation of 6410 % (× 64) across the test range, although non-linearity was apparent, the approximation gave a tolerance of +/- 12 %. In calculating the current and power being supplied to acoustic devices it was possible to refer to the specific gain as tested, which had a range of 17.89 – 18.57 dB.

4.4 Device Targets

Device targets provide a useful range of criteria against which the success or need for development of the demonstrated device can be assessed. For the on-chip-goniometer the following criteria were identified.

- To produce sufficient rotation to enable the collection of a complete dataset.
- To avoid excessive application of heat to the crystal sample
- To allow user control of the rate of rotation
- To avoid excessive crystal translation, allowing the effective collection of data
- To generate minimal background scatter during diffraction
- To generate sufficient acoustic force to excite a vortex within a drop.
- The presence of sufficient vortex force to produce rotation of the target crystal.
- The retention of crystals within a stable trapping position for a duration allowing their targeting and diffraction.
- A stable form of trapped-crystal motion allowing effective beam targeting.
- To allow scattering data to escape enabling < 2 Å data collection.
- Developed arrangement must be inert relative to the crystallisation fluid and the crystals themselves.

5 A Surface Acoustic Wave Vortex: The On-Chip Goniometer

5.1 Chapter Summary

The following chapter describes the use of surface acoustic wave vortexing to create an on-chip goniometer.[158] The chapter details the specification, design, fabrication and testing of the device. As part of the development cycle of the successful prototype device, specific challenges in physical technology and method of operation were identified. Important design choices and obstacles encountered are discussed in greater detail than in previously published work. Topics included: investigations into acoustic transducer design, thermal performance, crystal response to acoustic vortex, data quality and type, and humidity / contact angle issues. Further, observations are made on the integration and operation of the device on the beamline.

5.2 Introduction for the study

Lab-on-a-chip technology provides significant advantage in handling micro-particle suspensions. High throughput sorting, chemical treatment and analysis become possible because of dramatic system simplification. Advances in detector technology and X-ray optics means synchrotron-based macromolecular crystallography (MX) can now take advantage of new methodologies such as lab-on-a-chip. MX has an experimental pipeline that relies on the coordination of many complex, precision processes both human and mechanical. MX laboratory processes typically culminate with a single crystal isolated by hand onto a standard loop, representing considerable researcher effort. In recent years a diverse set of techniques have been developed for increased throughput in MX crystal handling, including: hydrodynamic traps, high density grid mounting, graphene microfluidics and acoustic levitation to name but a few.[21], [51], [66], [159]–[161] In order to determine the structure of a macromolecule by X-ray crystallography a complete set of the specifically oriented scattered X-rays (reflections) needs to be captured by a two-dimensional detector. Traditionally this is achieved by orienting and rotating the sample with a mechanical goniometer. However serial methods, pioneered at X-ray Free Electron Laser (XFEL) sources, rely instead on collecting a single detector image from a large number (1000s) of randomly oriented crystals.[124] As such XFEL sample presentation methods are typically much more dynamic, and include injectors that encompass gas virtual dynamic nozzles, lipidic cubic phase (LCP) extruders, acoustic droplet ejection (ADE), or concentric-flow electrokinetic injectors.[162]–[165] Alternatively, fixed target sample delivery methods include ADE coupled with a conveyor belt and various types of fixed targets wherein stationary samples are brought rapidly to the interaction region.[63], [164] All of these room temperature methods avoid structural artefacts that may

be induced on cryogenic cooling and in certain cases samples, such as viruses, can suffer significant degradation in crystal quality when cryo-cooled.[126],[129]

Our approach utilises a surface acoustic wave transducer to generate chaotic rotation of crystals within a fluid environment during X-ray diffraction. The approach occupies a uniquely small footprint and is able to maximise the amount of data from individual crystals, particularly with respect to serial methods, reducing the amount of sample required for structure elucidation.[162] Device specification was driven by the need for room temperature operation, ensuring the opportunity to resolve dynamic protein elements. Further, as there is no need to mount the crystal, nor remove it from precipitation solution, the induced rotation resolves a key challenge, namely >90° crystal rotation in microfluidic and crystallisation tray-based diffraction. As such the method is able to maximise the amount of data from individual crystals particularly with respect to serial methods, reducing the amount of sample required for structure elucidation.

The following work describes the hand mounting of a single drop containing traditionally sized protein crystals (>100 μm) onto a surface acoustic wave device. A prototype device is used to actuate the crystals, one of which is trapped and imaged at the centre of a 'low speed vortex'. Successful diffraction of a crystal under acoustic excitation is demonstrated, along with the potential of vortex entrapment for high throughput microfluidic crystallography techniques and successful data processing for structure determination despite the limitations of existing methods made apparent.

5.3 Methodology

The standing surface acoustic wave (SSAW) actuation system comprises a 3D printed kinematic 'chip' and a fixed mount, a piezo electric wafer section and a patterned hydrophobic layer for fluid deposition. Generation of a surface wave was achieved through patterned titanium and gold interdigitated electrodes (IDT) excited by a pulsed sine wave of 24 MHz and 50% duty cycle which was further cycled on and off at 1 Hz. To form the IDT, titanium was sputter coated to form a compatible and conductive base layer on the surface of the lithium niobate. This was then coated with gold to form an electrically conductive layer. A photolithographic 'lift off' process produced a periodic structure of an IDT on the surface of 128° rotated y cut, x propagating lithium niobate ($LiNbO_3$).

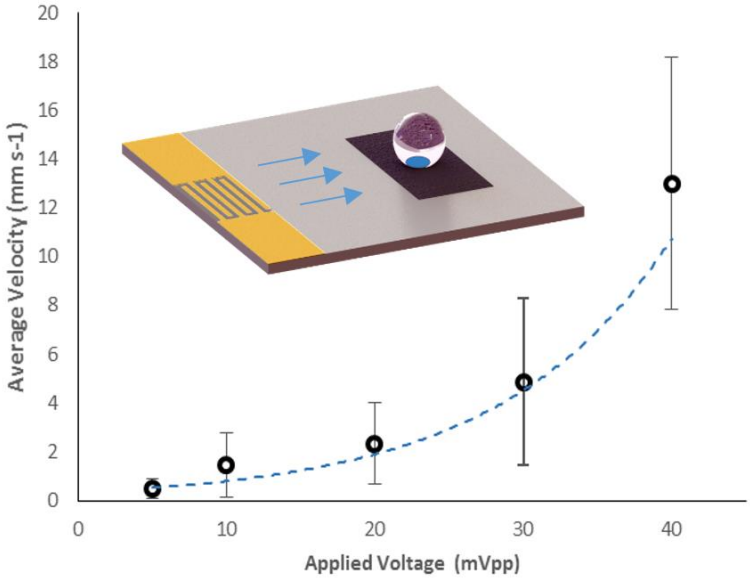

Figure 5.1 Velocity of the crystals in solution once the SSAW wave is applied. Error bars indicate standard deviation of measurements, and voltage level is shown pre amplification, where amplification is approximately linear x 64. Voltage level and mean velocity were correlated approximately exponentially, this trend is indicated

by the dashed line. Measurements were taken using digital image correlation using telecentric imaging apparatus. Overlay shows illustrative view of an IDT, with the arrow showing direction of propagation for the SSAW wave. The hydrophobic locating pattern is shown in black and the hydrophilic locating spot shown in blue beneath the fluid drop.

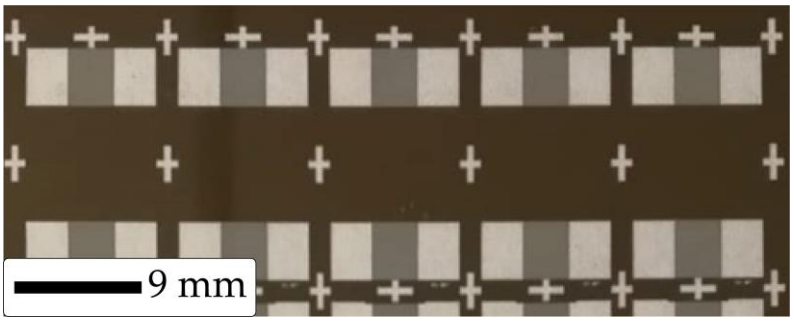

Figure 5.2 Chrome on quartz IDT photomask

For the photolithographic patterning, S1813 (Microposit, Dow) was used, along with a chrome mask from (JD Photo Data, UK) as shown in Figure 5.2. The transducer was designed as a single-single type, with periodicity set to 160 μm, for 30 periods (N = 30) . To excite the SSAW device, a signal generator (DSG4102, Rigol) was coupled to an amplifier (Henry Radio 20B, USA). Velocity of the samples within the drop was controlled by amplitude of the signal waveform, with pulse duty cycle being used to limit the power added to the device. A 24 MHz 50% duty cycle pulsed sine waveform was used, which was additionally globally cycled at 1 s intervals. Velocity was calculated by digital image correlation.

5.3.1 Device mount

The beamline mount was 3D-printed using Accura – 60 resin and a 3D Systems Viper SLA printer. The mount is composed of two parts: a removable chip to allow device transducer

swapping; a base designed to secure the transducer within to existing mounting points at the beamline. Figure 5.3 pictures the experimental arrangement (offline) and is included for clarity alongside Figure 5.4 which is an expanded view of the chip arrangement. The chip was additionally formed of LiNbO3 which was patterned with the IDT fingers, two laser cut contact restraints, and thread inserts to avoid thread issues from the soft SLA material and finally a thick copper foil was trimmed to allow connection.

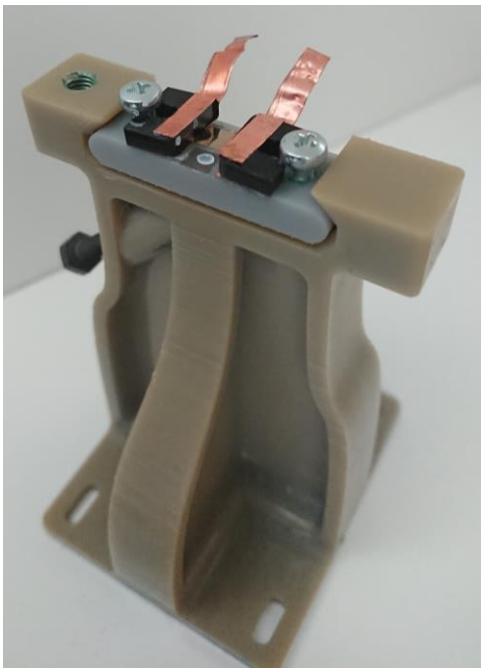

Figure 5.3 Assembled goniometer device

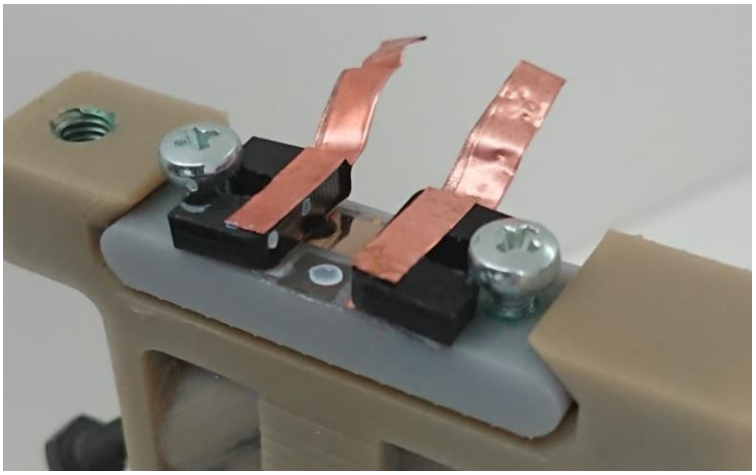

Figure 5.4 Close-up view of the IDT-chip arrangement.

5.3.2 Contact Angle Modification

A hydrophobic surface was fabricated by Scientific Device Laboratory (Scientific Device Laboratory, USA), an inkjet-printed fluorinated ink was selectively patterned onto a Kapton substrate. Composed of a solid block of colour except for a small hydrophilic dot in the centre designed to locate the crystal laden drop, see Figure 5.5. Fixing was achieved using material was fixed using ethyl cyanoacrylate glue (Loctite 401) to enable effective transmission of the surface wave through and into the film and fluid. Measured sessile water drop contact angle for a located drop was measured at 84°, compared to 64° for Kapton Hn Cole-Parmer, UK) alone, illustrating its more hydrophobic character.

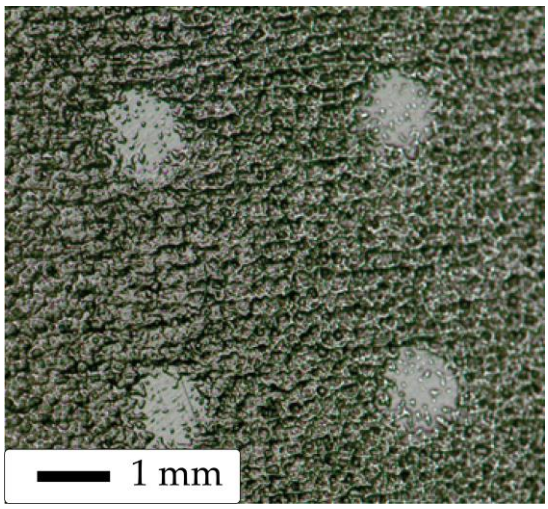

Figure 5.5 Digital microscopy image of the printed hydrophobic ink locating pattern.

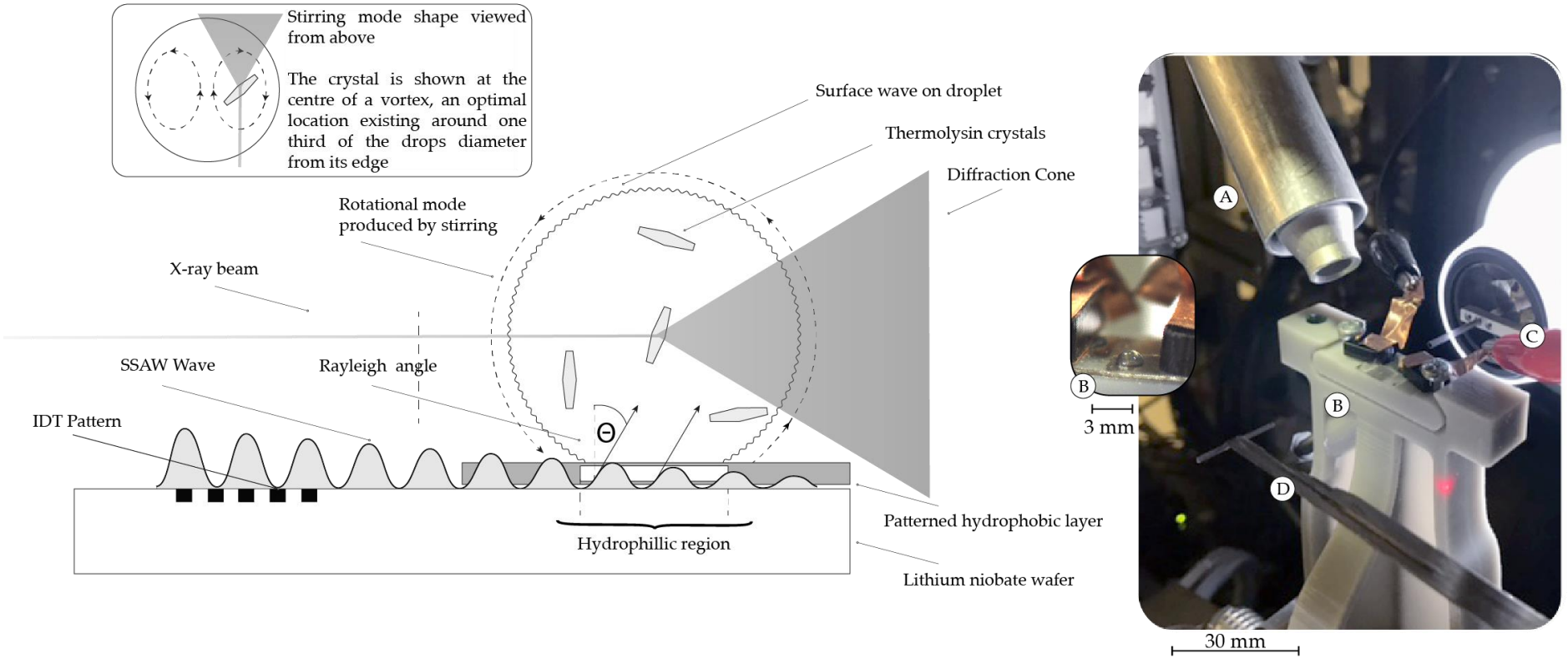

Figure 5.6 Schematic of the on-chip goniometer

5.3.3 *Thermal Characterisation*

Infrared measurements were taken to evaluate the heating experienced by the drop during stirring using a Fluke Ti400 on a fixed mount over a period of 1 minute. This is comparable with the length of time a single drop was exposed to the X-ray beam and SSAW stirring.

5.3.4 *Sample preparation*

Protein crystals were prepared by in-house biologist Tracey Keates at Diamond Light Source. Commercial thermolysin from Bacillus thermoproteolyticus (~40U/mg, Sigma-Aldrich) was resuspended to a concentration of 50 mg ml^{-1} in a solution of 45% dimethyl sulfoxide, 0.5 M NaCl and 50 mM 2-(*N*-morphlino)ethanesulfonic acid (MES buffer) to a pH of 6.0. Sitting drops were made by mixing 2 µl protein solution and 2 µl reservoir solution, consisting of 1.2 M ammonium sulfate in 18.2 MΩ water, and equilibrated against 300 µl of this reservoir solution at 20 °C in sealed trays. Crystals approximately 50 x 50 x 200 µm in dimension grew within 7 days as shown in Figure 5.7. Immediately prior to data collection 2 µl of a sitting drop was manually transferred by pipette to the chip surface.

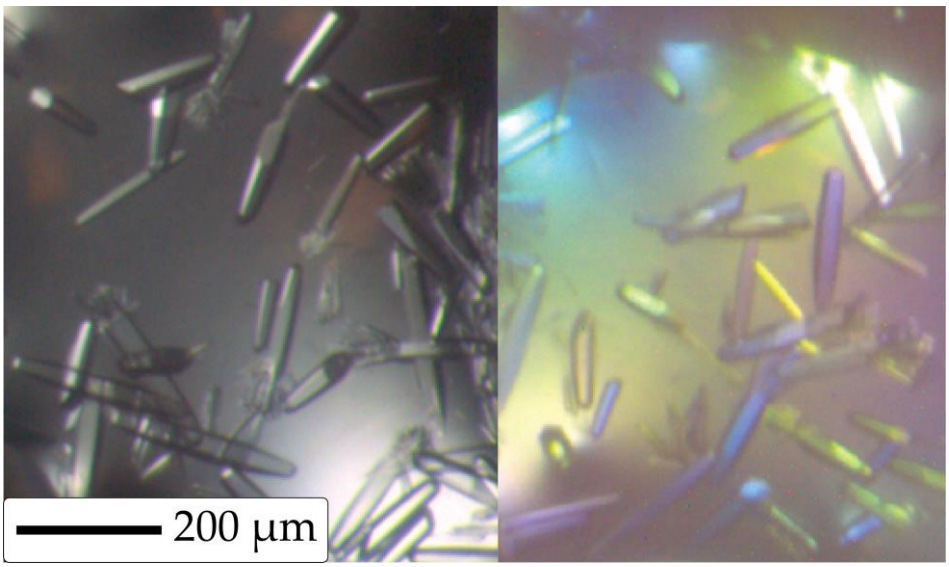

Figure 5.7 Thermolysin crystals under white light (left) and polarised white light (right).

5.4 Synchrotron data collection

It is important to note that the processing of the X-ray data was carried out by Dr D Axford, beamline scientist at Diamond Lights Source. Experiments took place at beamline i24 at the Diamond Light Source, Harwell, Oxford. The X-ray beam was defocused to 50 μm^2 to best match the dimensions of the crystal within the drop (between 50 and 200 μm). During studies the drop was approximately 1800-2500 μm diameter dependent intersection point of the beam with the drop. Diffraction data were recorded with a Pilatus3 6M operating at its maximum frame rate of 100 Hz. Using an on X-ray beam axis camera, the beam was aligned to a point approximately consistent with the vortex centre in and at a height of approximately 3/4 of the total drop to limit shadowing on the detector from the edge of the chip.

To prevent the sample-containing droplet from evaporating in the dry air of the beamline (ambient humidity recorded at 17% by portable device) the HC1 sample humidity control device was used.[44] This provided a constant flow of 96% humidity air over the drop at 293 K, it is important to note that no contribution to sample motion was observed from the airflow.

5.4.1 Bragg spot diffraction data processing

Table 5.1 Summary statistics for diffraction data processing and refinement.

Data collection	Exposure Time (ms)	10
	Beam size (μm)	50 x 50
	Wavelength (Å)	0.9686
	Incident flux (photons s^{-1})	6 x 10^{11}
	No. integrated frames	2796

	No. scaled & merged frames	2670
Scaling	Space group	$P6_122$
	Unit cell parameters (Å)	93.6, 93.6, 129.8
	Resolution range (Å)	44.0 – 2.0 (2.2 – 2.0)
	R_{split}	0.092 (1.038)
	$CC_{1/2}$	0.993 (0.290)
	$(I/\sigma(I))$	2.19 (0.19)
	Multiplicity	61.20 (42.1)
	Completeness (%)	99.2 (99.8)
Refinement	No. reflections	26888
	No. non-H atoms (Protein)	2480
	No. non-H atoms (Water)	108
	R/R_{free}	0.201/0.256
	R.m.s.d, bond lengths (Å)	0.010
	R.m.s.d., bond angles (°)	1.11
	Ramachandran outliers (%)	0
	Side chain outliers (%)	0.8
	PDB code	5O8N

5.4.2 Structure solution

The crystal structure was solved using molecular replacement with protein data bank (pdb) entry 5UU9 truncated to polyalanine. Model building was completed using Phenix autobuild and Coot and refinement was performed with Phenix refine. Statistics for data collection and refinement are presented in Table 5.1.

5.5 Results and Discussion

The SSAW transducer was designed to achieve a resonant frequency of 24 MHz which gave a short wavelength while allowing for a high device yield during production. The sharp frequency response of the device can be seen in Figure 5.8 Fabricated SSAW transducer frequency response. where the -3dB bandwidth was 0.02 MHz (-3 dB is the point that corresponds to a 50% received signal power reduction).

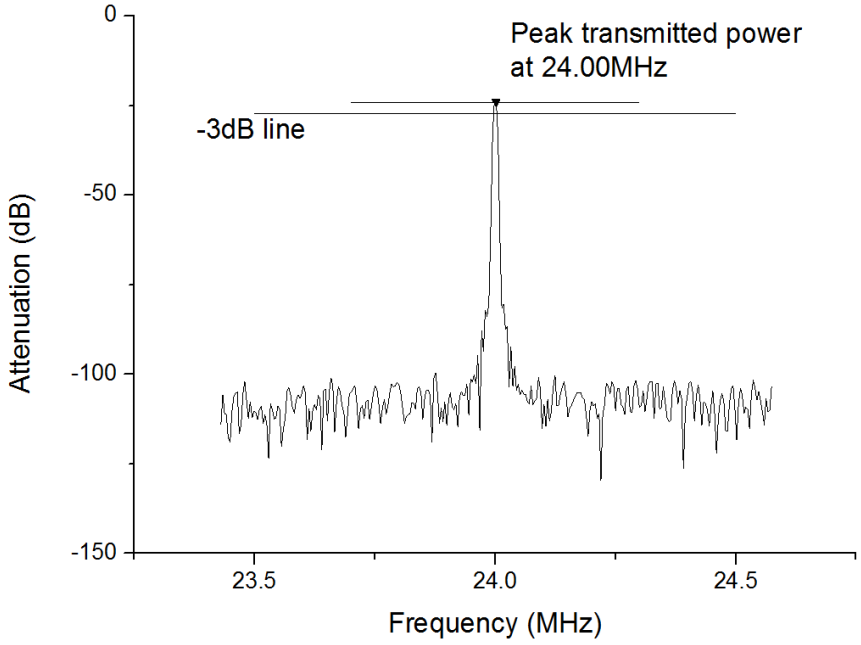

Figure 5.8 Fabricated SSAW transducer frequency response.

Off beam trials showed that after 30 s of SSAW actuation no significant droplet reduction occurred *via* evaporation or ejection. The switching pattern was determined through observation of the inertia of the moving crystals and fluid needed to maintain sufficient rotation.

5.5.1 Thermal Imaging

Results of thermal imaging, partially reproduced in Figure 5.9 showed the drop experienced a heating rate of approximately 42 mJ s^{-1}. In context the heating rate was equivalent to 0.1 K s^{-1},

with both the drop and piezo temperature benefitting from reduced heating due to the waveform described in section 5.3. At the time of writing, the typical period for continuous diffraction was approximately 50 s.

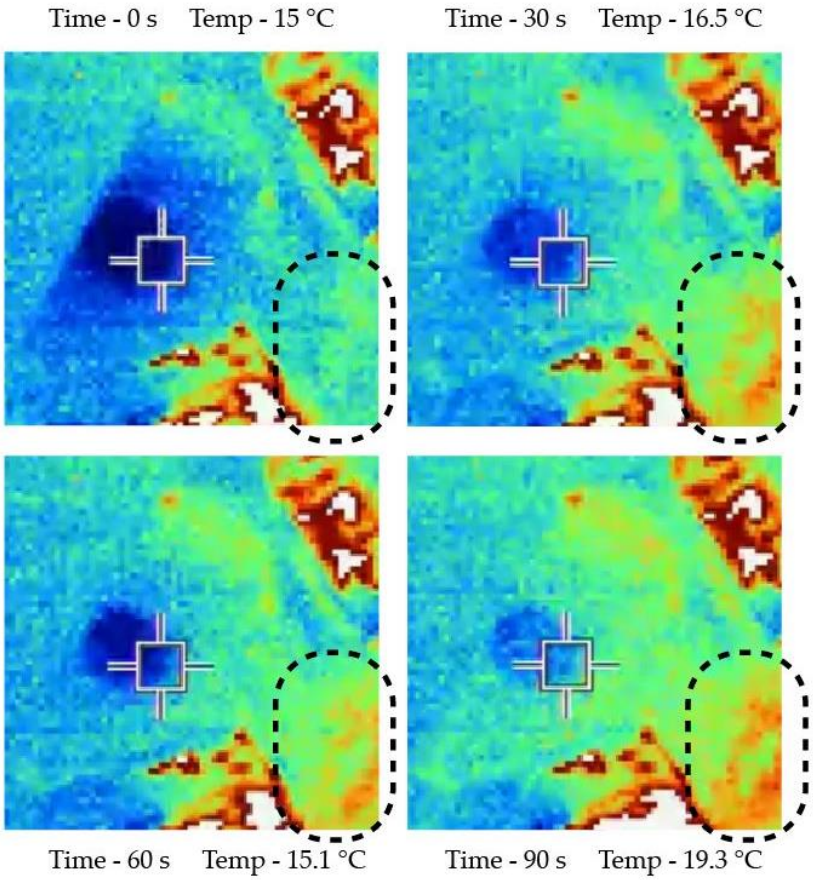

Figure 5.9 Infrared imaging of the surface acoustic wave device during operation. The dashed region highlights the IDT, and the darker blue region is the crystal drop.

5.5.2 *Amorphous type background scatter*

Assessing the experimental arrangement with respect to background scatter, Figure 5.10 shows a single diffraction still taken during experiment, and gives a qualitative perspective on the level of background scattering occurring during the experiment. Some shading occurred as a result of the non-X-ray transparent lithium niobate. Region (A) shows no shading and region (B) shows that the approximately symmetric amorphous scattering ring (wide angle X-ray scattering) pattern is partially attenuated. Defective pixels are shown in white. During

operation only the drop and any crystals within the drop intersected the incident beam. For the duration of the study, the drop was composed entirely of thermolysin crystallisation condition. After striking the drop some shading occurred that was dependent on the distance between the beam and the lithium niobate transducer. The shading is a side effect of a totally un-restrained drop, particularly those containing poly(ethylene glycol), which when subjected to ultrasound experiences a gradual increase in wetting [155], [166].

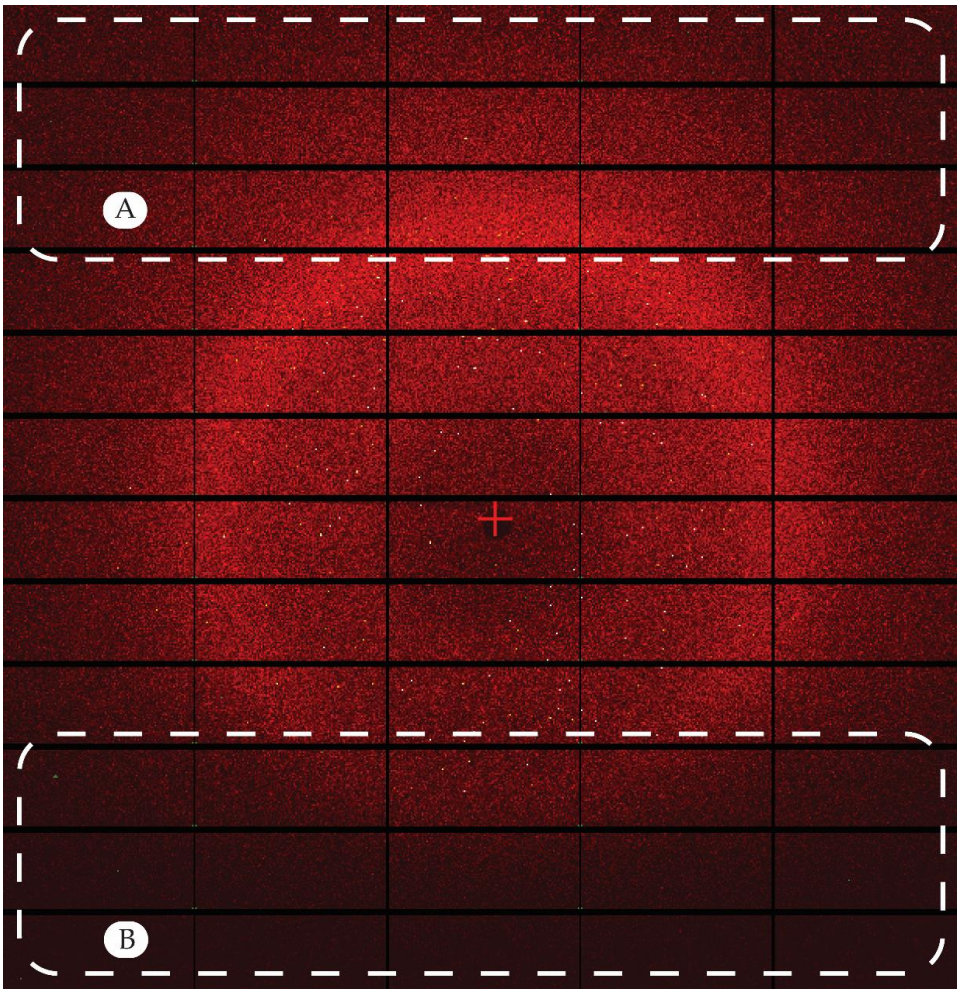

Figure 5.10 Diffraction static used for background scatter determination, captured during the acoustic rotation of thermolysin. Region (A) shows a significant different in amorphous scatter when compared to region (B), attributed to shading by the lithium niobate chip.

Eight statics taken during background scattering experiments were processed in accordance with Section 2. The Pilatus 3 detector (Dectris, Switzerland), records a count each time sufficient X-ray photons reach a pixel, recorded as counts per second (CPS). The detector is capable of doing this well in excess of 1 MCPS. It was found that the sample holding arrangement gave < 35 CPS across the detector, typically < 20 CPS and < 15 CPS, in the 2 Å region as shown in Figure 5.11 in blue. However, these figures must be adjusted upwards to compensate for the reduction in average radial intensity coming from shading, an estimate of a 30% shading factor was used and the adjusted results are also shown in Figure 5.11 in grey. The air scatter trace is provided for comparison and represents the minimum achievable background scatter, while providing context for the contribution to scattering made by the sessile drop.

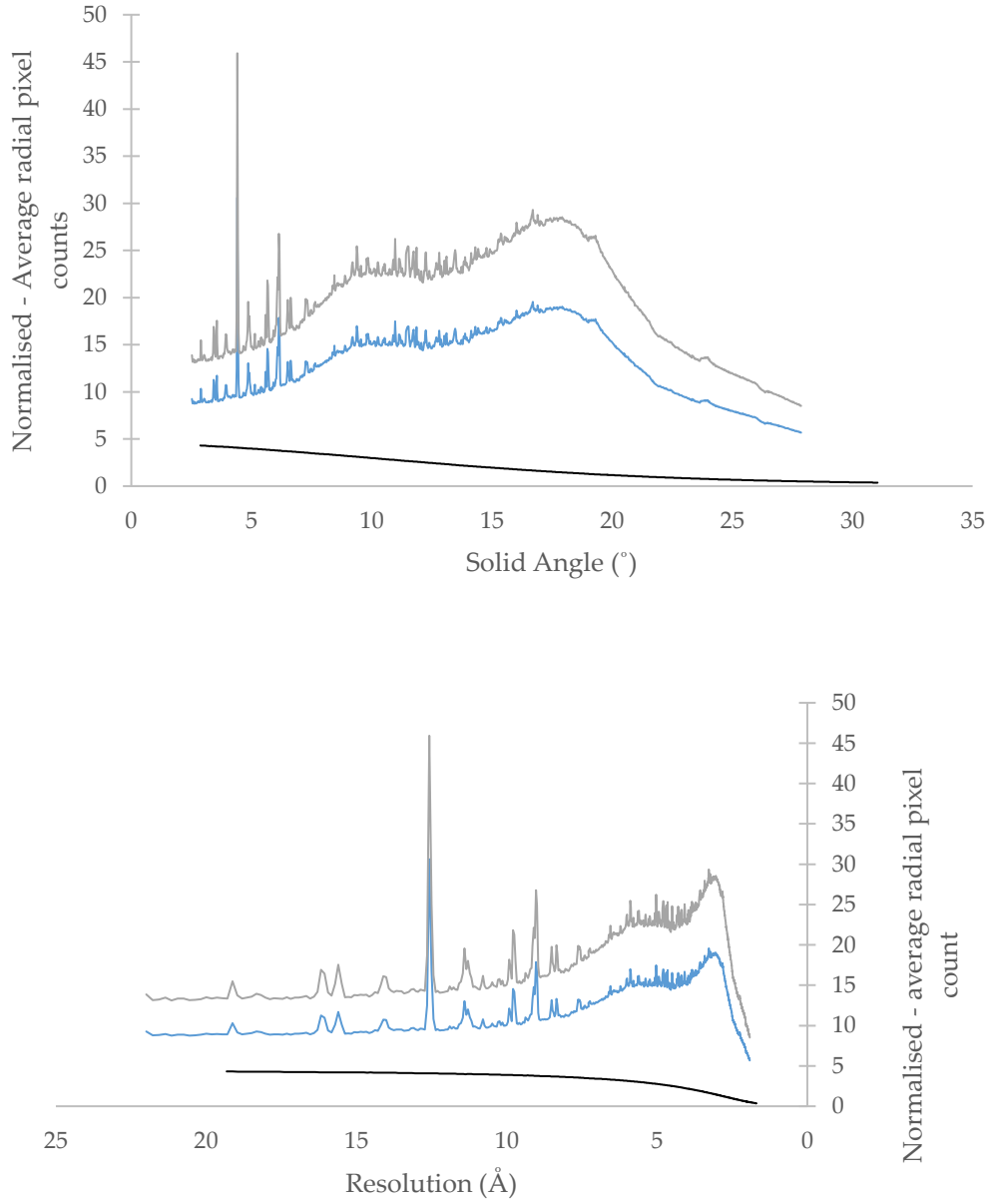

Figure 5.11 Plots showing averaged background scatter as a function of solid angle (top) and resolution (bottom), shading-adjusted normalised background scattering (grey), normalised background scatter (blue), and air scatter (black)

The background scatter was anticipated at a high level, as the drops were not restrained, and gave a beam path of 1 mm or more through crystallisation fluid. Despite this disadvantage high quality diffraction data was observed as seen in Figure 5.12.

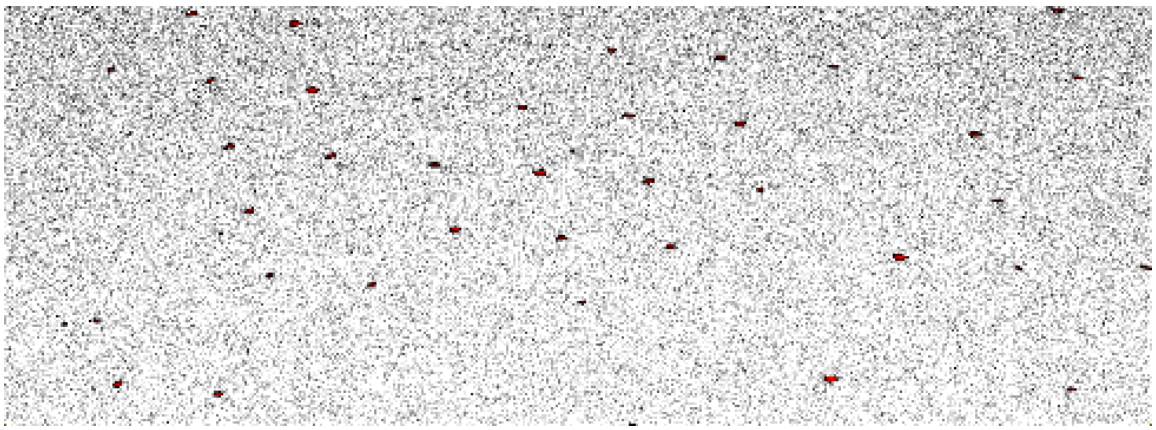

Figure 5.12 Section of a diffraction still taken during beamtime 14493-42, showing diffraction spots in comparison to background scatter.

Diffraction created Bragg spots may strike the detector, and produce a pixel intensity from the minimum the detector may record upwards, with Bragg spot intensity typically reducing at higher resolutions. The background scatter demonstrates plausibility of the technique even in sub optimal configurations. Integration of this method into a complete microfluidic system would almost certainly shorten the path length to a level comparable with state-of-the-art on the field.[128]

5.5.3 Crystal motion

Crystal translation during operation was monitored using custom telecentric video imaging with an arrangement to give optimal depth of field. Various mountings were used to achieve a birds-eye view of the drop, and a 1.7x high resolution lens for optimised depth of field and resolution (#63-232, Edmund Optic UK). Motion of crystals within the drop ranged between gentle rocking of a crystal (mimicking the small rotation method of a goniometer) to greater than 15 000 μm s^{-1} at high signal amplitudes, which is markedly faster than current detector frame rates and gave rise to increase in drop heating.

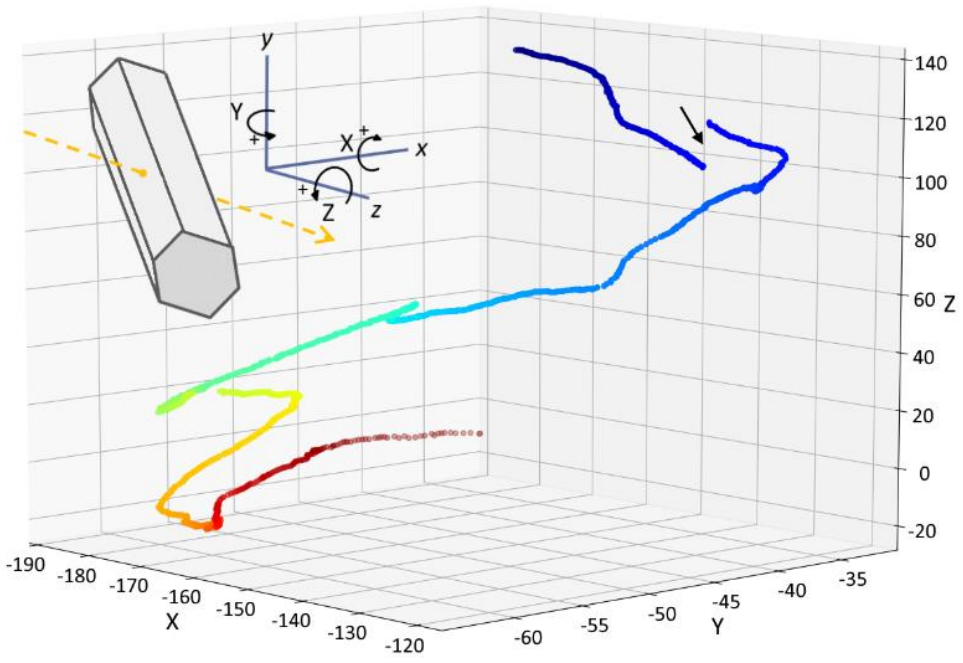

Figure 5.13 A 3 dimension scatter plot of Euler x,y,z rotation angles (in degrees) derived from the orientation matrix from 1709 diffraction images across which a consistent and unambiguous indexing solution could be tracked, thus illustrating the motion of the sample. The colour map indicates the sequence of observations from blue to red. The in-laid schematic describes the beamline coordinate system with the X-ray beam (dashed arrow) along the Z axis and the angles X,Y,Z representing rotations about the respective x,y,z axes. The black arrow indicates a gap where the crystal briefly moved out of the beam. An animation of the rotation is included in supplementary information ESI 5

The widening velocity ranges in Figure 5.1 (indicated by error bars) are due to the centre and the edge of a rotating system having different velocities. This implies that a vortex or other complex rotation is induced by the SSAW interacting with the drop. Differences in translational velocity between the drop centre and edge naturally increased with rotational speed. During diffraction SSAW power was applied to achieve an actuation speed range of approximately 0-800 μm s^{-1} in the XY plane. This velocity implies that a single crystal within a multi-crystal drop could intersect the beam for between 6 and 25 detector frames (at 100 Hz)

with the full crystal while in pure translation. However, in the instances when the crystal arrives at the centre of a vortex within the drop, the crystal may be imaged in a stream of consecutive frames, as illustrated by the tracking of incremental changes in the rotation matrix for each processed diffraction image. A video showing stirring motion is included in the supporting information ESI 3.

Whilst acoustic sample manipulation has seen prior application *via* a levitating droplet, we use a surface-based method, compatible with a continuous microfluidic on-chip device, with the potential for high sample throughput and initiation of enzyme reactions for dynamic studies.[81], [167] In comparison to more conventional microfluidic sample handling systems, acoustically induced sample orientation enabled the acquisition of a complete set of reflections without the need to move the device itself.[168], [169]

The thermolysin crystal structure (pdb 5O8N) was determined from a collection run of 5000 images, 2670 of which made up the final dataset, and statistics are presented in Table 5.1. The dataset is from a single drop and likely from a single crystal however there is a gap of ~200 frames within the block of useful images where no diffraction is seen and the possibility of an exchange of crystals at this point cannot be completely ruled out. An example of electron density is provided in Figure 5.14.

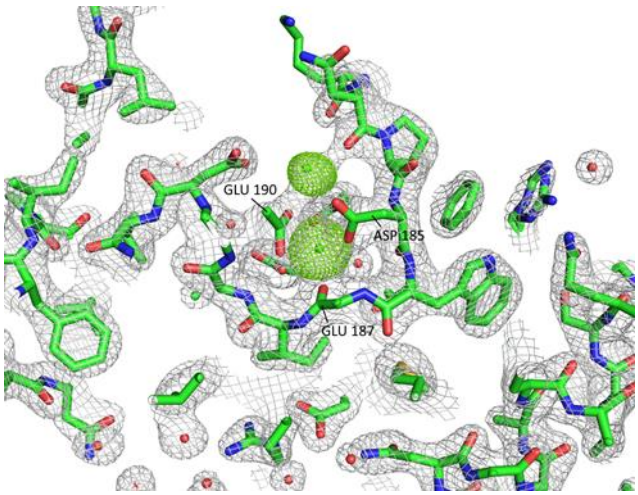

Figure 5.14 Example of electron density map to 2.0 Å resolution around the thermolysin model 5ON8. In this case the occupancy of two calcium atoms has been set to zero and a 2Fo-Fc map is shown (contoured at 1 σ) and a Fo-Fc difference map (contoured to 5σ) which highlights these atom sites in green, indicating scattering in the data not accounted for in the reduced occupancy model.

Using Raddose-3D and assuming a single crystal consistently illuminated, average diffraction weighted X-ray dose was calculated at 0.6 M Gy.[170] This is of the order of the maximum dose from which useful diffraction data can be collected at room temperature and there was no obvious decrease in diffracting power seen in the later diffraction images.[59] Data confirms the ability of the device to produce useful structures from acoustically perturbed μl volumes, without moving parts or crystal mounting. The dataset reflects a crystal captured at the centre of the vortex and rotating relatively slowly (Figure 5.13). Processing *via* a serial method assumes each detector frame to be an individual experiment and refines an independent crystal lattice orientation for each instance. Refined crystal lattice orientation for adjacent detector frames with consistent indexing from the dataset is plotted in Figure 5.13. The continuous line indicates a single lattice is being tracked and the plot displays the motion of the crystal during the data collection. A break in the line (arrow) indicates where the crystal has temporarily moved out of the beam. The predominant motion is a ~180° rotation about the

z axis (beam axis) accompanied by ~60° about the x axis (horizontal) and ~35° about the y axis (vertical). The speed of rotation can be seen to vary during the collection. The plot represents a time series of ~17 s equating to an average rotation speed about the dominant axis of ~10°s^{-1} or ~0.1° per detector frame. The ability to measure a complete set of crystal reflections is most likely enhanced by the fact that rotation of the crystal is not about a single fixed axis. However, there is currently no software able to properly handle such a goniometer-based experiment. Therefore, in this case, serial crystallography methods were needed to analyse detector frames on an individual basis. Routines are currently under development to correctly model the varying motion of the sample from frame to frame with the expectation of improving data analysis from this type of experiment.

5.6 Conclusions

The on-chip crystal rotation method designed and developed in this work enables efficient room temperature *in situ* X-ray data collection of protein crystals without the need for multi-axis goniometry and complex precision motion systems. The diffraction data acquired from the device are of good quality, despite a sub-optimal X-ray background and scattering cone. The wide range of speed control achieved by varying input power allowed sample translation and rotation at speeds appropriate to the 10 ms detector read out time, boosting data collection efficiency and quality. Precise X-ray dose quantification for the experiment is difficult since the relatively unconstrained motion of the sample is likely to be bringing fresh sample volume in and out of the beam. Although crystal diffracting power was not seen to dramatically decline over the dataset, the chance of radiation-induced changes should always be anticipated at room temperature. Going forward, the incorporation of microfluidics into the experimental

design is planned. A full lab-on-a-chip system is envisioned, moving towards automated sample delivery without the need for costly and complex robotics or time consuming user mounting. A sealed environment would be a valuable addition, preventing liquid loss *via* evaporation and removing the need for humidity control. In summary this technique has been proven for the first time to meet the demanding needs of macromolecular protein crystallography, and by achieving a high resolution structure the device makes a significant stride in automating sample handling.

6 Discussion, Conclusions and Further Work

6.1 Discussion

Considering acoustic goniometry and acoustic trapping, it is evident that both techniques contain significant potential. The marketplace within crystallography has seen a trend looking to increase the capacity of fixed target methods, and has made great progress in arraying multiple samples in diffraction compatible plates or micro-arrays. A comparison between protein crystal mounts which have space for one hundred microcrystals in a neatly ordered grid provides a high bar for entry for acoustic systems. To contrast a fixed target grid with a standing wave acoustic trap, it is important to reflect on the speed of individual crystal targeting, the speed of changeover between crystals, the speed of change of any device, the experimental flexibility, the researcher time required to achieve the method, and finally the likely quality of data achieved.

Acoustic trapping may improve the experimental flexibility over fixed target methods, as the microfluidic arrangement lends itself to the addition and removal fluid volumes around a trapped crystal this would however seriously challenge the architecture of a fixed grid or crystallisation plate target since each individual cell would require a fluid path. Unless crystals were to be exposed to a substrate on-mass then fixed target methods require as many fluid ports as chambers, quickly becoming complex.

With respect to targeting, it is unlikely that an acoustic trap would match the speed of fixed target methods, since the crystal positions are moveable within the acoustic system. There is potential to use fluid actuation of crystals, avoiding any need to move a positioning stage

between crystal locations or moreover removing the need for secondary devices as is the case of fixed target crystallisation plates. In contrast the acoustic trapping system may be adapted to handle crystals numbering over a thousand through simple fluidic tubing arrangements.

Comparing cost with existing systems, a value-engineered single acoustic chamber is likely to be an order of magnitude lower than similar fixed target system, since chambers may be made of X-ray compatible polymer such as a polyimide or cyclic-olefin-copolymer. Fixed target methods may make use of such systems but since components are essentially disposable, an acousto-fluidic system, with small form factor, of the order of 10 mm for the acoustic system *vs*. 100 mm for crystallisation plates, perhaps favours the acoustic method.

6.1.1 Device performance relative to operational design inputs

Although both techniques were produced as proof-of-concept devices it is important to evaluate them with respect to design inputs.

6.1.1.1 On chip goniometer

To produce sufficient rotation to enable the collection of a complete dataset.

The on-chip goniometer was able to capture a complete dataset using a simply pulsed excitation. It is probable that the rotation speed could be effectively and accurately controlled using a more complex excitation. In this respect the device is capable of meeting data collection needs

To avoid excessive application of heat to the crystal sample

The generation of acoustic power can produce significant heat in target zones, however due to the low speed requirements the device was shown to avoid excessive heat build up and may be said to meet data collection needs.

To allow user control of the rate of rotation

Rotation speed was observed to be a function of vortex speed, which was in turn observed to be a function of the input power, as such the speed was user controllable and it is anticipated that more refined control would be possible in an expanded system.

To avoid excessive crystal translation, allowing the effective collection of data

In operation it was found that the use of the minimum power required to produce crystal rotation allowed a crystal to remain centred in the beam path, in this regard the method showed itself as capable of effectively collecting data.

To generate minimal background scatter during diffraction

Background scattering data was collected and the device showed that it did not produce excessive noise within the high resolution diffraction region.

To generate sufficient acoustic force to excite a vortex within a drop.

A vortex was successfully excited therefore the device performed ably. There is scope however to consider lower frequency transducer design as this may reduce the subsequent heating and offer an expanded range of operation, e.g. high power signals for shorter periods.

The presence of sufficient vortex force to produce rotation of the target crystal.

The crystal was successfully rotated in the study.

The retention of crystals within a stable trapping position for a duration allowing their targeting and diffraction.

Crystals were observed as stable in both the vertical and horizontal planes however the stability is likely to be affected by the crystal content of a drop. A higher number of crystals would likely force collisions to occur, as such further study into crystal laden drop optimisation would be needed to fully describe expected operational conditions.

A stable form of trapped-crystal motion allowing effective beam targeting.

The beam remained relatively motionless once it had been aligned to the center of the vortex within the drop. It should be noted that the stability is reliant on crystal contact with the transducer surface.

To allow scattering data to escape enabling < 2 Å data collection.

Bragg spots were identified from scattering- data collected within the < 2 Å, as such the system meets this criteria.

Developed arrangement must be inert relative to the crystallisation fluid and the crystals themselves.

The crystal and fluid showed no sign of interaction and the resolved structure was not shown to have any ligand binding in effect, to this extent it can be considered inert and suitable for use.

In summation the on-chip goniometer served as a useful proof of concept and similar arrangements would be an effective starting point for further device developments.

6.1.1.2 Standing wave-trap

Sufficient acoustic pressure to enter the fluid cell to allow the excitation of a standing wave within the fluid.

The device was capable of creating a strong enough acoustic field to enable crystal trapping in-situ. Analysis of the experimental arrangement suggests that a redesign of the acoustic connection between the transducer and the chamber to include a matching layer would dramatically reduce the required input power for the study.

Multiple wavelengths contained within a single window, allowing for an array of crystals to be trapped.

An array of stable trapping positions were observed to capture crystals. A study of the modes produced within the acoustic chamber would further characterise the system and allow for predictive trapping positions.

The presence of sufficient acoustic force to cause the trapping of protein crystals

The retention of crystals within a stable trapping position for a duration allowing their targeting and diffraction, as such the system can be considered effective.

A stable form of trapped-crystal motion allowing effective beam targeting.

The crystal motion was measured and found to be sufficient for trapping.

The arrangement of a fluid cell which was capable of sustaining a standing wave.

The fluid cell successfully sustained a standing wave / resonant mode for the duration of the study.

The arrangement of a fluid cell which was sufficiently transparent to X-rays to allow scattering data to escape enabling < 2 Å data collection.

Background scatter data was collected and suggested that it would be possible to collect data within the < 2 Å region however crystal quality was not sufficient to allow this to be verified through Bragg spot identification.

Developed fluid cells must be inert relative to the crystallisation fluid and the crystals themselves.

Fluid cells were composed of silicon-nitride which is well studied and has been demonstrated inert.

In summary the device was shown to be functional and to enable the practical trapping of crystals in-situ. Further development into trapping modes which ay be excited within the acoustic chamber, and the effect of crystallisation fluid on these modes, combined with the inclusion of an acoustic matching layer would be an able start point for further development of this system.

6.1.1.3 The standing-wave trap

A precision angle mount to allow the matching of the (111) plane of the silicon nitride to the output of the transducer. Such a mount would enable the removal of the water connection and significantly improve the efficiency, thus reducing the power requirement for operation. Such an arrangement would likely be best manufactured using electro-discharge machining and highly specific alignment is entirely practical.

6.2 Conclusions

Within this thesis two separate acoustic methods have been studied to demonstrate applicability for macromolecular protein X-ray crystallography. The outcome for each method studied included diffraction stills, background noise profiles and Bragg spot counts, as such the experiments themselves succeeded in generating novel data. The acoustic goniometer created sufficient data to allow a structure to be determined, a major milestone. This pushes the system towards a next milestone where speed and efficiency of operation may be brought to the fore. Whilst proof of concept work should not be compared with fully developed systems, it is useful to seek indications of how a final version may perform. Since mounting and external rotation were not involved during the diffraction process, it was definitively an unsupervised process. The practical experimental considerations mean that in the present form the technique is not suited for routine use, as the hand mounting and pipette methods required both practice and a steady hand. However, further iteration, where drop mounting and removal methods were automated would create a device capable of exciting and high throughput protein studies. The technique is reliant only on the propensity of protein crystals to sink, and the ability of surface-acoustic-waves to interact and form vortices in droplet the

technique leaving scope for a wide range of optimisation. Further, since acoustic streaming is present within micro channel confines also, the experiment described herein offers proof of concept for a parallel study in microfluidic acoustic goniometer also.

Acoustic mounting of protein crystals was able to create a dataset that included background noise quantification, X-ray beam attenuation and crystal motion, so as a study it may be considered a success. However the lack of sufficient data to reconstruct the protein structure means that the technique requires further study before it is considered to have passed the proof of concept stage. Anecdotally the trapping produced a pleasant gentle rotation from crystals around at around one Hertz as a result of acoustic streaming. In practical terms this suggests that the technique may be particularly well suited to crystal data capture.

6.3 Further Work

Given that protein crystals have a different density to salt crystals, acoustic sorting technology would also be a natural progression in the study of high-throughput protein crystal analysis. The acoustic contrast of a single crystal sample would be sufficiently different based on salt content to allow selectivity. Crystals would however need to be pre-sorted based on size to avoid overlap between larger protein laden crystals and smaller but denser salt laden crystals.

To advance the on-chip goniometer towards a point where it would be a useable beamline tool, the incorporation of an off the shelf acoustic droplet ejection mounting system in combination with a form of compressed air jet to remove a diffracted droplet from the stage, would allow for a mount free throughput test.

The experimental determination of wave patterns is challenging to achieve, authors have recently reported the ability to detect pressure wave through the use of refractive index

changes which are the result of the pressure variations induced by a standing wave. Properly called 'Synthetic-Schlieren Optics', an image of known black and white geometry is viewed through the pressure variations, the resultant distortion is mathematically calculated from the implied refractive index shift and the pressure distribution may be visualised.[171], [172] At the time of writing this had only been achieved at the macro scale and not within the sphere of microfluidics. Such a system would enable users to assess the operation of an acoustic device without the need for the contamination or disassembly, moreover the results would be readily apparent to a non-specialist.

The development of machine-learning control for the controlled rotation of a crystal would develop the on-chip goniometers ability to ensure a dataset included a complete set of reflections. Any system would however, need to adapt to the rotation of the crystal being the result of a relatively continuous vortex, moreover the position of the crystal within the drop also significantly alters the force it would experience.

Finally, the collection of a further dataset to demonstrate acoustic trapping would allow the technique to be considered in its fullness and pave the way for more complex studies involving time resolved substrate binding.

References

[1] "Macromolecule (Polymer Molecule)," *IUPAC Compend. Chem. Terminol.*, vol. 2287, p. 3667, 1996.

[2] J. M. Berg, J. L. Tymoczko, and L. Stryer, "Biochemistry," in *Biochemistry textbook*, 2010, p. 1026.

[3] R. L. Schmidt and M. Simonović, "Synthesis and decoding of selenocysteine and human health," *Croat. Med. J.*, vol. 53, no. 6, pp. 535–550, 2012.

[4] C. K. Mathews and K. E. van Holde, "Biochemistry," *J. Chem. Educ.*, vol. 68, no. 1, p. A21, 1991.

[5] S. Honda, T. Akiba, Y. S. Kato, Y. Sawada, M. Sekijima, M. Ishimura, A. Ooishi, H. Watanabe, T. Odahara, and K. Harata, "Crystal structure of a ten-amino acid protein," *J. Am. Chem. Soc.*, vol. 130, no. 46, pp. 15327–15331, 2008.

[6] W. Massa, *Werner Massa Crystal Structure Determination*. 2000.

[7] E. Garman and R. L. Owen, "Cryocrystallography of macromolecules: practice and optimization.," *Methods Mol. Biol.*, vol. 364, pp. 1–18, 2007.

[8] J. P. . Glusker, M. Lewis, and M. Rossi, "Crystal Structure Analysis for Chemists and Biologists," *VCH Publishers*, vol. 1. p. 837, 1994.

[9] D. Jeruzalmi, "First analysis of macromolecular crystals: biochemistry and x-ray diffraction.," *Methods Mol. Biol.*, vol. 364, pp. 43–62, 2007.

[10] J. M. Holton and K. A. Frankel, "The minimum crystal size needed for a complete diffraction data set," *Acta Crystallogr. Sect. D Biol. Crystallogr.*, vol. 66, no. 4, pp. 393–408, 2010.

[11] C. P. Poole and F. J. Owens, "Introduction To Nanotechnology - Poole , Owens.pdf," *Collection Management*. 2003.

[12] J. M. Grimes, D. R. Hall, A. W. Ashton, G. Evans, R. L. Owen, A. Wagner, K. E. McAuley, F. Von Delft, A. M. Orville, T. Sorensen, M. A. Walsh, H. M. Ginn, and D. I. Stuart, "Where is crystallography going?," *Acta Crystallogr. Sect. D Struct. Biol.*, vol. 74, pp. 152–166, 2018.

[13] The Diamond Light Source, "Campus Aerial View." 2015.

[14] The Diamond Light Source, "Diamond Beamlines." 2014.

[15] A. Thompson, "X-ray data booklet," *Centre for X-Ray Optics and Advanced Light Source*, vol. 8, no. 4. pp. 1125–1125, 2009.

[16] J. Als-Nielsen and D. McMorrow, *Elements of Modern X-ray Physics: Second Edition*. 2011.

[17] T. D. Lightsource, "The Machine." [Online]. Available: http://www.diamond.ac.uk/Science/Machine.html.

[18] J. M. Thomas, "Centenary: The birth of X-ray crystallography," *Nature*, vol. 491, no. 7423. pp. 186–187, 2012.

[19] C. Kittel, *Introduction to Solid State Physics*. 2010.

[20] P. Paul, *An introduction to electrospinning process*, vol. 48, no. 10. 2005.

[21] C. A. Smith and A. E. Cohen, "The Stanford Automated Mounter: Enabling High-Throughput Protein Crystal Screening at SSRL," *JALA - J. Assoc. Lab. Autom.*, vol. 13, no. 6, pp. 335–343, 2008.

[22] G. Snell, C. Cork, R. Nordmeyer, E. Cornell, G. Meigs, D. Yegian, J. Jaklevic, J. Jin, R. C. Stevens, and T. Earnest, "Automated sample mounting and alignment system for biological crystallography at a synchrotron source.," *Structure*, vol. 12, no. 4, pp. 537–

45, 2004.

[23] D. Nurizzo, M. W. Bowler, N. Guichard, S. McSweeney, P. Theveneau, M. Guijarro, O. Svensson, C. Mueller-Dieckmann, and G. Leonard, "Automated data collection based on RoboDiff at the ESRF beamline MASSIF-1," *AIP Conf. Proc.*, vol. 1741, 2016.

[24] A. E. Cohen, P. J. Ellis, M. D. Miller, A. M. Deacon, and R. P. Phizackerley, "An automated system to mount cryo-cooled protein crystals on a synchrotron beamline, using compact sample cassettes and a small-scale robot," *J. Appl. Crystallogr.*, vol. 35, pp. 720–726, 2002.

[25] M. Cianci, G. Bourenkov, G. Pompidor, I. Karpics, J. Kallio, I. Bento, M. Roessle, F. Cipriani, S. Fiedler, and T. R. Schneider, "P13, the EMBL macromolecular crystallography beamline at the low-emittance PETRA III ring for high- and low-energy phasing with variable beam focusing," *J. Synchrotron Radiat.*, vol. 24, no. 1, pp. 323–332, 2017.

[26] B. G. Abdallah, "Microfluidic Tools for Protein Crystallography," 2016.

[27] K. Dörner, J. M. Martin-Garcia, C. Kupitz, Z. Gong, T. C. Mallet, L. Chen, R. M. Wachter, and P. Fromme, "Characterization of Protein Nanocrystals Based on the Reversibility of Crystallization," *Cryst. Growth Des.*, 2016.

[28] D. J. Kissick, D. Wanapun, and G. J. Simpson, "Second-Order Nonlinear Optical Imaging of Chiral Crystals," *Annu. Rev. Anal. Chem.*, 2011.

[29] A. S. Pawate, V. Šrajer, J. Schieferstein, S. Guha, R. Henning, I. Kosheleva, M. Schmidt, Z. Ren, P. J. A. Kenis, and S. L. Perry, "Towards time-resolved serial crystallography in a microfluidic device," *Acta Crystallogr. Sect. Struct. Biol. Commun.*, vol. 71, pp. 823–830, 2015.

[30] B. Heras and J. L. Martin, "Post-crystallization treatments for improving diffraction quality of protein crystals," *Acta Crystallogr. Sect. D*, vol. 61, no. 9, pp. 1173–1180, Sep. 2005.

[31] SSRL, "Standford Auto Mounting Puck and Cassette," 2015. [Online]. Available: http://smb.slac.stanford.edu/users_guide/manual/Using_SSRL_Automated_Mounti.html. [Accessed: 15-Oct-2015].

[32] Katherine, McAuley, Mark, Williams, Stuart and Fisher, "BART – the new robotic sample changer for MX beamlines at Diamond," 2015. [Online]. Available: http://www.diamond.ac.uk/Home/Corporate-Literature/Annual-Review/Review2015/Villages/Macromolecular-Crystallography-Village/Macromolecular-Crystallography-Village-Developments/BART---the-new-robotic-sample-changer-for-MX-beamlines-at-Diamond.html.

[33] IRELEC, "CATS Cryogenic automated sample changer for macromolecular crystallography," 2015. [Online]. Available: http://www.irelec-alcen.com/en/products/cats-cryogenic-automated-sample-changer-macromolecular-crystallography. [Accessed: 09-Oct-2015].

[34] Rigaku, "Automated crystal transport orientation and retrieval robot," 2015. [Online]. Available: http://www.rigaku.com/en/products/protein/actor. [Accessed: 09-Oct-2015].

[35] G. Ueno, R. Hirose, K. Ida, T. Kumasaka, and M. Yamamoto, "Sample management system for a vast amount of frozen crystals at SPring-8," *J. Appl. Crystallogr.*, vol. 37, no. 6, pp. 867–873, 2004.

[36] N. Okazaki, K. Hasegawa, G. Ueno, H. Murakami, T. Kumasaka, and M. Yamamoto, "Mail-in data collection at SPring-8 protein crystallography beamlines.," *J. Synchrotron Radiat.*, vol. 15, no. Pt 3, pp. 288–91, 2008.

[37] E. Pohl, U. Ristau, T. Gehrmann, D. Jahn, B. Robrahn, D. Malthan, H. Dobler, and C. Hermes, "Automation of the EMBL Hamburg protein crystallography beamline BW7B," *J. Synchrotron Radiat.*, vol. 11, no. 5, pp. 372–377, 2004.

[38] K. Mader, F. Marone, C. Hintermüller, G. Mikuljan, A. Isenegger, and M. Stampanoni, "High-throughput full-automatic synchrotron-based tomographic microscopy," *J. Synchrotron Radiat.*, vol. 18, pp. 117–124, 2011.

[39] G. König, S. Bruckner, and S. Boresch, "Absolute hydration free energies of blocked amino acids: Implications for protein solvation and stability," *Biophys. J.*, vol. 104, no. 2, pp. 453–462, 2013.

[40] J. C. Biro, "Amino acid size, charge, hydropathy indices and matrices for protein structure analysis," *Theor. Biol. Med. Model.*, vol. 3, no. 1, pp. 1–12, 2006.

[41] J. M. Holton, "A beginner's guide to radiation damage," *J. Synchrotron Radiat.*, vol. 16, no. 2, pp. 133–142, 2009.

[42] I. D. Kuntz and W. Kauzmann, "Hydration of Proteins and Polypeptides," *Adv. Protein Chem.*, vol. 28, no. C, pp. 239–345, 1974.

[43] J. Sanchez-Weatherby and I. Moraes, "Crystal dehydration inmembrane protein crystallography," *Adv. Exp. Med. Biol.*, vol. 922, pp. 73–89, 2016.

[44] J. Sanchez-Weatherby, M. W. Bowler, J. Huet, A. Gobbo, F. Felisaz, B. Lavault, R. Moya, J. Kadlec, R. B. G. Ravelli, and F. Cipriani, "Improving diffraction by humidity control: A novel device compatible with X-ray beamlines," *Acta Crystallogr. Sect. D Biol. Crystallogr.*, vol. 65, no. 12, pp. 1237–1246, 2009.

[45] D. Axford, R. L. Owen, J. Aishima, J. Foadi, A. W. Morgan, J. I. Robinson, J. E. Nettleship, R. J. Owens, I. Moraes, E. E. Fry, J. M. Grimes, K. Harlos, A. Kotecha, J. Ren, G. Sutton, T. S. Walter, D. I. Stuart, and G. Evans, "In situ macromolecular crystallography using microbeams," *Acta Crystallogr. Sect. D Biol. Crystallogr.*, vol. 68, no. 5, pp. 592–600, 2012.

[46] H. Taberman, "Radiation Damage in Macromolecular Crystallography — An Experimentalist ' s View," pp. 5–9, 2018.

[47] E. F. Garman, "Developments in x-ray crystallographic structure determination of biological macromolecules," *Sci. (New York, N Y)*, vol. 343, no. 6175, pp. 1102–1108, 2014.

[48] D. S. Khvostichenko, E. Kondrashkina, S. L. Perry, A. S. Pawate, K. Brister, and P. J. A.

Kenis, “An X-ray transparent microfluidic platform for screening of the phase behavior of lipidic mesophases,” *Analyst*, vol. 138, no. 18, p. 5384, 2013.

[49] D. S. Khvostichenko, J. M. Schieferstein, A. S. Pawate, P. D. Laible, and P. J. A. Kenis, “X-ray transparent microfluidic chip for mesophase-based crystallization of membrane proteins and on-chip structure determination,” *Cryst. Growth Des.*, 2014.

[50] C. J. Gerdts, M. Elliott, S. Lovell, M. B. Mixon, A. J. Napuli, B. L. Staker, P. Nollert, and L. Stewart, “The plug-based nanovolume Microcapillary Protein Crystallization System (MPCS),” *Acta Crystallogr. Sect. D Biol. Crystallogr.*, 2008.

[51] S. Sui, Y. Wang, K. W. Kolewe, V. Srajer, R. Henning, J. D. Schiffman, C. Dimitrakopoulos, and S. L. Perry, “Graphene-based microfluidics for serial crystallography,” *Lab Chip*, vol. 16, no. 16, pp. 3082–3096, 2016.

[52] G. Kisselman, W. Qiu, V. Romanov, C. M. Thompson, R. Lam, K. P. Battaile, E. F. Pai, and N. Y. Chirgadze, “X-CHIP: An integrated platform for high-throughput protein crystallization and on-the-chip X-ray diffraction data collection,” *Acta Crystallogr. Sect. D Biol. Crystallogr.*, 2011.

[53] D. Axford, P. Aller, J. Sanchez-Weatherby, and J. Sandy, “Applications of thin-film sandwich crystallization platforms,” *Acta Crystallogr. Sect. Struct. Biol. Commun.*, vol. 72, no. March, pp. 313–319, 2016.

[54] T. Y. Teng, “Mounting of crystals for macromolecular crystallography in a free-standing thin film,” *Journal of Applied Crystallography*, vol. 23, no. 5. pp. 387–391, 1990.

[55] G. K. Feld, M. Heymann, W. H. Benner, T. Pardini, C. J. Tsai, S. Boutet, M. A. Coleman, M. S. Hunter, X. Li, M. Messerschmidt, A. Opathalage, B. Pedrini, G. J. Williams, B. A. Krantz, S. Fraden, S. Hau-Riege, J. E. Evans, B. W. Segelke, and M. Frank, “Low-Z polymer sample supports for fixed-target serial femtosecond X-ray crystallography,” *J. Appl. Crystallogr.*, vol. 48, pp. 1072–1079, 2015.

[56] a. Georgiev, P. K. Allen, and W. Edstrom, “Visually-guided protein crystal manipulation using micromachined silicon tools,” *2004 IEEE/RSJ Int. Conf. Intell. Robot. Syst. (IEEE Cat. No.04CH37566)*, 2004.

[57] C. X. Weichenberger, P. V. Afonine, K. Kantardjieff, and B. Rupp, “The solvent component of macromolecular crystals,” *Acta Crystallogr. Sect. D Biol. Crystallogr.*, 2015.

[58] J. Holton, “A beginner’s guide to radiation damage,” *J. Synchrotron Radiat.*, vol. 16, no. Pt 2, pp. 133–142, 2009.

[59] R. J. Southworth-Davies, M. A. Medina, I. Carmichael, and E. F. Garman, “Observation of Decreased Radiation Damage at Higher Dose Rates in Room Temperature Protein Crystallography,” *Structure*, vol. 15, no. 12, pp. 1531–1541, 2007.

[60] P. Nogly, V. Panneels, G. Nelson, C. Gati, T. Kimura, C. Milne, D. Milathianaki, M. Kubo, W. Wu, C. Conrad, J. Coe, R. Bean, Y. Zhao, P. Båth, R. Dods, R. Harimoorthy, K. R. Beyerlein, J. Rheinberger, D. James, D. DePonte, C. Li, L. Sala, G. J. Williams, M. S. Hunter, J. E. Koglin, P. Berntsen, E. Nango, S. Iwata, H. N. Chapman, P. Fromme, M.

Frank, R. Abela, S. Boutet, A. Barty, T. A. White, U. Weierstall, J. Spence, R. Neutze, G. Schertler, and J. Standfuss, "Lipidic cubic phase injector is a viable crystal delivery system for time-resolved serial crystallography," *Nat. Commun.*, vol. 7, no. 12314, pp. 1–9, 2016.

[61] R. L. Owen, D. Axford, D. A. Sherrell, A. Kuo, O. P. Ernst, E. C. Schulz, R. J. D. Miller, and H. M. Mueller-Werkmeister, "Low-dose fixed-target serial synchrotron crystallography," *Acta Crystallogr. Sect. D Struct. Biol.*, vol. 73, no. 4, pp. 373–378, 2017.

[62] P. Roedig, I. Vartiainen, R. Duman, S. Panneerselvam, N. Stübe, O. Lorbeer, M. Warmer, G. Sutton, D. I. Stuart, E. Weckert, C. David, A. Wagner, and A. Meents, "A micro-patterned silicon chip as sample holder for macromolecular crystallography experiments with minimal background scattering," *Sci. Rep.*, 2015.

[63] D. A. Sherrell, A. J. Foster, L. Hudson, B. Nutter, J. O'Hea, S. Nelson, O. Par??-Labrosse, S. Oghbaey, R. J. D. Miller, and R. L. Owen, "A modular and compact portable mini-endstation for high-precision, high-speed fixed target serial crystallography at FEL and synchrotron sources," *J. Synchrotron Radiat.*, vol. 22, pp. 1372–1378, 2015.

[64] A. Y. Lyubimov, T. D. Murray, A. Koehl, I. E. Araci, M. Uervirojnangkoorn, O. B. Zeldin, A. E. Cohen, S. M. Soltis, E. L. Baxter, A. S. Brewster, N. K. Sauter, A. T. Brunger, and J. M. Berger, "Capture and X-ray diffraction studies of protein microcrystals in a microfluidic trap array.," *Acta Crystallogr. D. Biol. Crystallogr.*, vol. 71, no. Pt 4, pp. 928–40, 2015.

[65] D. C. Carter, B. Wright, T. Miller, J. Chapman, P. Twigg, K. Keeling, K. Moody, M. White, J. Click, J. R. Ruble, J. X. Ho, L. Adcock-Downey, T. Dowling, C. H. Chang, P. Ala, J. Rose, B. C. Wang, J. P. Declercq, C. Evrard, J. Rosenberg, J. P. Wery, D. Clawson, M. Wardell, W. Stallings, and A. Stevens, "PCAM: A multi-user facility-based protein crystallization apparatus for microgravity," *J. Cryst. Growth*, 1999.

[66] A. Le Maire, M. Gelin, S. Pochet, F. Hoh, M. Pirocchi, J. F. Guichou, J. L. Ferrer, and G. Labesse, "In-plate protein crystallization, in situ ligand soaking and X-ray diffraction," *Acta Crystallogr. Sect. D Biol. Crystallogr.*, vol. 67, no. 9, pp. 747–755, 2011.

[67] T. D. Nguyen, V. T. Tran, Y. Q. Fu, and H. Du, "Patterning and manipulating microparticles into a three-dimensional matrix using standing surface acoustic waves," *Appl. Phys. Lett.*, vol. 112, no. 21, pp. 1–6, 2018.

[68] C. H. Chen, S. H. Cho, F. Tsai, A. Erten, and Y. H. Lo, "Microfluidic cell sorter with integrated piezoelectric actuator," *Biomed. Microdevices*, vol. 11, no. 6, pp. 1223–1231, 2009.

[69] B. Barfield, "A STUDY OF LIQUID BEHAVIOR IN A KUNDT'S TUBE," Georgia Institute of Technology, 1965.

[70] D. Yin, G. Xu, M. Wang, M. Shen, T. Xu, X. Zhu, and X. Shi, "Effective cell trapping using PDMS microspheres in an acoustofluidic chip," *Colloids Surfaces B Biointerfaces*, vol. 157, pp. 347–354, 2017.

[71] P. Li, Z. Mao, Z. Peng, L. Zhou, Y. Chen, P.-H. Huang, C. I. Truica, J. J. Drabick, W. S.

El-Deiry, M. Dao, S. Suresh, and T. J. Huang, "Acoustic separation of circulating tumor cells.," *Proc. Natl. Acad. Sci. U. S. A.*, vol. 112, no. 16, 2015.

[72] J. Woods, P. T. Docker, C. E. Dyer, S. J. Haswell, and J. Greenman, "On-chip integrated labelling, transport and detection of tumour cells.," *Electrophoresis*, vol. 32, no. 22, pp. 3188–95, Nov. 2011.

[73] L. Schmid, D. a. Weitz, and T. Franke, "Sorting drops and cells with acoustics: acoustic microfluidic fluorescence-activated cell sorter," *Lab Chip*, vol. 14, no. 19, 2014.

[74] P. Augustsson, J. T. Karlsen, H. W. Su, H. Bruus, and J. Voldman, "Iso-acoustic focusing of cells for size-insensitive acousto-mechanical phenotyping," *Nat. Commun.*, 2016.

[75] M. F. C. Ladd and R. A. Palmer, *Structure Determination by X-Ray Crystallography*. 1995.

[76] X. Ding, S.-C. S. Lin, B. Kiraly, H. Yue, S. Li, I.-K. Chiang, J. Shi, S. J. Benkovic, and T. J. Huang, "On-chip manipulation of single microparticles, cells, and organisms using surface acoustic waves," *Proceedings of the National Academy of Sciences*, vol. 109. pp. 11105–11109, 2012.

[77] B. Hammarström, M. Evander, H. Barbeau, M. Bruzelius, J. Larsson, T. Laurell, and J. Nilsson, "Non-contact acoustic cell trapping in disposable glass capillaries.," *Lab Chip*, vol. 10, no. 17, pp. 2251–2257, 2010.

[78] H. Mulvana, S. Cochran, and M. Hill, "Ultrasound assisted particle and cell manipulation on-chip," *Advanced Drug Delivery Reviews*, vol. 65, no. 11–12. pp. 1600–1610, 2013.

[79] M. Wu, Y. Ouyang, Z. Wang, R. Zhang, P.-H. Huang, C. Chen, H. Li, P. Li, D. Quinn, M. Dao, S. Suresh, Y. Sadovsky, and T. J. Huang, "Isolation of exosomes from whole blood by integrating acoustics and microfluidics," *Proc. Natl. Acad. Sci.*, 2017.

[80] M. Evander and J. Nilsson, "Acoustofluidics 20: Applications in acoustic trapping," *Lab on a Chip*, vol. 12, no. 22. p. 4667, 2012.

[81] F. Guo, W. Zhou, P. Li, Z. Mao, N. H. Yennawar, J. B. French, and T. J. Huang, "Precise Manipulation and Patterning of Protein Crystals for Macromolecular Crystallography Using Surface Acoustic Waves.," *Small*, vol. 11, no. 23, pp. 2733–7, 2015.

[82] A. Neild, S. Oberti, F. Beyeler, J. Dual, and B. J. Nelson, "A micro-particle positioning technique combining an ultrasonic manipulator and a microgripper," *Journal of Micromechanics and Microengineering*, vol. 16. pp. 1562–1570, 2006.

[83] E. Teplitsky, K. Joshi, D. L. Ericson, A. Scalia, J. D. Mullen, R. M. Sweet, and A. S. Soares, "High throughput screening using acoustic droplet ejection to combine protein crystals and chemical libraries on crystallization plates at high density," *J. Struct. Biol.*, 2015.

[84] A. W. Martinez, S. T. Phillips, and G. M. Whitesides, "Three-dimensional microfluidic devices fabricated in layered paper and tape.," *Proc. Natl. Acad. Sci. U. S. A.*, vol. 105, no. 50, pp. 19606–19611, 2008.

[85] C. G. Roessler, A. Kuczewski, R. Stearns, R. Ellson, J. Olechno, A. M. Orville, M. Allaire,

A. S. Soares, and A. Héroux, "Acoustic methods for high-throughput protein crystal mounting at next-generation macromolecular crystallographic beamlines," *J. Synchrotron Radiat.*, vol. 20, no. 5, pp. 805–808, 2013.

[86] F. D. Fuller, S. Gul, R. Chatterjee, E. S. Burgie, I. D. Young, H. Lebrette, V. Srinivas, A. S. Brewster, T. Michels-Clark, J. A. Clinger, B. Andi, M. Ibrahim, E. Pastor, C. de Lichtenberg, R. Hussein, C. J. Pollock, M. Zhang, C. A. Stan, T. Kroll, T. Fransson, C. Weninger, M. Kubin, P. Aller, L. Lassalle, P. Bräuer, M. D. Miller, M. Amin, S. Koroidov, C. G. Roessler, M. Allaire, R. G. Sierra, P. T. Docker, J. M. Glownia, S. Nelson, J. E. Koglin, D. Zhu, M. Chollet, S. Song, H. Lemke, M. Liang, D. Sokaras, R. Alonso-Mori, A. Zouni, J. Messinger, U. Bergmann, A. K. Boal, J. M. Bollinger, C. Krebs, M. Högbom, G. N. Phillips, R. D. Vierstra, N. K. Sauter, A. M. Orville, J. Kern, V. K. Yachandra, and J. Yano, "Drop-on-demand sample delivery for studying biocatalysts in action at X-ray free-electron lasers," *Nat. Methods*, vol. 14, no. 4, pp. 443–449, 2017.

[87] D. Huang and E. S. Kim, "Micromachined acoustic-wave liquid ejector," *J. Microelectromechanical Syst.*, vol. 10, no. 3, pp. 442–449, 2001.

[88] C. M. Cuttitta, D. L. Ericson, A. Scalia, C. G. Roessler, E. Teplitsky, K. Joshi, O. Campos, R. Agarwal, M. Allaire, A. M. Orville, R. M. Sweet, and A. S. Soares, "Acoustic transfer of protein crystals from agarose pedestals to micromeshes for high-throughput screening," *Acta Crystallogr. Sect. D Biol. Crystallogr.*, 2015.

[89] L. E. Kinsler, A. R. Frey, A. B. Coppens, and J. V Sanders, "Fundamentals of acoustics," *Fundamentals of Acoustics, 4th Edition, by Lawrence E. Kinsler, Austin R. Frey, Alan B. Coppens, James V. Sanders, pp. 560. ISBN 0-471-84789-5. Wiley-VCH, December 1999.*, vol. 1. p. 560, 1999.

[90] B. A. Auld, *Acoustic fields and waves in solids, volumes I and II*. 1975.

[91] D. Morgan and E. G. S. Paige, *Surface Acoustic Wave Filters*. 2007.

[92] K. Yoneda, M. Tawata, and S. Hattori, "Laser Probe for Surface Acoustic Wave Measurements," *Jpn. J. Appl. Phys.*, vol. 20, pp. 61–64, 1981.

[93] S. T. Thornton and A. Rex, *Modern Physics for Scientists and Engineers*, 4th ed. Boston, MA: Physics and Astronomy: Charles Hartford, 2013.

[94] S. Zhang, R. Xia, and T. R. Shrout, "Lead-free piezoelectric ceramics vs. PZT?," *J. Electroceramics*, 2007.

[95] H. Jaffe and D. A. Berlincourt, "Piezoelectric Transducer Materials," *Proc. IEEE*, 1965.

[96] Y. V. Gulyaev and F. S. Hickernell, "Acoustoelectronics: history, present state, and new ideas for a new era," *IEEE Ultrason. Symp. 2004*, 2004.

[97] T. D. Rossing, *Handbook of Acoustics*. 2009.

[98] M. P. da Cunha and E. L. Adler, "High Velocity Pseudosurface Waves (HVPSAW)," *IEEE Trans. Ultrason. Ferroelectr. Freq. Control*, 1995.

[99] C. S. Lam, C. S. Lam, Y. J. C. Wang, Y. J. C. Wang, S. M. Wang, and S. M. Wang, "A

Review of the Recent Development of Temperature Stable Cuts of Quartz for SAW Applications," *Ultrasonics*, 2004.

[100] R. H. Olsson III, K. Hattar, S. Homeijer, M. Wiwi, M. Eichenfield, D. Branch, M. S. Baker, J. Nguyen, B. Clark, T. Bauer, and T. A. Friedmann, "A High Electromechanical Coupling Coefficient SH0 Lamb Wave Lithium Niobate Micromechanical Resonator and a Method for Fabrication," *Sensors Actuators A Phys.*, vol. 209, pp. 183–190, 2014.

[101] D. Morgan and E. G. S. Paige, *Surface Acoustic Wave Filters*. 2007.

[102] X. Ding, P. Li, S.-C. S. Lin, Z. S. Stratton, N. Nama, F. Guo, D. Slotcavage, X. Mao, J. Shi, F. Costanzo, and T. J. Huang, "Surface acoustic wave microfluidics.," *Lab Chip*, vol. 13, no. 18, pp. 3626–49, 2013.

[103] a Lenshof, M. Evander, T. Laurell, and J. Nilsson, "Acoustofluidics 5: Building microfluidic acoustic resonators.," *Lab Chip*, vol. 12, no. 4, pp. 684–95, 2012.

[104] L. Y. Yeo and J. R. Friend, "Surface Acoustic Wave Microfluidics," *Annu. Rev. Fluid Mech.*, vol. 46, no. 1, pp. 379–406, 2014.

[105] E. MEYER and E.-G. NEUMANN, *Physical and Applied Acoustics*. 1972.

[106] J. R. Vig and A. Ballato, *Ultrasonic Instruments and Devices II - Reference for Modern Instrumentation, Techniques, and Technology*. 1999.

[107] Boston-Piezo-Optics, "Material Properties," 2018. [Online]. Available: https://www.bostonpiezooptics.com/material-properties. [Accessed: 24-Aug-2018].

[108] L. Brekhovskikh and V. Goncharov, *Mechanics of Continua and Wave Dynamics*. Springer-Verlag, 1985.

[109] J. Lighthill, *Waves in Fluids*. Cambridge University Press, 1978.

[110] W. G. Hankel, "Ueber die actino- und piezoelectrischen Eigenschaften des Bergkrystalles und ihre Beziehung zu den thermoelectrischen," *Ann. Phys.*, vol. 253, no. 9, pp. 163–175.

[111] E. a. Avellone, T. Baumeister, and H. Saunders, *Marks Standard Handbook for Mechanical Engineers*. 1993.

[112] Morgan Technical Ceramics, "Physical Basis," in *Piezoelectric Ceramics Properties and Applications*, 2013, pp. 1–12.

[113] K. Nakamura, *Ultrasonic transducers: Materials and design for sensors, actuators and medical applications*. 2012.

[114] R. S. Dahiya and M. Valle, *Robotic Tactile Sensing*. 2013.

[115] H. Fischer, I. Polikarpov, and A. F. Craievich, "Average protein density is a molecular-weight-dependent function," *Protein Sci.*, vol. 13, no. 10, pp. 2825–2828, 2009.

[116] H. Research, "Hampton Research Index Screen User Guide," 2016. [Online]. Available: https://hamptonresearch.com/product_detail.aspx?cid=1&sid=24&pid=5. [Accessed:

09-Apr-2018].

[117] M. Rhodes, *Introduction to Particle Technology: Second Edition*. 2008.

[118] Pilatus, "Pilatus 3 X 6M Technical Data," 2018. [Online]. Available: https://www.dectris.com/products/pilatus3/pilatus3-x-for-synchrotron/details/pilatus3-x-6m. [Accessed: 27-Mar-2018].

[119] M. Greenspan and C. E. Tschiegg, "Speed of sound in water by a direct method," *J. Res. Natl. Bur. Stand. (1934).*, vol. 59, no. 4, p. 249, 1957.

[120] M. Levy, *Modern Acoustical Techniques for the Measurement of Mechanical Properties*, 1st ed. San Diego: Academic Press, 2001.

[121] T. Hickernell, F. Fliegel, and F. Hickernell, "The elastic properties of thin-film silicon nitride," *Ultrason. Symp. 1990. Proceedings., IEEE 1990*, 1990.

[122] W. A. Fate, "High-temperature elastic moduli of polycrystalline silicon nitride," *J. Appl. Phys.*, vol. 46, no. 6, pp. 2375–2377, 1975.

[123] C. Torres-Torres, A. López-Suárez, R. Torres-Martínez, a Rodriguez, J. A. Reyes-Esqueda, L. Castañeda, J. C. Alonso, and A. Oliver, "Modulation of the propagation speed of mechanical waves in silicon quantum dots embedded in a silicon-nitride film," *Opt. Express*, vol. 20, no. 4, p. 4784, 2012.

[124] H. N. Chapman, P. Fromme, A. Barty, T. A. White, R. A. Kirian, A. Aquila, M. S. Hunter, J. Schulz, D. P. DePonte, U. Weierstall, R. B. Doak, F. R. N. C. Maia, A. V. Martin, I. Schlichting, L. Lomb, N. Coppola, R. L. Shoeman, S. W. Epp, R. Hartmann, D. Rolles, A. Rudenko, L. Foucar, N. Kimmel, G. Weidenspointner, P. Holl, M. Liang, M. Barthelmess, C. Caleman, S. Boutet, M. J. Bogan, J. Krzywinski, C. Bostedt, S. Bajt, L. Gumprecht, B. Rudek, B. Erk, C. Schmidt, A. Hömke, C. Reich, D. Pietschner, L. Strüder, G. Hauser, H. Gorke, J. Ullrich, S. Herrmann, G. Schaller, F. Schopper, H. Soltau, K.-U. Kühnel, M. Messerschmidt, J. D. Bozek, S. P. Hau-Riege, M. Frank, C. Y. Hampton, R. G. Sierra, D. Starodub, G. J. Williams, J. Hajdu, N. Timneanu, M. M. Seibert, J. Andreasson, A. Rocker, O. Jönsson, M. Svenda, S. Stern, K. Nass, R. Andritschke, C.-D. Schröter, F. Krasniqi, M. Bott, K. E. Schmidt, X. Wang, I. Grotjohann, J. M. Holton, T. R. M. Barends, R. Neutze, S. Marchesini, R. Fromme, S. Schorb, D. Rupp, M. Adolph, T. Gorkhover, I. Andersson, H. Hirsemann, G. Potdevin, H. Graafsma, B. Nilsson, and J. C. H. Spence, "Femtosecond X-ray protein nanocrystallography," *Nature*, vol. 470, no. 7332, pp. 73–77, 2011.

[125] C. Nave, "Matching X-ray beam and detector properties to protein crystals of different perfection," *J. Synchrotron Radiat.*, vol. 21, no. 3, pp. 537–546, 2014.

[126] J. S. Fraser, H. van den Bedem, A. J. Samelson, P. T. Lang, J. M. Holton, N. Echols, and T. Alber, "Accessing protein conformational ensembles using room-temperature X-ray crystallography," *Proc. Natl. Acad. Sci.*, vol. 108, no. 39, pp. 16247–16252, 2011.

[127] C. Mueller, A. Marx, S. W. Epp, Y. Zhong, A. Kuo, A. R. Balo, J. Soman, F. Schotte, H. T. Lemke, R. L. Owen, E. F. Pai, A. R. Pearson, J. S. Olson, P. A. Anfinrud, O. P. Ernst, and R. J. Dwayne Miller, "Fixed target matrix for femtosecond time-resolved and in situ

serial micro-crystallography.," *Struct. Dyn. (Melville, N.Y.)*, vol. 2, no. 5, p. 054302, 2015.

[128] D. Axford, P. Aller, J. Sanchez-Weatherby, and J. Sandy, "Applications of thin-film sandwich crystallization platforms," *Acta Crystallogr. Sect. Struct. Biol. Commun.*, vol. 72, pp. 313–319, 2016.

[129] D. Axford, R. L. Owen, J. Aishima, J. Foadi, A. W. Morgan, J. I. Robinson, J. E. Nettleship, R. J. Owens, I. Moraes, E. E. Fry, J. M. Grimes, K. Harlos, A. Kotecha, J. Ren, G. Sutton, T. S. Walter, D. I. Stuart, and G. Evans, "In situ macromolecular crystallography using microbeams," *Acta Crystallogr. Sect. D Biol. Crystallogr.*, vol. 68, no. 5, pp. 592–600, 2012.

[130] A. L. Bernassau, P. Glynne-Jones, F. Gesellchen, M. Riehle, M. Hill, and D. R. S. Cumming, "Controlling acoustic streaming in an ultrasonic heptagonal tweezers with application to cell manipulation," *Ultrasonics*, vol. 54, pp. 268–274, 2014.

[131] F. Petersson, A. Nilsson, C. Holm, H. Jonsson, and T. Laurell, "Continuous separation of lipid particles from erythrocytes by means of laminar flow and acoustic standing wave forces.," *Lab Chip*, vol. 5, pp. 20–22, 2005.

[132] J. Nam, H. Lim, C. Kim, J. Yoon Kang, and S. Shin, "Density-dependent separation of encapsulated cells in a microfluidic channel by using a standing surface acoustic wave," *Biomicrofluidics*, vol. 6, no. 2, 2012.

[133] a Lenshof, M. Evander, T. Laurell, and J. Nilsson, "Acoustofluidics 5: Building microfluidic acoustic resonators.," *Lab Chip*, vol. 12, no. 4, pp. 684–95, Feb. 2012.

[134] H. Bruus, J. Dual, J. Hawkes, M. Hill, T. Laurell, J. Nilsson, S. Radel, S. Sadhal, and M. Wiklund, "Forthcoming Lab on a Chip tutorial series on acoustofluidics: acoustofluidics-exploiting ultrasonic standing wave forces and acoustic streaming in microfluidic systems for cell and particle manipulation.," *Lab Chip*, vol. 11, no. 21, pp. 3579–80, Nov. 2011.

[135] D. J. Collins, B. Morahan, J. Garcia-Bustos, C. Doerig, M. Plebanski, and A. Neild, "Two-dimensional single-cell patterning with one cell per well driven by surface acoustic waves.," *Nat. Commun.*, vol. 6, p. 8686, 2015.

[136] S. Tsujino and T. Tomizaki, "Ultrasonic acoustic levitation for fast frame rate X-ray protein crystallography at room temperature," *Nat. Publ. Gr.*, no. April, pp. 1–9, 2016.

[137] J. Guo, Y. Kang, and Y. Ai, "Radiation dominated acoustophoresis driven by surface acoustic waves," *J. Colloid Interface Sci.*, vol. 455, pp. 203–211, 2015.

[138] O. Manneberg, J. Svennebring, H. M. Hertz, and M. Wiklund, "Wedge transducer design for two-dimensional ultrasonic manipulation in a microfluidic chip," *J. Micromechanics Microengineering*, vol. 18, no. 9, 2008.

[139] P. Augustsson, R. Barnkob, C. Grenvall, T. Deierborg, P. Brundin, H. Bruus, and T. Laurell, "Measuring the Acoustophoretic Contrast Factor of Living Cells in Microchannels," *Cell*, no. October, pp. 1337–1339, 2010.

[140] I. Leibacher, P. Reichert, and J. Dual, "Microfluidic droplet handling by bulk acoustic

wave (BAW) acoustophoresis," *Lab Chip*, vol. 15, pp. 2896–2905, 2015.

[141] X. Ding, S.-C. S. Lin, B. Kiraly, H. Yue, S. Li, I.-K. Chiang, J. Shi, S. J. Benkovic, and T. J. Huang, "On-chip manipulation of single microparticles, cells, and organisms using surface acoustic waves," *Proc. Natl. Acad. Sci.*, vol. 109, no. 28, pp. 11105–11109, 2012.

[142] A. P. Source, "Structural Biology Center."

[143] K. Yosioka and Y. Kawasima, "Acoustic radiation pressure on a compressible sphere," *Acustica*, vol. 5, pp. 167–173, 1955.

[144] P. L. Marston and D. B. Thiessen, "Manipulation of fluid objects with acoustic radiation pressure," in *Annals of the New York Academy of Sciences*, 2004, vol. 1027, pp. 414–434.

[145] H. Bruus, "Acoustofluidics 7: The acoustic radiation force on small particles," *Lab on a Chip*, vol. 12. p. 1014, 2012.

[146] J. T. Karlsen and H. Bruus, "Size-dependent acoustophoretic contrast factor of microparticles and droplets," vol. 775, no. 1962, p. 16327, 2015.

[147] L. A. Goldsmith and H. P. Baden, "The mechanical properties of hair. I. The dynamic sonic modulus.," *J. Invest. Dermatol.*, vol. 55, no. 4, pp. 256–259, 1970.

[148] J. E. Carlson, J. Van Deventer, A. Scolan, and C. Carlander, "Frequency and temperature dependence of acoustic properties of polymers used in pulse-echo systems," *IEEE Symp. Ultrason. 2003*, vol. 1, no. 2, pp. 885–888, 2003.

[149] G. Evans, D. Axford, D. Waterman, and R. L. Owen, "Macromolecular microcrystallography," *Crystallogr. Rev.*, vol. 17, no. September, pp. 105–142, 2011.

[150] The Diamond Light Source, "IsPyB - About," 2018. [Online]. Available: https://www.diamond.ac.uk/Instruments/Mx/Common/Common-Manual/Using-ISPyB.html. [Accessed: 25-Jul-2018].

[151] Z. Zhang, N. K. Sauter, H. Van Den Bedem, G. Snell, and A. M. Deacon, "Automated diffraction image analysis and spot searching for high-throughput crystal screening," *J. Appl. Crystallogr.*, vol. 39, no. 1, pp. 112–119, 2006.

[152] M. Gedge and M. Hill, "Acoustofluidics 17: theory and applications of surface acoustic wave devices for particle manipulation.," *Lab Chip*, vol. 12, no. 17, pp. 2998–3007, Sep. 2012.

[153] X. Noblin, A. Buguin, and F. Brochard-Wyart, "Vibrated sessile drops: Transition between pinned and mobile contact line oscillations," *Eur. Phys. J. E*, vol. 14, no. 4, pp. 395–404, 2004.

[154] B. Vukasinovic, M. K. Smith, and A. Glezer, "Dynamics of a sessile drop in forced vibration," *J. Fluid Mech.*, 2007.

[155] J. S. Sharp, D. J. Farmer, and J. Kelly, "Contact angle dependence of the resonant frequency of sessile water droplets.," *Langmuir*, 2011.

[156] K. Yu, X. Wei, Z. Jiang, Y. Lei, and F. Zhang, "Surface acoustic wave (SAW)-induced particle rotation and aggregation in microdroplet," in *IEEE International Conference on Nano/Molecular Medicine and Engineering, NANOMED*, 2017.

[157] T. Sano, T. Onuki, Y. Hamate, M. Hojo, S. Nagasawa, and H. Kuwano, "Micro blender and separator using inner-vortex of droplet induced by surface acoustic wave," in *TRANSDUCERS 2009 - 15th International Conference on Solid-State Sensors, Actuators and Microsystems*, 2009.

[158] C. G. Burton, D. Axford, A. M. J. Edwards, R. J. Gildea, R. H. Morris, M. I. Newton, A. M. Orville, M. Prince, P. D. Topham, and P. T. Docker, "An acoustic on-chip goniometer for room temperature macromolecular crystallography," *Lab Chip*, vol. 17, no. 24, pp. 4225–4230, 2017.

[159] A. Otten, S. Köster, B. Struth, A. Snigirev, and T. Pfohl, "Microfluidics of soft matter investigated by small-angle X-ray scattering," *J. Synchrotron Radiat.*, vol. 12, no. 6, pp. 745–750, 2005.

[160] A. Marmur, "Wetting on hydrophobic rough surfaces: To be heterogeneous or not to be?," *Langmuir*, vol. 19, no. 20, pp. 8343–8348, 2003.

[161] K. Dhouib, C. Khan Malek, W. Pfleging, B. Gauthier-Manuel, R. Duffait, G. Thuillier, R. Ferrigno, L. Jacquamet, J. Ohana, J.-L. Ferrer, A. Théobald-Dietrich, R. Giegé, B. Lorber, and C. Sauter, "Microfluidic chips for the crystallization of biomacromolecules by counter-diffusion and on-chip crystal X-ray analysis.," *Lab Chip*, vol. 9, no. 10, pp. 1412–1421, 2009.

[162] D. P. DePonte, U. Weierstall, K. Schmidt, J. Warner, D. Starodub, J. C. H. Spence, and R. B. Doak, "Gas dynamic virtual nozzle for generation of microscopic droplet streams," *J. Phys. D. Appl. Phys.*, vol. 41, no. 19, p. 195505, 2008.

[163] R. G. Sierra, H. Laksmono, J. Kern, R. Tran, J. Hattne, R. Alonso-Mori, B. Lassalle-Kaiser, C. Gl??ckner, J. Hellmich, D. W. Schafer, N. Echols, R. J. Gildea, R. W. Grosse-Kunstleve, J. Sellberg, T. A. McQueen, A. R. Fry, M. M. Messerschmidt, A. Miahnahri, M. M. Seibert, C. Y. Hampton, D. Starodub, N. D. Loh, D. Sokaras, T. C. Weng, P. H. Zwart, P. Glatzel, D. Milathianaki, W. E. White, P. D. Adams, G. J. Williams, S. Boutet, A. Zouni, J. Messinger, N. K. Sauter, U. Bergmann, J. Yano, V. K. Yachandra, and M. J. Bogan, "Nanoflow electrospinning serial femtosecond crystallography," *Acta Crystallogr. Sect. D Biol. Crystallogr.*, vol. 68, no. 11, pp. 1584–1587, 2012.

[164] C. G. Roessler, R. Agarwal, M. Allaire, R. Alonso-Mori, B. Andi, J. F. R. Bachega, M. Bommer, A. S. Brewster, M. C. Browne, R. Chatterjee, E. Cho, A. E. Cohen, M. Cowan, S. Datwani, V. L. Davidson, J. Defever, B. Eaton, R. Ellson, Y. Feng, L. P. Ghislain, J. M. Glownia, G. Han, J. Hattne, J. Hellmich, A. H??roux, M. Ibrahim, J. Kern, A. Kuczewski, H. T. Lemke, P. Liu, L. Majlof, W. M. McClintock, S. Myers, S. Nelsen, J. Olechno, A. M. Orville, N. K. Sauter, A. S. Soares, S. M. Soltis, H. Song, R. G. Stearns, R. Tran, Y. Tsai, M. Uervirojnangkoorn, C. M. Wilmot, V. Yachandra, J. Yano, E. T. Yukl, D. Zhu, and A. Zouni, "Acoustic Injectors for Drop-On-Demand Serial Femtosecond Crystallography," *Structure*, vol. 24, no. 4, pp. 631–640, 2016.

[165] A. Ishchenko, V. Cherezov, and W. Liu, "Preparation and Delivery of Protein Microcrystals in Lipidic Cubic Phase for Serial Femtosecond Crystallography," *J. Vis. Exp.*, no. 115, pp. 1–8, 2016.

[166] C. Burton, P. Docker, M. Prince, D. Axford, A. Orville, and P. Topham, "Contact angle and active drop transport for time resolved Macromolecular and serial femto-second crystallography," in *Informatics, Electronics and Microsystems - TechConnect Briefs 2017*, 2017, vol. 4, pp. 116–119.

[167] S. Tsujino and T. Tomizaki, "Ultrasonic acoustic levitation for fast frame rate X-ray protein crystallography at room temperature," *Nat. Publ. Gr.*, no. April, pp. 1–9, 2016.

[168] S. L. Perry, S. Guha, A. S. Pawate, A. Bhaskarla, V. Agarwal, S. K. Nair, and P. J. a Kenis, "A microfluidic approach for protein structure determination at room temperature via on-chip anomalous diffraction.," *Lab Chip*, vol. 13, no. 16, pp. 3183–7, 2013.

[169] M. Maeki, H. Yamaguchi, M. Tokeshi, and M. Miyazaki, "Microfluidic Approaches for Protein Crystal Structure Analysis," *Anal. Sci.*, vol. 32, no. January, pp. 3–9, 2016.

[170] O. B. Zeldin, M. Gerstel, and E. F. Garman, "RADDOSE-3D: Time- and space-resolved modelling of dose in macromolecular crystallography," *J. Appl. Crystallogr.*, vol. 46, no. 4, pp. 1225–1230, 2013.

[171] S. Verma and P. J. Shlichta, "Imaging techniques for mapping solution parameters, growth rate, and surface features during the growth of crystals from solution," *Progress in Crystal Growth and Characterization of Materials*. 2008.

[172] G. S. Settles and M. J. Hargather, "A review of recent developments in schlieren and shadowgraph techniques," *Measurement Science and Technology*. 2017.

End of Document